Mitigation of Small Space Debris

Master Thesis

Patricia Carceller Suarez

TU Delft

Title Page Image Reference:

"We Need a Plan to Stop Polluting Space before It's Too Late." Wired, www.wired.com/story/we-need-a-plan-to-stop-polluting-space-before-its-too-late/. Accessed 14 Feb. 2023.

Mitigation of Small Space Debris

by

Patricia Carceller Suarez

to obtain the degree of Master of Science
at Delft University of Technology.

Student number: 5382726
Thesis committee:
Ir. R. Noomen, TU Delft, supervisor
Erwin Mooij TU Delft, Committee Chair
Jian Guo TU Delft, External Examiner

TU Delft

Preface

This report is the thesis work for the Master of Science at the Faculty of Aerospace Engineering of Delft University of Technology. It describes the potential mitigation of small space debris with a passive spacecraft. I gained interest in space debris while working on the DebriSat project during my time at the University of Florida, which was the main reason why I came to TU Delft to continue my studies. Before coming to the Netherlands, in the midst of the Covid-19 pandemic, I started working from home for a consulting company, although it was going to be a short time position, I ended up continuing my work during the entire duration of my study. This led to some delays in the thesis work, but I am happy to finally be able to say I finished.

I am so grateful to have had Ron Noomen as my supervisor, he truly kept me motivated throughout this process during our weekly meetings, helping me figure out my doubts and guiding me to solve all issues that arose. All of this would not have been possible without his constant positive attitude toward the challenges encountered and his continuous support. Furthermore, I would like to thank my family for pushing me to never give up and supporting me. My dad for listening to my questions, my mom for calling me every day to check up on me and my sister for always encouraging me. I would like to thank my boyfriend for keeping me company during this time and being there for me. I would also like to thank my friends who helped me with coding issues and who let me bounce my ideas off of them when I got stuck. For studying with me at the faculty while trying to stay optimistic when we all had problems. I couldn't have done it without them. I can certainly say it was a bumpy ride but I am happy to have been able to explore a topic that means so much to me further.

Patricia Carceller Suarez
Delft, April 14^{th} 2023

Abbreviations

ADR	Active Debris Removal
ADS	Airbus Defense and Space
AEDC	Air Force Arnold Engineering Development Complex
CFRP	Carbon-fiber-reinforced polymers
CPU	Central Processing Unit
ECI	Earth-Centered Inertial
ESA	European Space Agency
ESOC	European Space Operations Centre
FCC	Federal Communications Commission
IADC	Inter - Agency Space Debris Coordination Committee
ISS	International Space Station
JAXA	Japanese Aerospace Exploration Agency
LEO	Low Earth Orbit
LVLH	Local Vertial Local Horizontal
NASA	National Aeronautics and Space Administration
ODPO	NASA Orbital Debris Program Office
SSC	Space Force Space Systems Command
UN	United Nations

Nomenclature

Physics Constants

μ_E	Earth's gravitational parameter	$3.986\,004\,41 \times 10^{14}\ \mathrm{m^3/s^2}$
c	Speed of light in vacuum	$2.997\,924\,58 \times 10^{8}\ \mathrm{m/s}$
g_0	Earth's free fall acceleration at Earth surface	$9.806\,65\ \mathrm{m/s^2}$
J_2	Earth's J_2 coefficient	1082.63×10^{-6}
R_E	Earth's equatorial radius	$6.378\,137 \times 10^{6}\ \mathrm{m}$
T_s	Earth's Sidereal Day	$86\,164.1004\ \mathrm{s}$
W	Power density of the solar radiation near the Earth	$1360\ \mathrm{W/m^2}$

Symbols

α	Azimuth	rad
δ	Elevation	rad
γ	Flight path angle	rad
ν	True anomaly	rad
Ω	Right ascension of the ascending node	rad
ω	Argument of periapsis	rad
ρ	Density of air	$\mathrm{kg/m^3}$
φ	Phase angle	rad
A	Reference Area	$\mathrm{m^2}$
a	Semi-major axis	m
C_D	Coefficient of Drag	-
C_r	Radiation Pressure Coefficient	-
C_r	satellite's reflectivity	-
D	Drag	N
E	Eccentric anomaly	rad
e	Eccentricity	-
h	Magnitude of angular momentum	$\mathrm{m^2/s}$
i	Inclination	rad
K	Ballistic coefficient	$\mathrm{kg/m^2}$
M	Mean anomaly	rad
m	mass of the respective body in question	kg

n	Mean motion	rad/s
p	Semi-latus rectum	m
v	Velocity	m/s
v_{rel}	Relative velocity	m/s
V	Volume	m^3

Contents

Abstract

Space debris fragments smaller than 10 cm cannot be tracked from Earth and are generally neglected in conjunction and risk analyses because of this. However, these fragments pose a great threat, as they can lead to collisions. Currently, the threat that space debris poses on the space environment is getting larger, so methods to mitigate said debris need to be explored. The technique that was studied here, consisted of a passive spacecraft with a circular cross-sectional surface of a material, such as aerogel or foam, with the ability to decelerate and catch the debris fragments encountered. Given this choice, a capture analysis was carried out for such a potential technique. It was concluded, that the most favorable orbital settings for such a method, would be in the case of an explosion of an active or defunct spacecraft, as a direct reaction device. This scenario was then simulated using the orbital parameters of the Kosmos 1408 anti-satellite missile test. The results showed that for a spacecraft with a collector radius of 20 meters, 2 to 3% of the newly created fragments were caught, whereas, for a larger spacecraft with a radius of 100 meters, that number increased to up to 12%. The ideal deployment time for a spacecraft of 20 meters radius was found to be 12 hours after the fragmentation, whereas for 100 meters it was 6 hours. It was found that the capability of such a method is highly dependent on the catcher size, whereas deployment time has a smaller impact. Moreover, it was concluded that the performance of this technique is very sensitive to injection inaccuracies, as the number of fragments caught would be close to zero.

1

Introduction

If we were to live in a world where after every car crash none of the broken parts were cleaned up, it would reach a point where those parts would lead to more accidents and thus more car parts, until eventually, roads would become viably unusable. At this very moment, humankind finds itself facing a similar issue, not on roads, but in space. When talking about space debris, this phenomenon is often referred to as the ”Kessler Syndrome”, a popular term in orbit dynamics that describes a scenario where collisions lead to fragment generation and these fragments lead to more collisions. The result of the increase in the number of collisions leads to an exponential and self-sustaining increment of space debris (Kessler et al., 2010). This increase in space debris would at one point generate a high-risk situation for both new and existing missions, thus hindering the advance of space travel.

Given the large number of fragments in orbit, numerous (inter)governmental agencies and private companies are working to develop Active Debris Removal (ADR) methods to mitigate the current situation humankind faces. Nonetheless, these bodies only focus on cleaning up the trackable large debris. This means that an estimated 131 million fragments are left unattended (Lemmens & Letizia, 2022). Although fragments below 700 km altitude will eventually decay and burn up upon re-entry into Earth’s atmosphere, until that happens, which can take years depending on fragment conditions, these fragments are neglected in conjunction analyses, with obvious consequences.

For this reason, this study will focus on small space debris mitigation. To do this, two scenarios will be initially considered; an overall clean-up of space and a clean-up in the case of an existing breakup event, due to an explosion. The National Aeronautics and Space Administration (NASA) defines a passive method as one which does not require further active control after deployment (Caldwell, 2021). The study will examine the feasibility of using a passive spacecraft to clean up the small debris by analyzing a variety of aspects such as the time delay to reach the desired orbit and possible injection inaccuracies. This spacecraft will be input into the desired orbit and then an analysis of the number of fragments caught will be carried out. The simplicity of this design would make it revolutionary as it does not require active debris tracking or maneuvering to catch the debris. However, a concept such as this one has never been studied so it is unknown whether it would work. Therefore the primary goal of this study is to determine the feasibility of a method such as the one proposed. The specific research question to be answered is the following:

> **“How effective would a passive removal method be in mitigating space debris smaller than 10 cm in a conjunction analysis?”**

In order to successfully answer this question a set of sub-questions will be looked at.

- What would the concept of such a spacecraft look like?
- What would be a favorable orbital setting in which this method would be successful?
- What would be an effective size for the catcher vehicle?

- When would the ideal deployment time be?
- What would be the yield of the system?
- Could such a method still work given injection inaccuracies?
- Which momentum values would such a spacecraft encounter?

To answer this research question and sub-questions, several aspects will addressed. To begin with, the relevance and justification for the research will be presented in a detailed manner. This will be followed by a description of the space debris population including the current environment, the nature of the debris, a specific look into the behavior of debris at Low Earth Orbit (LEO) as well as threats and the future evolution of debris. Next, Chapter 3 will look into existing debris removal techniques, here all techniques will be considered including those used for larger space debris so long as deemed applicable to small debris. This chapter will also provide a detailed description of the debris removal idea used for this study. The following chapter will look at the astrodynamics of both the debris and the removal spacecraft. This will look at reference frames, coordinate systems, governing equations, orbit propagation and integration as well as assumptions made for the astrodynamics of the problem and preliminary numbers for all cases. Chapter 6 will provide insight into the satellite breakup as well as the explosion geometry and fragment data generation. Next, the conditions for the conjunction analysis will be presented. Chapter 8 will present an overall overview of the developed methodology in the form of flow charts. Chapter 9 will look at the verification and validation of the model used as well as all the parts implemented in the code. The proceeding chapter will present the results obtained from the study as well as a discussion of the various results. Finally, the last chapter will present the conclusions of the study including the feasibility and limitations as well as recommendations for further studies.

2

Relevance and Justification

Since the beginning of the space era in 1957, 13,100 satellites have been launched into an Earth orbit. According to the European Space Operations Centre (ESOC), 8,410 of those are still in space, however, only 5,800 are still functional (ESA, 2021d). This means that there are 2,610 satellites in space that should not be there, posing an increased risk that could be avoided by removing them. Over the past years, more awareness has been brought to the current situation of space debris and the risk it poses to future generations. This chapter will concern itself with the relevance of the study at hand and the justification of the research. To do this the consequences of staying on the current track we are on, along with the diverse courses of action that are being taken, will be looked at. While this chapter will only focus on the rationale of the investigation carried out in this study, a more in-depth description of the space environment, measurements and possible removal techniques will be presented in Chapters 3 and 4.

2.1. Debris Evolution

According to Lemmens and Letizia (2022), the average number of non-deliberate fragmentations over the past two decades has been 11.7 fragmentations per year. Looking only at catastrophic fragmentations resulting in ”complete destruction of the target and the impactor”, Lemmens and Letizia (2022) made a prediction for the evolution of catastrophic collisions in LEO of objects larger than 10 cm if no action is taken. The results of this prediction can be seen in Figure 2.1. It can be seen that if nothing is done, in the coming century (Year 2125) the cumulative number of catastrophic collisions will increase until it reaches about 320 collisions. Nonetheless, the concerning part is that if we were to stop all future launches, the situation would result in about 70 collisions.

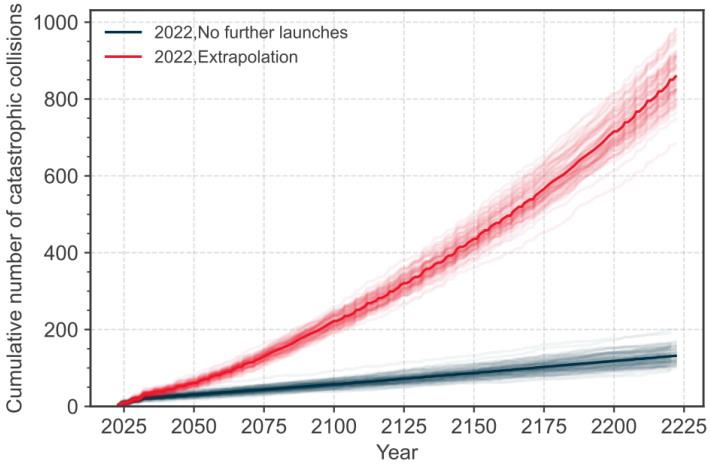

Figure 2.1: Cumulative number of collisions in LEO in the simulated scenarios of the long-term evolution of the environment (Lemmens & Letizia, 2022).

The situation depicted in Figure 2.1 is the reason why a set of measures have been put into place, to avoid said catastrophic scenario. These measures are passivation, mitigation and ADR.

2.2. Passivation

ESA (2021a) defines passivation as the “deactivation of satellites’ power systems and batteries and venting leftover propellant to reduce the risk of explosion in the future”. As can be seen in Figure 2.2, during the past 10 years, almost one-third of the causes for fragmentation events can be attributed to the leftover propellant. While breakup events related to electrical causes only comprise 5.26% together with propulsion-related breakups they account for almost 40% of the breakup events. This is why passivation is such an important measure in decreasing space debris. Through the depletion of this excess energy and propellant, a large number of breakup events could be avoided. A historical overview of the relative share of breakup causes since 1960 will be provided in Chapter 3.

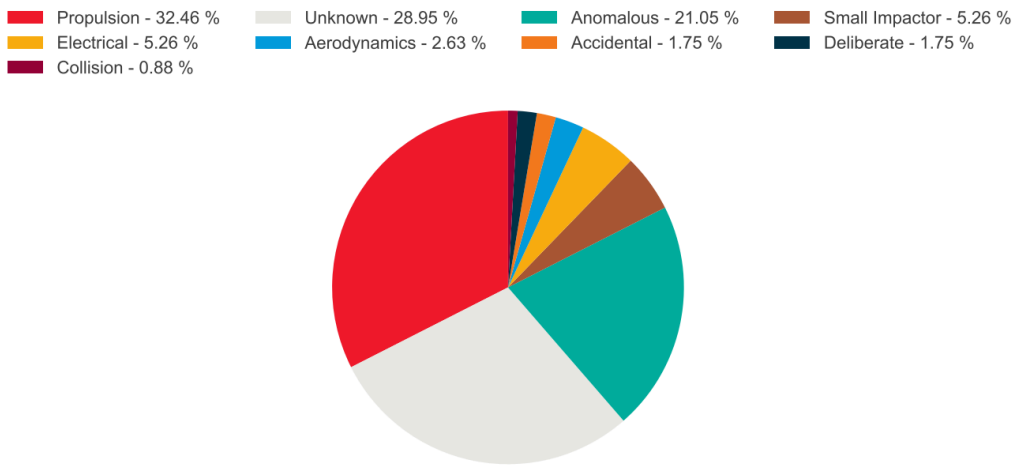

Figure 2.2: Event causes and their relative share for all past fragmentation events in the last 10 years (Lemmens & Letizia, 2022).

2.3. Mitigation

In 1994, the United Nations (UN) regarded space debris as a priority to be addressed for the first time ever. Each year after, discussions took place until a decision was made to establish a set of guidelines in 1996. This led to the generation of a technical report on space debris in 1999 (UNOOSA, 2010). Over the proceeding years, the UN made it its mission to make sure these voluntary guidelines were adopted. Furthermore, it required member states to research and report on space debris. Given the continued increase of space debris in 2002 the Inter - Agency Space Debris Coordination Committee (IADC) provided a set of guidelines to attempt to limit the further generation of space debris (UNOOSA, 2010). Nonetheless, space debris continued to increase.

In January of 2007, the breakup of the FengYun-1C satellite increased trackable space debris by 25% (ESA, 2021d), leading to the approval of said guidelines by the member states in 2007. One of these guidelines focused on limiting “the long-term presence of spacecraft and launch vehicle orbital stages in the LEO region after the end of their mission” (UNOOSA, 2010), by requiring spacecraft in LEO to re-enter the atmosphere and burn up within 25 years after completing their mission (UNOOSA, 2010). In November 2022, the Federal Communications Commission (FCC) voted to change that number to merely 5 years. An example of the importance of space debris mitigation can be observed in Figure 2.3. Action must be taken in order to avoid complete pollution of the environment.

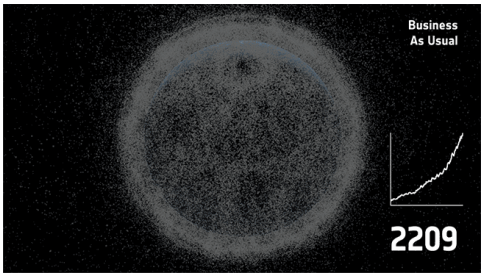

(a) Space debris evolution in the year 2209 without any space debris mitigation.

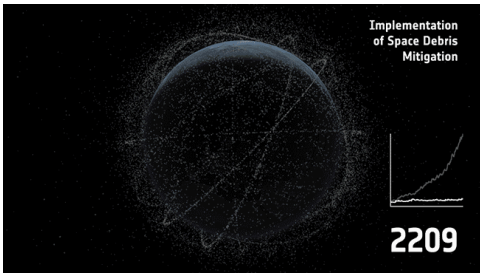

(b) Space debris evolution in the year 2209 with space debris mitigation.

Figure 2.3: Space debris environment business as usual versus with space debris mitigation (ESA, 2022).

2.4. Active Debris Removal

In the preceding sections, different ways of avoiding the further generation of space debris have been presented. Nonetheless, Figures 2.1 and 2.3 made the issue clear: no matter how much the guidelines are followed, space debris will continue to increase as more spacecraft get put into orbit. For this reason, a further step has to be taken: debris has to actively be removed from orbit to avoid further generation of new debris. Active Debris Removal (ADR) is defined as “the removal of obsolete spacecraft (satellites and rockets) or fragments of spacecraft that have broken off satellites and rockets, through an external disposal method” (May, 2021). Through a combination of passivation, mitigation and ADR an improved situation could be expected, there is no guideline that on its own can make enough of an impact to improve the environment.

When talking about ADR one often refers to trackable versus non-trackable and large versus small debris. At the moment this distinction is made at 10 cm, where LEO fragments below about 10 cm are not currently tracked by observatories on Earth, meaning that when collision predictions are made there are 131 million fragments which are not taken into account (ESA, 2021e). Similarly, small objects are considered fragments below 10 cm whereas large fragments are those larger than 1 meter. Large fragments are responsible for the majority of new space debris generation but small space debris poses the largest threat. To put it into perspective one can think of a million bullets flying through space with no knowledge of when they could hit your spacecraft. In order to quantify the risk, (ESA, 2021e) calculated the mean time between impact with a debris for satellites of different cross-sectional areas. They predicted that at an altitude of 400 km, the mean time between impact for a debris object of 10 cm and a satellite with a cross-sectional area of 100 m^2 would be 15,000 years. For a satellite of cross-sectional area of 30 m^2 with a large object that time decreases to 4,000 years. Although these values seem very optimistic, one has to take into consideration the combined profile area of the satellites orbiting Earth at the moment. Using these numbers (ESA, 2021e) calculated that a catastrophic collision is expected to occur every 10 years.

2.4.1. Large Debris

At the moment, most ADR projects consider large spacecraft. These aim at removing large defunct satellites or other large items as a way to avoid further debris generation and remove high amounts of mass from orbit. Most of the methods explored include contact methods, where the main technique of removal is through coming in close contact and physically catching and removing the object. Some examples of this include projects such as Airbus’ removeDEBRIS (Airbus, 2021) where a tether was used as a means of removing the debris, reasonDEBRIS which consisted of a space net used to catch a large debris fragment (Aglietti et al., 2020). Another project is ClearSpace-1, the first project contracted by ESA to remove an existing debris fragment. This project consists of using four robotic arms which grab the inactive spacecraft (Biesbroek et al., 2021). Studies carried out by NASA and ESA show that in order to make a significant impact and stabilize the environment, five to ten large objects have to be removed from LEO yearly (Lemmens & Letizia, 2022).

2.4.2. Small Debris

Given the difficulty in tracking small space debris, not as many efforts have been made to mitigate these debris fragments. Companies such as LeoLabs are working on bridging the gap of the size of trackable debris by tracking debris as small as 2 cm (McKnight, 2021). This would help the mitigation of said fragments. However, there are still a number of studies that have acknowledged the issue that small debris fragments pose and come up with possible theoretical solutions. Some options include the use of a space-based laser that uses ablation to decrease the energy of the debris which causes them to lose altitude and burn up upon atmospheric re-entry. This option was studied for small fragments by Pieters and Noomen (2020) and Alves Teixeira et al. (2022). In their report (Alves Teixeira et al., 2022) also looked at other possible options such as a net with a similar concept to the one presented in this study.

Another option is based on the usage of an ion beam, a contactless method that makes use of bi-directional plasma to decrease the velocity and thus altitude of the debris with the same goal as the laser. Nets have also been explored as a way to mitigate small fragments, however, the mesh would have to be very small to be able to catch the required debris. Another method is spraying foam in order to increase the size of the debris causing an increase in atmospheric drag and faster de-orbiting. An additional option to catch small space debris is a disk-shaped surface of aerogel with a collection chamber that catches debris based on contact. This option was obtained as a result of a literature review conducted prior to this research in which Carceller (2021) identified this as the most promising option. This will be explored further in this study.

2.4.3. Implementation Status

As aforementioned, there are no missions which have been launched as of this moment. The first expected mission will be Clearspace-1. However, given the amount of mass in space, the mission will consider the 112 kg Vespa upper stage (Biesbroek et al., 2021). However, it is expected that this will be the first of many as agencies and companies around the world focus on neutralizing the threat that space debris poses.

3

Space Debris Environment

This chapter will concern itself with the debris population looking at the origin of the debris; this will look at the debris originating from fragmentation versus that originating from other sources. Then it will look at the size of the debris and the density distribution of the debris in various orbits. Nonetheless, it is important to clarify that space debris is ”defined as all man-made objects including fragments and elements thereof, in Earth orbit or re-entering the atmosphere, that is non-functional.” (ESA, 2021e).

3.1. History

The history of the debris environment can be traced to the beginning of what is known as the space age, namely the launch of Sputnik 1 on the 4^{th} of October 1957 (Lemmens & Letizia, 2022). Since then, objects in space have been increasing with more objects being added into new orbits than ever. This can be attributed to a number of things such as more affordable space missions with concepts such as cubesats and the large number of constellations being sent into space. Figure 3.1 shows the evolution of the objects in space by object type. From this figure it can be seen that in the past five years the growth rate of objects in space has increased at a significantly faster rate. Moreover, most debris originates from payload missions related objects, payloads, rocket fragmentation debris and unidentified objects. Taking a look at unidentified objects, it is important to keep in mind that Lemmens

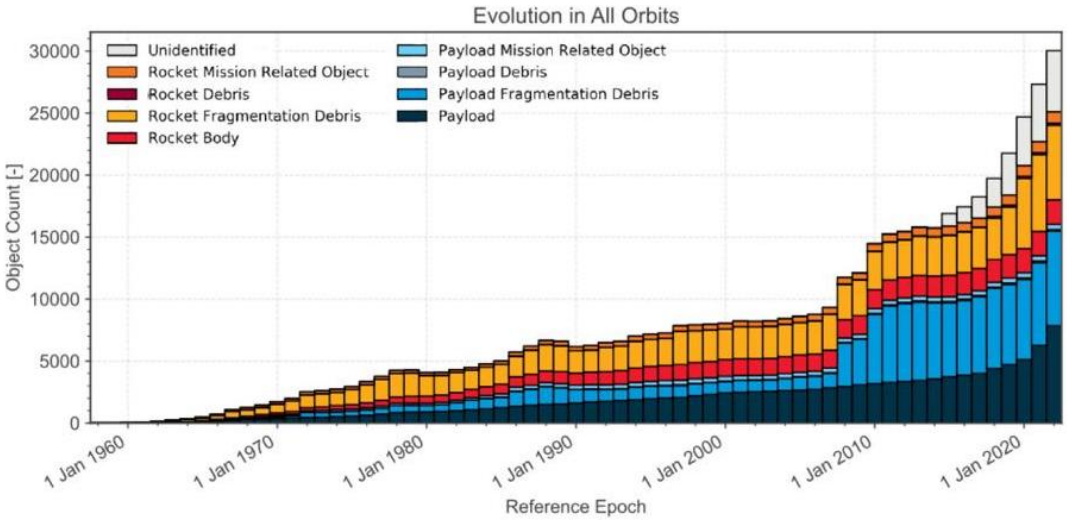

Figure 3.1: Evolution of number of objects by object class since January 1960 based on object type (Lemmens & Letizia, 2022).

and Letizia (2022) notes that the data is limited to catalogued and asserted objects, and hence at any given epoch limited to the capability of the space surveillance system in use at the time. A secondary effect hereof is that when new objects are detected due to increased sensor performance, they can

generally not be traced back to an event or source and become classified as unidentified. Meaning that these objects are not necessarily new objects in the space environment but rather newly discovered.

3.2. Fragmentation Events

When looking at the consequences and risks of space debris, it is important to look at the evolution of space debris after a fragmentation event. There are several examples which can be looked at, but in either case, the result is the same. The debris cloud is initially very condensed and then gradually spreads out across the globe. Figure 3.2 shows the perigee, apogee and period of the tracked debris one day after the explosion of Kosmos 1408 which took place on November 2021. As can be seen, one day after, the debris cloud has spread resulting in a variety of different orbits, some even 300 km above the original apogee altitude. The agglomeration of the debris fragments, at the time right after the fragmentation event, poses the best-case geometry to catch the small fragments. For this reason, Kosmos 1408 will be studied as a means to avoid the rapid spread around the globe. The study will reveal the feasibility of such a device in different cases such as a general situation as well as explosions and collisions, focusing on the explosion scenario.

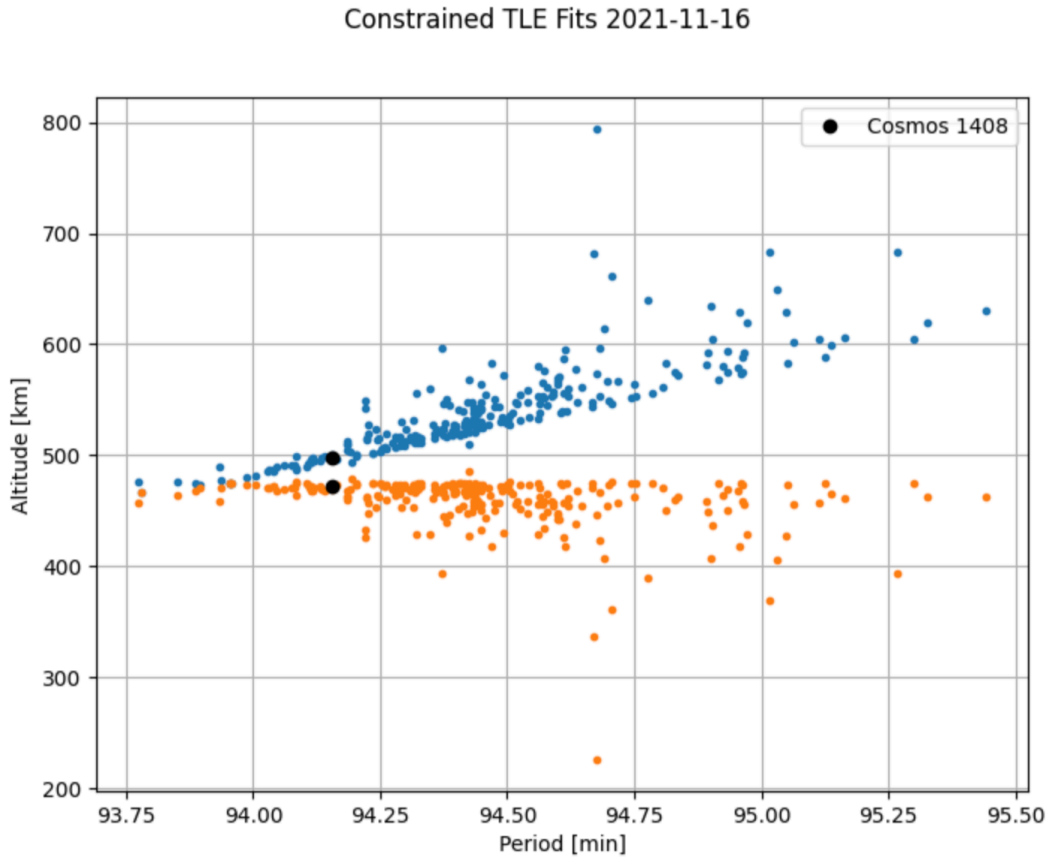

Figure 3.2: Gabbard diagram of LeoLabs debris fragments from Kosmos 1408. Blue dots denote the apogee while the “partner” orange dots denote perigee for the same object. The y-axis denotes the pericenter and apocenter altitudes. The thick black dots represent the original situation before the explosion (McKnight, 2021).

3.3. Fragmentation Debris

The issue of space debris has gained importance during the past few years due to its growing severity. This section will present the origin of fragmentation debris. The eight categories that ESA now divides up fragmented space debris into are: unintentional, aerodynamics, anomalous, collision, deliberate, electrical, propulsion, and unknown. Figure 3.3 depicts these categories, which will be explored in more detail later in the chapter.

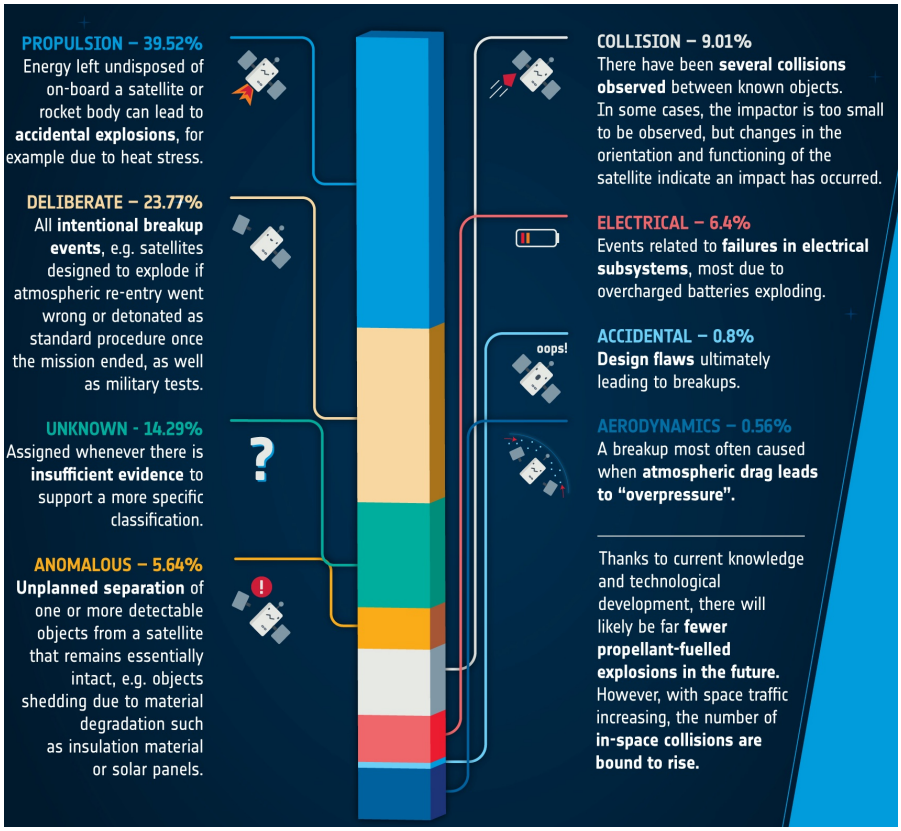

Figure 3.3: Percentage of fragmentation debris events in the history of space, along with a description of the diverse categories (ESA/UNOOSA, 2020).

It is evident from studying the evolution of fragmentation events that more awareness is being brought to the dangers of space debris. This can be seen from the reduction in fragmentation events. Figure 3.4 depicts the number of fragmentation events since 1960 in five-year bins. It can be observed that the peak was reached in the five-year period from 2005 to 2010 and has since been declining. Although we are only halfway through our five-year bin it can be expected that 2020 to 2025 will have fewer fragmentation events than the previous bin. So far since 2020, more than 50% of fragmentation events were unidentified, with propulsion, electrical, collision and deliberate accounting for the remaining events. Despite declining incidences, there is still a long way to go in terms of the mitigation of space debris.

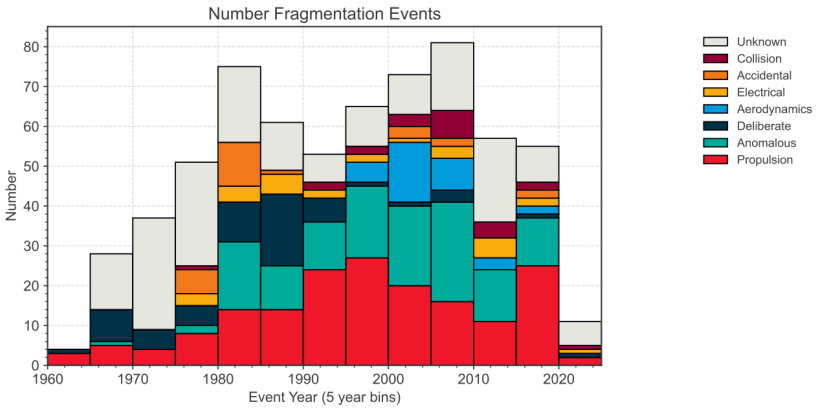

Figure 3.4: Number of fragmentation debris events since 1960 based on fragmentation debris categories (Lemmens & Letizia, 2022).

As seen in Figure 3.4, the bulk of fragmentation occurrences in recent years have been classified as propulsion, anomalous, and unknown, with accidental, electrical, and deliberate fragmentation events being near nil. In contrast, a significant percentage of fragmentation events in the early years of spaceflight was deliberate. Additionally, it is evident that fewer fragmentation events have occurred in recent years, which is probably a result of the stricter enforcement of debris mitigation legislation.

Although there are fewer fragmentation events, there is nevertheless a rise in the number of space debris (Figure 3.1), with the payload, payload fragmentation debris, rocket fragmentation debris, and unknown all contributing equally to the total.

3.3.1. Propulsion

Since the dawn of the space age, nearly 40% of fragmentation debris has been traced back to propulsion (Figure 3.3). This is due to excess energy which is stored in the satellite or rocket; this energy can lead to explosions, resulting in a large number of debris particles. This type of fragmentation debris can be avoided by getting rid of excess energy. For this reason, the requirement of passivation has been put into place, meaning that excess energy must be discarded, whether by emptying propellant tanks or disconnecting batteries, depending on the spacecraft's power source (ESA, 2021d).

3.3.2. Deliberate

The second cause, which accounts for nearly a quarter of all space debris, is deliberate; this can include testing or planned explosions in case of failed re-entry attempts, as well as a measure implemented as an end-of-life strategy. As shown in Figure 3.4, these types of fragmentation debris have decreased as a result of tight regulations and our growing understanding of the dangers of space debris. Deliberate break-up events were mostly used in the early years of spaceflight when debris was not as much of a concern as it is now.

A well-known deliberate incident that increased the amount of space debris by over a quarter and raised awareness of the issue of debris, was China's FengYun-1C anti-satellite test in 2007. Even if these types of incidents are declining, there is still more work to be done in terms of space law, as evidenced by the Russian anti-satellite missile test that occurred on November 15^{th}, 2021. So long as no hard laws are made and repercussions are suffered for the responsible parties, catastrophes such as those will continue to occur.

3.3.3. Unknown

Unfortunately, the origin of a large number of debris fragments is unknown; this can be attributed in part to the limitations in sensors tracking debris. However, the lack of knowledge about the properties poses a threat to space debris mitigation given that something which cannot be traced back to the origin cannot be safely mitigated. Space debris mitigation techniques could prove useful for said debris and would be aided by improving tracking methods as these would give a better insight into composition and size. Nonetheless, Lemmens and Letizia (2022) notes that the data is limited to catalogued and asserted objects, and hence at any given epoch limited to the capability of the space surveillance system in use at the time. As a consequence, when new objects are detected due to increased sensor performance, they can generally not be traced back to an event or source and become classified as Unidentified.

3.3.4. Collision

Collisions account for 9% of all sources of space debris (Figure 3.3); this figure is likely to rise as more objects are launched into space, increasing the risk of collision. Large constellations are an example of a potential collision threat.

The first unintentional collision between two satellites took place in 2009 (Kelso, 2009). The collision occurred between the defunct Russian communication satellite Cosmos 2251 and the active US Iridium 33, thus being named the Iridium-Cosmos collision. Despite the fact that a close approach was predicted, no intervention was carried out (Kelso, 2009). As seen in Figure 3.5, the collision presented a valuable overall view of how quickly debris spreads along the orbit. This incident helped raise awareness of the rapidly increasing threat of future collisions as the number of objects in orbit grows.

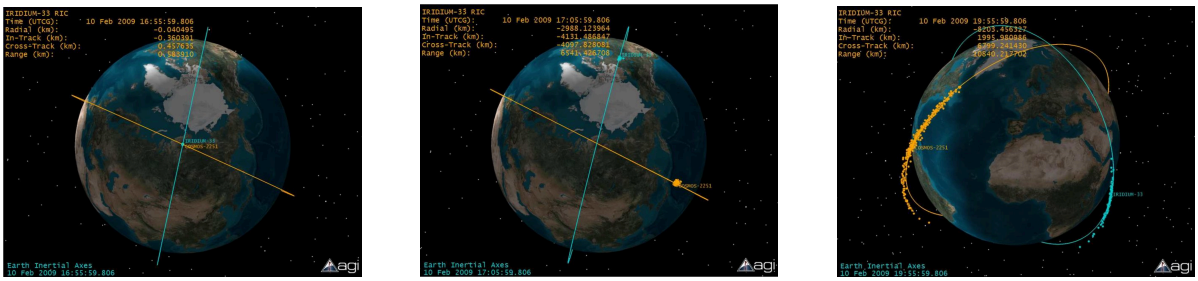

(a) At the time of the collision. (b) Ten minutes after the collision. (c) Three hours after the collision.

Figure 3.5: Evolution of debris clouds originating from the Iridium-Kosmos collision over time (Kelso & Gorski, 2022).

3.3.5. Electrical

In terms of electrical fragmentation, it stems from problems that onboard electrical systems and subsystems may have encountered. The vast majority of incidents are caused by overcharged batteries exploding. More than 6% of fragmentations are caused by electrical issues (ESA, 2021d).

3.3.6. Anomalous

The anomalous object types are composed of fragments that have been detached from the satellite but have not been damaged. This could include fragments detaching as a result of the material's degradation. An example of this would be materials used for insulation or solar panels (ESA, 2021d).

3.3.7. Accidental

Accidental space debris is a problem brought on by poor design. This fault in the design could cause the satellite to fragment. Only a small portion of debris falls into this category since satellites undergo rigorous testing before entering orbit.

3.3.8. Aerodynamics

Aerodynamic fragment types are due to a variety of different forces, the main one being drag. When exerted to a high amount of atmospheric drag, there is an excessive amount of pressure applied to the spacecraft. This high pressure can lead to fragmentation and thermal load (Lemmens & Letizia, 2022).

3.4. Non-Fragmentation Debris Population

Whereas the debris originating from fragmentation events was discussed there are also particles that cannot be associated with fragmentation events. These particles are known as non-fragmentation debris and are another type of debris. This debris can be produced by a variety of events and sources, such as solid rocket motor firings, reactor core ejections, and others. All of these, as the name suggests, are the result of events other than spacecraft fragmentation. The following subsections will provide a general overview of the various sources and types (ESA, 2021a).

3.4.1. Solid Rocket Motor Firings

Solid rocket motor firings are the most important source of non-fragmentation debris. Over time, there have been almost 2,500 fragments catalogued which can be traced back to solid rocket motor firings. The way this type of debris is generated is that aluminium oxide (Al_2O_3) is released. This leads to the release of dust in the size range of micrometers and slag particles in the size range of millimeters to centimeters (ESA, 2021c). Given the small size of these particles, they would be categorized as small space debris and would thus lead to the lack of tracking and cataloguing of said particles. However, for the ones tracked, Figure 3.6 shows that the propellant mass expelled by solid rocket motor firings has increased over the past few years but the number of firings, depicted by the dots on the graph, appears to have decreased.

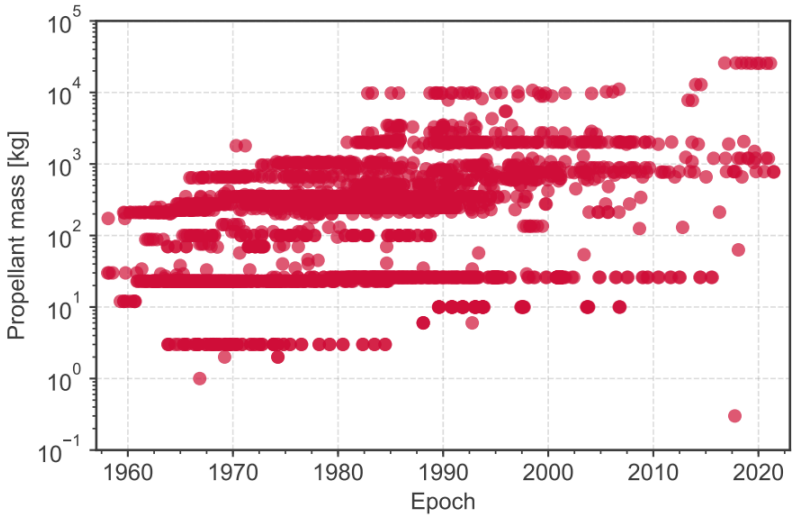

Figure 3.6: Solid-motor firings since 1960 in terms of propellant mass (Lemmens and Letizia, 2022).

Similarly, when looking at the distribution of the number of firings over the years, it can be observed that the largest number of firings over time has occurred in LEO. This can be seen in Figure 3.7 where on average approximately three-quarters of the firings have been in LEO. However, in recent years that number has been reduced with the most recent firings occurring in other orbits. The decrease in the number of firings can be attributed to the compliance with the instilled debris mitigation guidelines (Lemmens & Letizia, 2022).

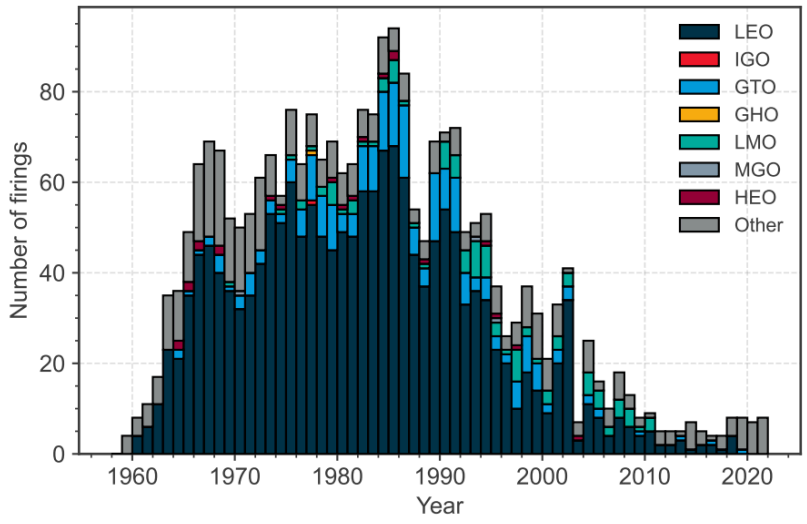

Figure 3.7: Orbital distribution of solid-motor firings since 1960 in terms of propellant mass (ESA, 2021e).

3.4.2. Ejection of Reactor Cores

Another important source of non-fragmentation debris is that generated due to the ejection of Buk reactor cores. It was catalogued that the coolant of the reactor released droplets into the space environment on 16 separate occasions. Nonetheless, all of these occasions could be traced back to Russian radar satellites that were decommissioned in the 1980s (ESA, 2021a).

3.4.3. Other Sources

Non-fragmentation events are not only limited to those mentioned above, there are numerous other reasons which could lead to an increase in non-fragmentation debris. Human influence and action

have played a large role in some of the increase in said type of debris. An important incident which had a big influence on the increase of non-fragmentation debris was a communication test carried out in the 1960s during the Midas mission. The test conducted in this mission involved releasing a large number of thin copper wires into the space environment. This event led to a large increase in the existing space-debris population (ESA, 2021a) known as “West Ford Needles”.

According to ESA, 2021a other sources which can lead to non-fragmentation debris include but are not limited to the degradation of surfaces as a result of exposure to ultraviolet light, and impacts with atoms and small particles. Both of these cases lead to a generation of space-debris particles that tend to be micrometer- to millimeter-sized. Some of these particles could be objects such as paint and other materials found on the surface of spacecraft (ESA, 2021a).

3.5. Other Threats

While fragmentation events are one of the biggest concerns when regarding space debris it is far from the only issue that space debris poses. Space debris is constantly flying through space encountering spacecraft and damaging them, although it may not always result in a failure of the system, enough collisions with items such as solar panels could result in damages which could lead to a malfunction. Figure 3.8 shows a real-life example of the damage space debris can do to a solar panel.

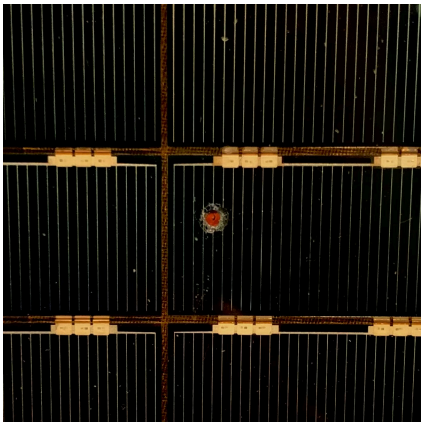

Figure 3.8: Picture taken by P.Carceller Suarez of Hubble solar panel with impact area by space debris.

4

Existing Removal Techniques

Many removal techniques have been proposed and tested over the years, but no ADR missions have ever taken off. The first mission, ClearSpace-1, is scheduled to launch in 2025 (Biesbroek et al., 2021); if successful, this could kickstart a new movement, paving the way for future ADR missions. The various methods, both contact and contactless, will be examined in this section. Similarly, a foundation will be established in order to obtain the best removal methods capable of successfully capturing small debris fragments in LEO in the event of a fragmentation event.

4.1. Basis for Removal Method

To be able to select a method that can carry out the aforementioned tasks, it is critical to establish a foundation upon which the removal method must operate. This will examine the catchment capacity in terms of size and efficiency. This will also look at operational capabilities such as orbit geometries.

1. **The removal method must be able to interact with debris 10 cm or smaller in size.** Because the study is concerned with active debris removal of small debris fragments, this is critical to the study's success and will be regarded as the primary criterion for method selection subsequently.

2. **The removal method should be efficient in terms of the number of objects removed from orbit.** Given that small debris fragments do not constitute a significant portion of the mass found in space, the removal method must be capable of collecting a substantial number of objects in order to bring about change in the space environment.

3. **The removal method shall have longevity allowing it to collect debris for multiple orbit geometries**. Proven that this technique was to be successful, it would be beneficial to be able to operate in various orbit geometries. This way it would be ensured that if another breakup event occurs, the ADR method would be ready to mitigate the risk as soon as possible.

4.2. Contactless Methods

This section will focus on ADR methods which do not come in touch with debris fragments.

4.2.1. Laser

The laser method is a contactless method that has two applications. The first possible application is using it as a ground-based laser (Scharring et al., 2021) while the second option is a space-based laser (Pieters & Noomen, 2020). As this study concerns itself with debris fragments of 10 cm and smaller, only the space-based laser will be considered. This is due to the fact that given the size of the fragments, they cannot be detected from Earth rendering the ground-based laser inefficient.
The space-based laser utilizes ablation as a way to slow down debris fragments, resulting in a reduction in altitude and thus an atmospheric burn-up upon re-entry. To detect debris, it has an onboard target acquisition system that identifies which debris fragments could be targeted by the space-laser (Pieters & Noomen, 2020).

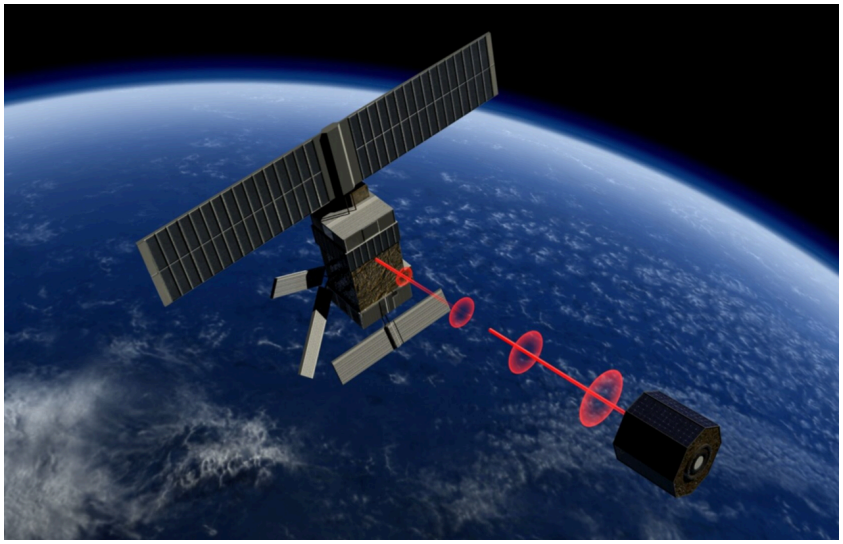

Figure 4.1: Artist illustration of a laser acting on space debris (ESA, 2021b).

4.2.2. Ion Beam Shepherd

The ion beam is a different contactless technique (Figure 4.2) that makes use of a bi-directional plasma beam as a means of decelerating the debris to obtain a decrease in altitude and eventually causing the debris to burn up upon atmospheric entry (Takahashi et al., 2018). This technique calls for a satellite from which plasma beams are fired. In this concept one of the plasma beams is aimed at the debris and the other plasma beam is directed in the opposing direction to ensure the distance between the debris and the satellite remains constant. Laboratory experiments showed that a deceleration of the debris along with a zero net force on the thruster can be achieved, this concept has yet to be tested (Takahashi et al., 2018).

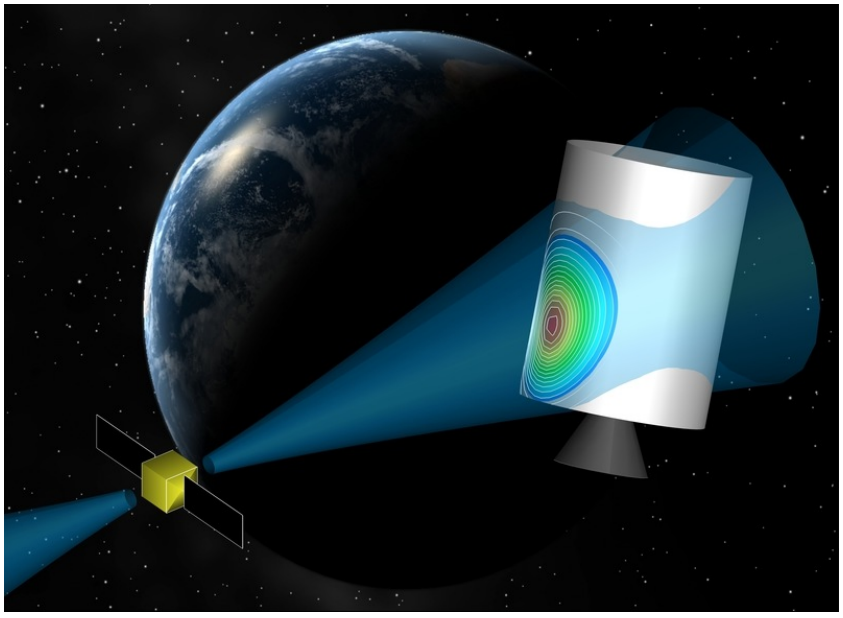

Figure 4.2: Depiction of ion beam shepherd concept (UPM, 2021).

4.2.3. Vacuum

When one thinks of cleaning something up, a vacuum cleaner often comes to mind, which is why this section was included. Creating a vacuum requires air to be removed from within a volume by making use of a vacuum pump or through the reduction of pressure making use of a fast flowing of fluid

(Britannica, 2021). Nevertheless, there is no air in space since it is a near vacuum. There is currently no known technology with the ability to create a vacuum within the spacecraft to vacuum space debris so this method will not be considered (Carceller, 2021).

4.2.4. Gravity Tractor

The gravity tractor concept has been widely analyzed when looking at asteroid deflection techniques. It entails flying a spacecraft close to an asteroid for an extended period of time, gradually changing the asteroid's path because of the gravitational attraction between both the asteroid and the spacecraft (Bonilla, 2015). Figure 4.3 depicts the use of a gravity tractor as a means to remove asteroids. In said scenario, the asteroid would be replaced by space debris fragments. Nevertheless, this has not yet been researched as an ADR method.

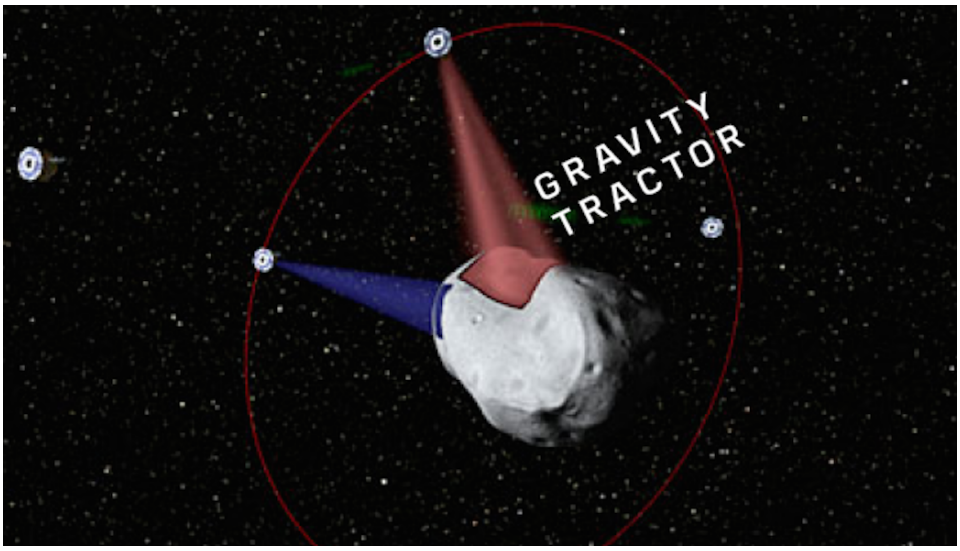

Figure 4.3: Gravity tractor with an asteroid (Bonilla, 2015).

Newton's law of gravitation states that the gravitational force is proportional to the masses of the two objects as well as the inverse of the square of the distance between their centers of mass (Wakker, 2015). Taking debris of 10 cm and smaller into account, the mass of these objects would be very small enough such that the gravitational attraction would in turn be very low. Even though the distance could be reduced, achieving the desired closeness in a controlled way would be difficult given a large number of particles with varying scattering throughout an orbit, so individual particles could most probably not be targeted without interacting with the other particles. This technique would thus necessitate a rendezvous situation, that is far too expensive in terms of Δv and will thus be ignored (Carceller, 2021).

4.2.5. Electric and Magnetic Field

A study carried out at the University of Utah aimed at moving non-magnetic objects through the use of electromagnets. This was studied with a focus on space debris removal focusing on electrically conductive debris fragments. The way that this was achieved, was through the use of magnetic induction, namely using a magnetic field to induce what is known as eddy current (Pham et al., 2021). The end result would be turning the conductive debris fragments into electromagnets. Once this is achieved, the debris fragments can be slowed down and even moved so they can burn up in the atmosphere (Pham et al., 2021). This study was tested in water as an attempt to mimic space and it was successful. However, more tests would have to be carried out to see if this would be successful in space so this method will not be considered (Pham et al., 2021). Moreover, for debris made out of non-conductive materials, such as paint flecks, this would not work.

4.2.6. Foam Spray

The foam spray method was investigated as a method of ADR. It consists of a satellite that sprays foam that creates a carcass around the debris increasing the drag of the debris and forcing it to deorbit (Carceller, 2021). Simulations were performed to demonstrate the effectiveness of this method. This type of ADR could be effective if it worked on smaller debris fragments (Carceller, 2021). While one can imagine that would work for the ”larger” small debris in the measure of cm but the effectiveness on mm-sized fragments could be limited (Andrenucci et al., 2011). This method was investigated in literature and is depicted as seen in Figure 4.4. However, in order to spray the foam, a technique such

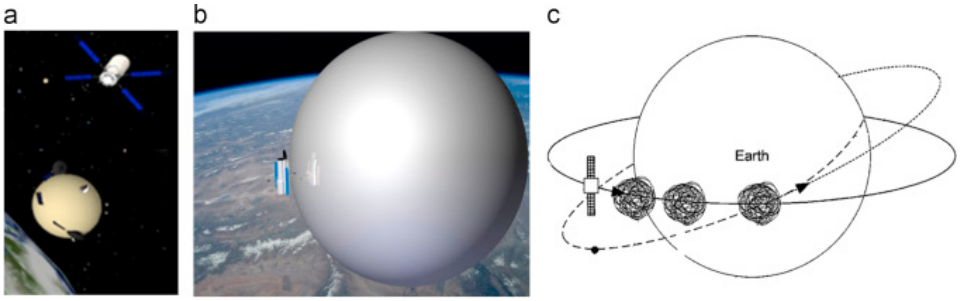

Figure 4.4: a. Concept based on spraying foam and increasing drag of debris b. Close up of foam spraying c. Dynamics of debris fragments with foam (Shan et al., 2016).

as this would mandate the spacecraft and debris fragments to be in rendezvous. This could pose a limitation for small debris fragments because the number, size, and high relative velocities would render spraying foam at individual fragments expensive in terms of Δv (Carceller, 2021).

4.3. Contact Methods

This section will focus on ADR methods that come directly in contact with debris. This can be utilized to both capture and decelerate the debris fragments. Existing contact methods that are thought to be designed to capture small debris fragments will be investigated (Carceller, 2021).

4.3.1. Robotic Arms

The first contact method which will be analyzed is that of robotic arms, such as for the ClearSpace-1 mission seen in Figure 4.5.

Figure 4.5: Illustration of Clearspace-1 (Biesbroek et al., 2021).

The method employed in the ClearSpace-1 mission is made up of four robotic arms that seize the inactive spacecraft (Biesbroek et al., 2021). Nonetheless, the use of one robotic arm has been investigated as a method of debris removal such as that depicted in Figure 4.6. This requires an appropriate protrusion that can be grappled (Carceller, 2021). The use of robotic arms would be ineffective for smaller space debris and therefore will not be considered for the context of this research (ESA, 2021c).

Figure 4.6: **a.** Illustration of a robot arm in space **b.** Picture of a real robot arm testing **c.** Single robot arm depiction (Shan et al., 2016).

The Space Vulture concept is another type of space debris removal method consisting of a chaser that catches the debris and then pulverizes it to be repurposed as raw resources (El-Rashid et al., 2021). Figure 4.7 shows a representation of this concept.

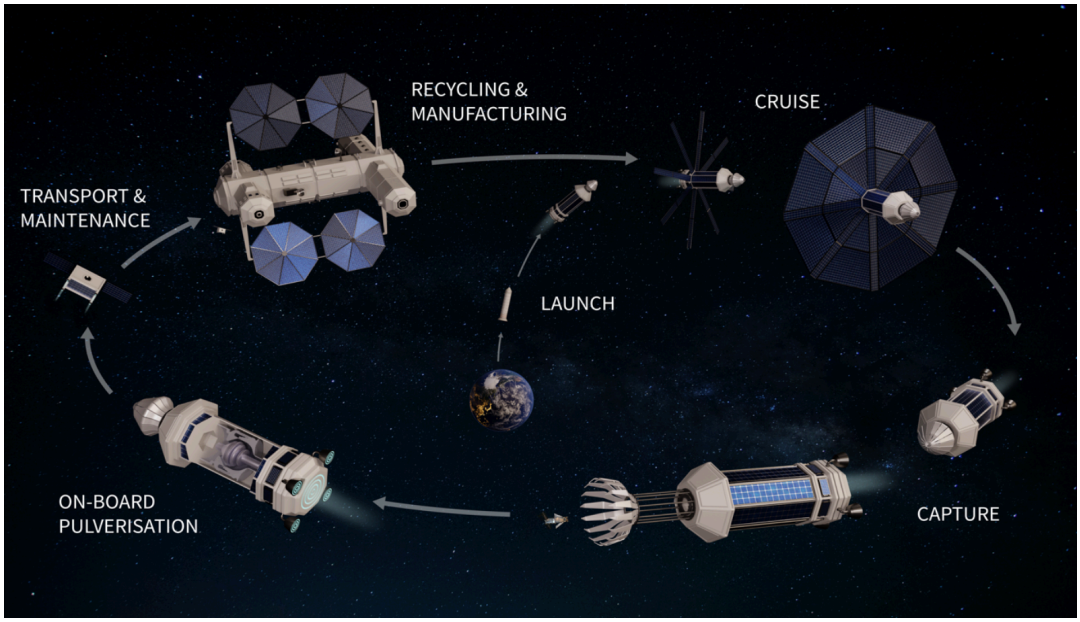

Figure 4.7: Illustration of Space Vulture Process (El-Rashid et al., 2021).

4.3.2. Tether

The use of tethers in space applications has been extensively researched for a variety of applications. Numerous space agencies, including ESA, NASA and JAXA, have investigated the possibility of employing a tether to capture space debris. This method works by connecting the tether to the debris and pulling it (Wormnes et al., 2013). There are various versions of tethered concepts, several of which are depicted in Figure 4.8.

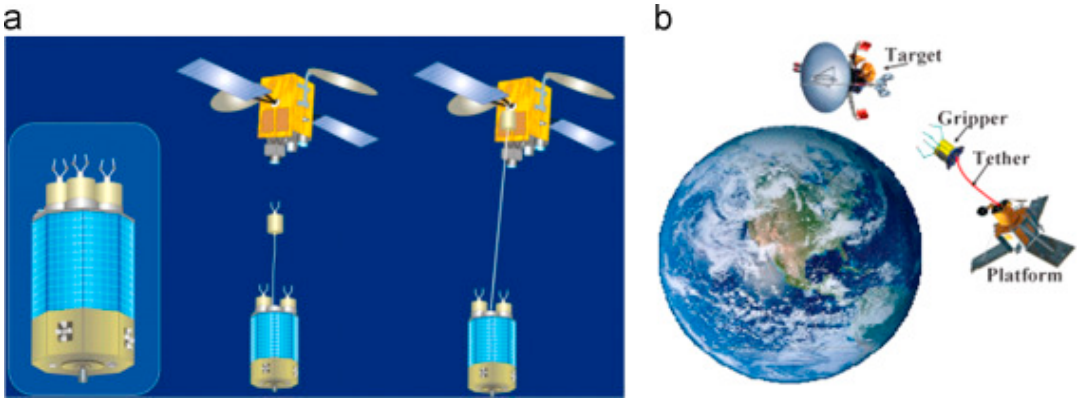

Figure 4.8: a. Illustration of tethered concept b. Illustration of tethered concept with gripper in space (Shan et al., 2016).

Regardless of the complexity of the dynamics, tethers have been discussed as a promising method (Wormnes et al., 2013). Airbus Defense and Space (ADS), for example, has been testing and developing tethered systems with the RemoveDEBRIS Harpoon (Airbus, 2021). During the test phase, the satellite successfully deployed a harpoon (Figure 4.9) with a tether system. Nonetheless, this method was designed for large debris fragments and will not be considered for the purposes of this research (Carceller, 2021).

Figure 4.9: Illustration of RemoveDEBRIS ADS Harpoon concept (Airbus, 2021).

4.3.3. Space Net

This method of ADR involves the deployment of a net from a satellite, where it then captures the debris in question. Even though this method has been solely regarded for large debris fragments, it may be utilized for fragments smaller than 10 cm. The reasonDEBRIS satellite, launched to the ISS in 2018, was designed to test various removal methods on test samples released earlier (Aglietti et al., 2020). One of the methods was a net (Aglietti et al., 2020), which proved to be effective for the task at hand (Carceller, 2021).

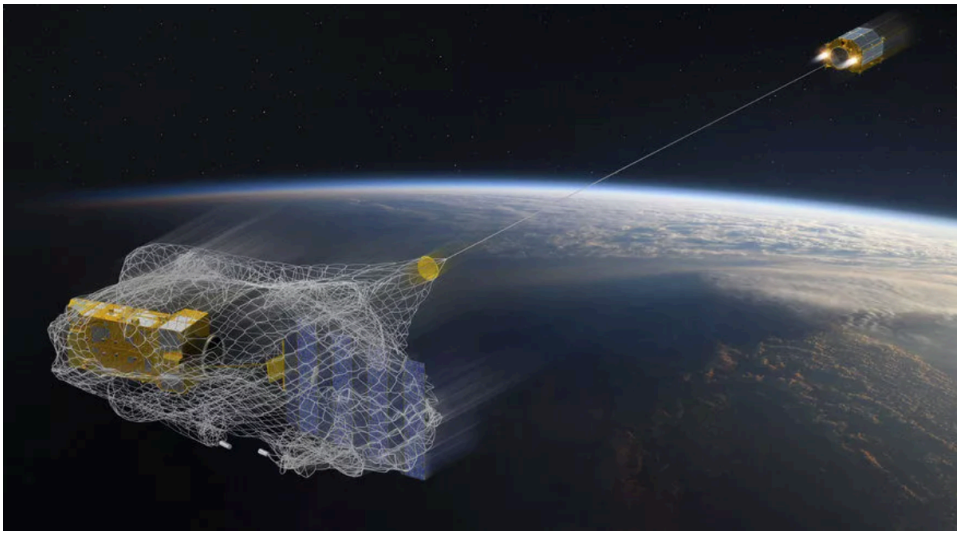

Figure 4.10: Artist illustration of a net capturing space debris (Werner, 2018).

The removal of said fragments might be possible if a net with a fine enough mesh were to be employed on a debris cloud of small debris.

4.3.4. Web Net

Another net option that has been considered is a web-type net with a cone shape connected to a spacecraft that captures debris in the manner of a cobweb in nature. This technique would be better suited for smaller debris with a small enough mesh size and high impact resistance (Carceller, 2021). Figure 4.11 shows a representation of the method.

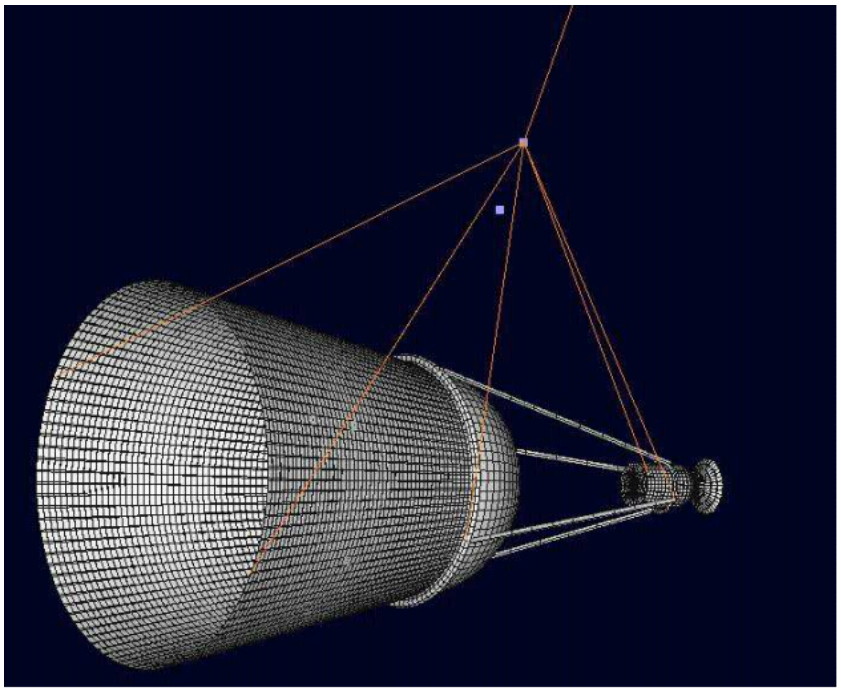

Figure 4.11: Net concept based on a spider web (Trivailo & Kojima, 2016).

This theory employs ”one-shot rip-stop type post-capture energy absorbers and a very small and light storage spool (attached to the center of the net to prevent loose debris generation).” (Trivailo & Kojima, 2016). Using this concept, the net concept might be a viable option for the current study (Carceller, 2021).

4.3.5. Foam Panel

Another technique not existing in the literature is a foam panel that catches the debris upon impact. This concept arose from a hypervelocity impact test conducted NASA Orbital Debris Program Office (ODPO), Space Force Space Systems Command (SSC), the Aerospace Corporation, the University of Florida, and Air Force Arnold Engineering Development Complex (AEDC) for the DebriSat Project. In this experiment, a model of a satellite was subjected to a hypervelocity impact test in a chamber lined with foam panels of varying densities (NASA, 2021). The debris fragments generated by the impact were captured by such foam panels, which were then studied by students such as myself at the University of Florida to establish a revised satellite break-up model.
Depending on the type of foam utilized, this technique might succeed given that the diverse foam densities could offset each others downsides. For example, low density foam may have more trouble catching larger debris while high density foam is better at catching larger debris. Nonetheless, impact with high density foam may lead do some fragmentation of the debris but low density foam could catch these fragmented particles.(NASA, 2021).

4.3.6. Aerogel Cushion

Another alternative would be to employ an aerogel cushion, which would be capable of capturing small debris. Notwithstanding, to prevent stress and breakage in the material after a specific period of time, this aerogel would most likely need to be adapted from the traditional aerogel. A series of tests conducted revealed that this process could be an effective method of ADR (Woignier et al., 2013).

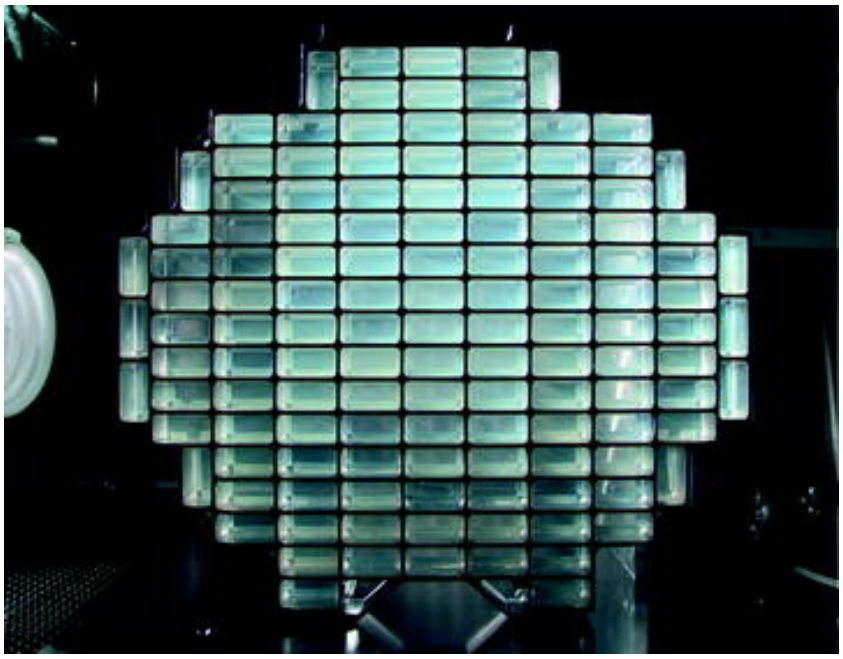

Figure 4.12: Aerogel used for space application (Jones & Sakamoto, 2011).

Aerogel has been used in space applications for at least two decades. NASA has used aerogel in missions such as the Mars Pathfinder, Exploration Rover, and Science Lander to collect hypervelocity fragments such as stardust in addition to providing thermal insulation. Although insulation is not the primary goal of our mission, it is always a plus: the utilization of an aerogel cushion or device might serve both as a collector and an insulator. Furthermore, because of its low density and insulating properties, aerogel has the added benefit of not heating to the extent that it alters the material characteristics of the specimen being captured (Dunbar, 2008).
Even so, aerogel has some limitations with respect to particle size; stardust is typically smaller than a grain of sand and, once captured, can generate a ”carrot-shaped track” 200 times its own length. This would not be a concern for millimeter-sized debris particles; nevertheless, for bigger debris fragments in the centimeter spectrum, a 10 cm debris particle would demand implausible quantities of aerogel (Dunbar, 2008). Notwithstanding, a combination of techniques could be employed with one filtering

larger debris while the other capturing smaller particles.

4.4. Challenges of ADR

ADR faces many challenges, which is why a real mission has never been flown. The main challenge, especially when considering small space debris, is that there is no communication with the debris. Looking at a general clean-up case, the challenges are related to the lack of data for small debris and the spread of the debris across the globe. Similarly, given that this study also looks at mitigating a break-up event, little to no information is available about the fragments in question, namely: size, orbital elements, mass, etc. When designing a device to mitigate such a case, this can pose a problem. In both cases, the general clean-up case and break-up case, actively tracking the debris is simply unfeasible. This is why a passive ADR method was chosen. The ability to have a spacecraft catch debris fragments without the need to adjust for the location of each individual fragment, would be highly beneficial for both scenarios mentioned. It would allow the catcher to be almost autonomous in the sense that as long as the mechanical design fits the required criteria, it would only have to be moved if it were to pose a threat to existing spacecraft. A catcher such as the one mentioned would merely rely on the initial ground data available.

4.5. Concluding Choice

After carefully analyzing all options and looking at the challenges faced by the cases at hand, it was found that many techniques require rendezvous situations. Given that this technique would have to be efficient for a general case and a breakup event, tracking would be difficult given the size of the objects and closeness in time to the explosion, so a rendezvous situation would be nearly impossible. Moreover, the large magnitude of relative speeds combined with the small size of the fragments results in methods such as the ones mentioned to be inefficient and unfeasible. Furthermore, the Δv that would be required to maneuver into the diverse orbits of all the small fragments would be too large. As a result, an option that does not necessitate maneuvering was chosen. The best option was determined to be a type of foam/aerogel that slows or stops the particles, followed by a possible second layer of foam to stop debris with higher velocities or larger mass. A collector shield would also be present to direct particles to the final debris container. Figure 4.13 shows an illustration of this. Once in orbit, this method would allow for passive flight, eliminating the need for large amounts of Δv.

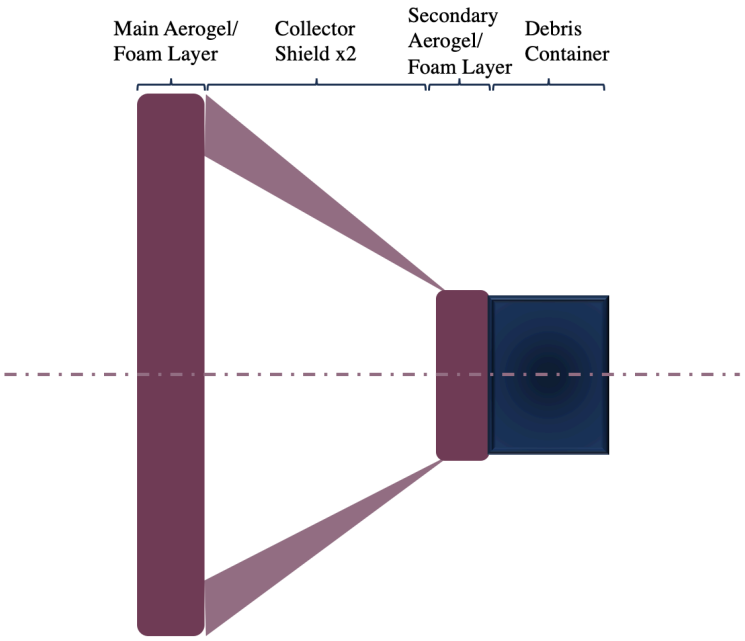

Figure 4.13: Final choice of the Removal Method.

4.6. Final Note

Given the concluding choice, the orbital aspects of said choice will be analyzed. The factors looked at will include: the size of the catcher, the number of debris captured in both cases mentioned, the best case in which to use this device, the most favorable orbit and the momentum values encountered for the best case. If the results of this study were to prove promising, a further study into the mechanical design would have to be carried out. The latter is considered beyond the scope of the current investigation however.

5

Astrodynamics

This chapter will examine the astrodynamics of both the debris fragments and the debris-collecting spacecraft. In order to do this, a range of reference frames will be presented to find the preferred option for the application at hand. Next, the possible coordinate systems used to define an orbit will be expressed. This will be followed by the governing equations of motion of an object. Then, an overview of the transformations used will be given along with the required equations for an orbit simulation. Similarly, the relative geometry of the debris and the spacecraft when in orbit, will be looked at along with the dynamics.

5.1. Reference Frame

This section will look at a number of reference frames which can be used for the problem at hand. This will aid in providing an accurate reference for the motion of the spacecraft and the debris fragments.

5.1.1. Earth-Centered Inertial

The Earth-Centered Inertial (ECI) reference frame is comprised of an Earth-centered coordinate system. As seen in Figure 5.1, in this reference frame, the reference plane is the equatorial plane of the Earth which coincides with the celestial equator. The axes are as follows (Rao, 2021):

- I_x from Earth to Sun on the spring equinox
- I_y cross product of I_x and I_z
- I_z center of Earth to the North Pole

The depiction of the axes can be seen in Figure 5.1.

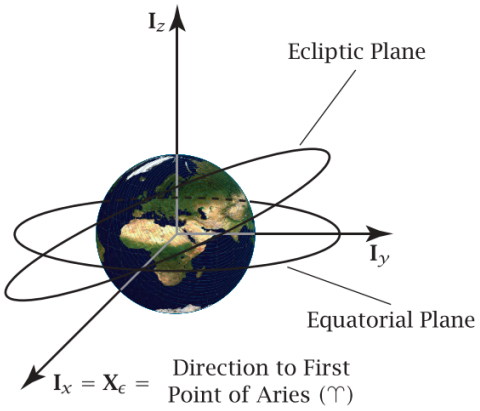

Figure 5.1: Depiction of ECI reference frame (Rao, 2021).

It is important to note that the ECI reference frame is not inertially fixed given that the center of the Earth is not inertially fixed. Nevertheless, it is assumed that the center of the Earth does not move significantly, it is not accelerated and it is fixed to the stars. Therefore, it can be considered pseudo-inertial. This reference frame is often used to describe the position of spacecraft or celestial objects (Rao, 2021).

5.1.2. Local Vertical Local Horizontal

The Local Vertial Local Horizontal (LVLH) reference frame has the local axes of the coordinate system at the center of mass of the spacecraft. This allows for the location of the debris with respect to the spacecraft to be successfully identified. The coordinates in this reference frame are defined by Cartesian coordinates, as seen in Figure 5.2. This frame is defined as follows (Reinthal, 2017):

- $\vec{e_x}$ directed radially outwards as seen from the center of the Earth
- $\vec{e_z}$ is directed normal to the orbital plane in the direction positive of the chief's orbit's angular momentum
- $\vec{e_y}$ is the remaining direction given by the cross product of $\vec{e_z}$ and $\vec{e_x}$

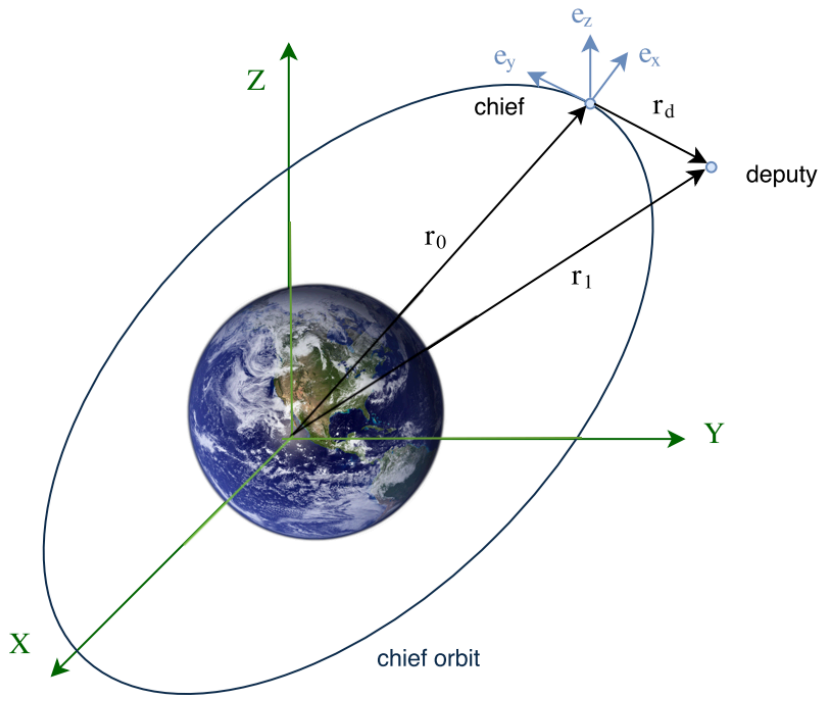

Figure 5.2: Cartesian inertial and local coordinate frames. ECI is depicted in green and LVLH of the chief in blue. For the study at hand the chief would be the spacecraft and the deputy would be the debris object(s) (Reinthal, 2017).

Given that for the case at hand we deal with a chief and a deputy, the LVLH frame will be used to obtain the relative position of the debris with respect to the spacecraft. The advantage of LVLH is that the relative behavior can be better understood and thus modeled.

5.2. Coordinate System

This section will look at a selection of coordinate systems as a means to obtain the most suitable option for the study at hand. These different coordinate systems will aid in pinpointing the location of both the spacecraft and the debris fragments. The elements implemented to obtain the diverse positions will be dependent on the chosen coordinate systems.

5.2.1. Cartesian

One of the most recurring coordinate systems in literature is the Cartesian coordinate system. Cartesian coordinates serve as a means to express the state of an object by defining the *x*, *y*, and *z* coordinates as well as the respective derivatives. This coordinate system is based on orthogonal axes with its center at a given point. An example of such a system is the aforementioned ECI frame and system where the center was placed at the center of the Earth. This system can be seen in Figure 5.3.

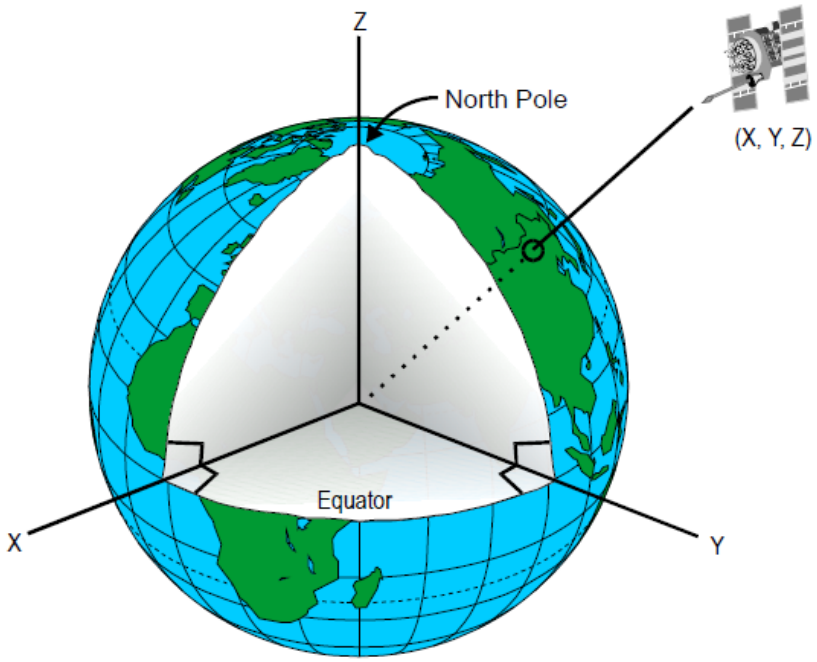

Figure 5.3: Depiction of a cartesian coordinate system in an ECI frame with the satellite's position found at coordinates x,y,z (Wong, 2015).

While this coordinate system has proved useful for a large variety of applications, the location of the debris fragments and the user satellite in space as seen from Earth changes considerably over each individual revolution which might introduce drawbacks (Carceller, 2021). An alternative to this type of coordinate system will be described in the next section.

5.2.2. Kepler

Another predominantly used coordinate system is the set of Kepler coordinates. This system consists of six orbital elements "used to parameterize the location of a spacecraft in orbit relative to a planet" (Rao, 2021). The six main orbital elements are the following (Rao, 2021):

- a defined as the semi-major axis which provides the size of the orbit
- e defined as the eccentricity which provides the shape of the orbit
- Ω defined as the right ascension of the ascending node which provides the angle between the main direction I_x (see Figure 5.1) and the line of nodes n going from the origin to the ascending node which is given by $n = I_z \times h$.
- i as the inclination of the orbit
- ω defined as the argument of periapsis which provides the angle from the line of nodes n to the eccentricity vector
- θ which in Figure 5.4 is referred to as ν is defined as the true anomaly which provides the angle from the eccentricity vector to the position of the spacecraft relative to the planet

A depiction of these orbital elements can be seen in Figure 5.4:

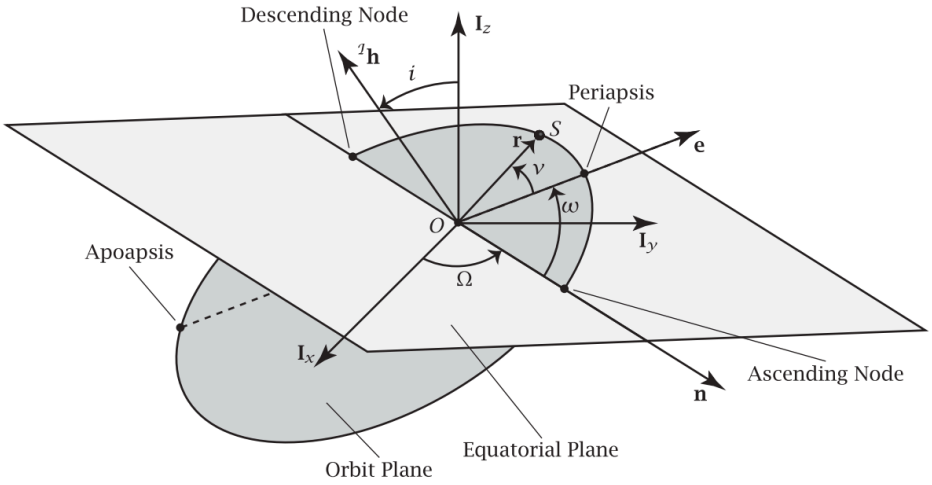

Figure 5.4: Orbital elements (Ω, i, ω, ν (referred to as θ in this paper) that define the orientation of the orbit and the direction towards the spacecraft, relative to the Earth-Centered inertial (ECI) coordinate system (Rao, 2021).

While the elements presented are considered to be the main six elements, there remain two further related elements that are commonly used in applications with orbital elements, these are as follows:

- E is defined as the eccentric anomaly, the exact definition of this can be seen in Figure 5.5
- M is defined as the mean anomaly which is an angle that varies with time defined by the product of the mean angular motion of the body and the time elapsed since the last pericenter passage (Wakker, 2015)

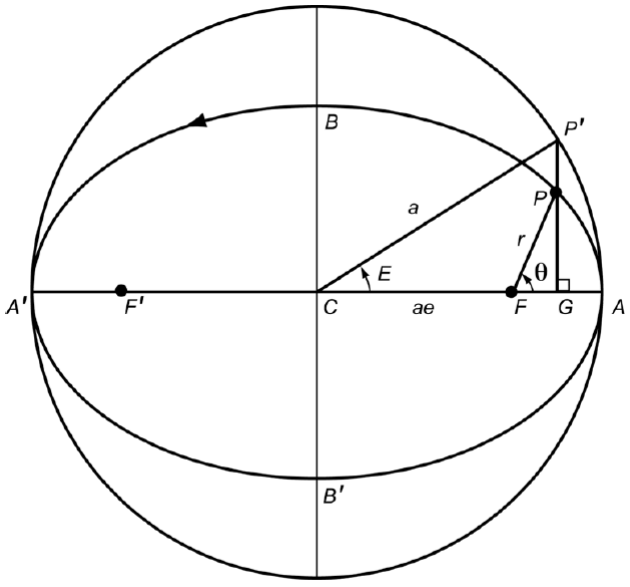

Figure 5.5: Diagram of in-plane orbital parameters (Wakker, 2015).

5.2.3. Other

Other coordinate systems that could be used include but are not limited to spherical, cylindrical, polar and modified equinoctial; however, these will not be further explored at this moment. The reason for

this is that for the problem at hand, the described coordinate systems are deemed the best for the application in question.

5.3. Governing Equations

In this section, the governing equations of motion will be looked at. These are crucial in order to be able to examine the behavior of the spacecraft and the debris. These equations will be formulated in an inertially fixed reference frame such as the one shown in the previous illustrations. The following notation will be useful in determining the differential equation of motion of the spacecraft relative to the planet (Equation 5.1). Let $\vec{r}$ represent the vector to the spacecraft as measured from the center of mass of the planet in question, in this case the Earth, and let $r = |\vec{r}|$ represent the magnitude of $\vec{r}$ (Rao, 2021).

$$\ddot{\vec{r}} = -\frac{\mu}{r^3}\vec{r} + \vec{a_p} \tag{5.1}$$

where

- $\vec{r}$ is the radial distance from the center of mass of the central body, such as the Earth, to the object of interest, such as the satellite, as seen in Figures 5.2 and 5.3.
- $\vec{a_p}$ is the acceleration due to perturbations
- μ is the gravitational parameter of the central body, equal to GM

For this part of the study, the perturbations will not be taken into account. A general magnitude for the perturbations at hand at an altitude of 750 km ranges from 10^{-10} km/s^2 for the solar radiation pressure to 10^{-5} km/s^2 for the J_2 term (Montenbruck & Gill, 2012). The gravitational acceleration is the largest at 10^{-2} km/s^2 (Montenbruck & Gill, 2012). However a deeper insight into perturbations will be provided in a later section in the chapter. This assumption leads to the following equation for the two-body problem described in Equation 5.2

$$\ddot{\vec{r}} = -\frac{\mu}{r^3}\vec{r} \tag{5.2}$$

Solving the two-body problem, the following solution is obtained.

$$r = \frac{h^2/\mu}{1 + e\cos\theta} \tag{5.3}$$

where

- h is the magnitude of the specific angular momentum (see Figure 5.6)
- θ is the true anomaly, in literature this is also referred to as ν as seen in Figure 5.6. For the remainder of this study θ will be used
- e is the norm of the eccentricity vector, pointing to the pericenter (the point in the orbit where the distance to the central body is minimal)

Using the following relationship a different version of the above equations can be derived as seen below:

$$p = \frac{h^2}{\mu} \tag{5.4}$$

$$r = \frac{p}{1 + e\cos\theta} \tag{5.5}$$

where

- p is the semi-latus rectum

This equation can be expressed in terms of the semi-major axis a using the expression below.

$$p = a(1 - e^2) \tag{5.6}$$

Resulting in the following expression for the solution of the two-body problem

$$r = \frac{a(1-e^2)}{1+e\cos\theta} \tag{5.7}$$

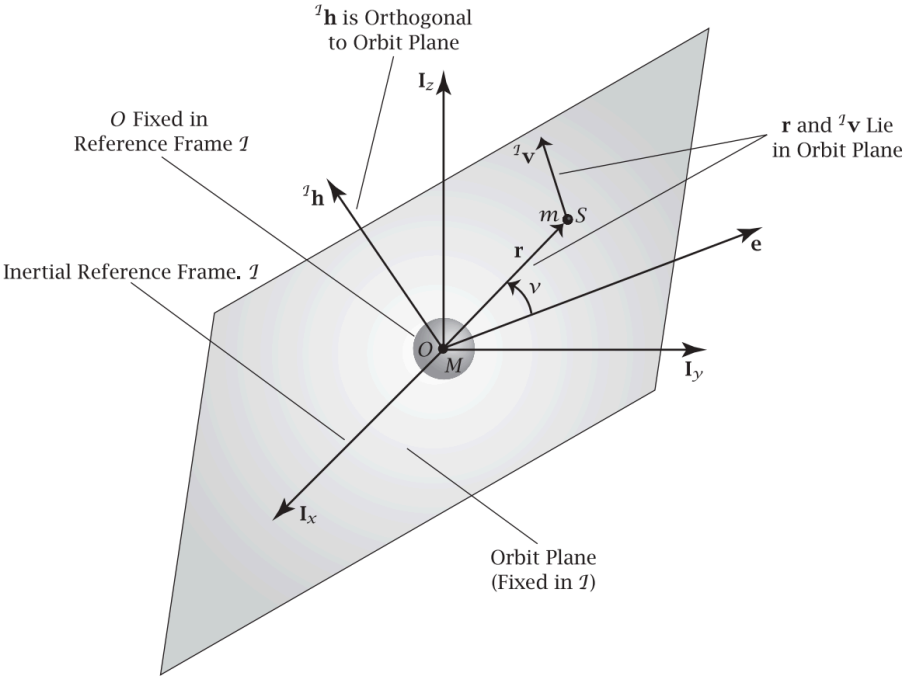

Figure 5.6: Depiction of the plane in which the solution of the two-body problem lies as well as the respective vectors. (Rao, 2021) Note ν depicted is referred to as θ throughout the study.

In order to find the velocity, the specific mechanical energy is used to obtain the expression seen in Equation 5.8.

$$E = \frac{v^2}{2} - \frac{\mu}{r} = -\frac{\mu}{2a} \tag{5.8}$$

solving for the velocity the equation known as the vis-viva equation is found as seen in Equation 5.9.

$$v^2 = \mu\left(\frac{2}{r} - \frac{1}{a}\right) \tag{5.9}$$

for the case of a circular orbit where $r = a$, such as the case of the majority of debris orbiting the Earth, the expression is simplified to the square of the circular velocity given as

$$v_c^2 = \frac{\mu}{r} \tag{5.10}$$

5.4. Transformations

As aforementioned, objects in orbit around the Earth can be defined in both Cartesian and Keplerian elements. It was concluded that in order to define the position of the spacecraft, Keplerian elements are preferred. However, in order to be able to find the location of the debris with respect to the spacecraft, Cartesian coordinates are a better option as we are operating in the LVLH frame. For this reason, a transformation between Cartesian and Keplerian elements and vice versa is necessary. A thorough description of these transformations can be seen in Appendix A.

5.5. Kepler Solver

In order to obtain a relationship between the position in the orbit and time, one must look at Kepler's Equation 5.11

$$E - e\sin E = \sqrt{\frac{\mu}{a^3}}(t - t_p) \tag{5.11}$$

where t_p represents the time of pericenter passage where the true anomaly is equal to $0°$ (Wakker, 2015). Given an initial value for the eccentric anomaly E_0 at an initial time t_0, Equation 5.11 can be rewritten as seen in Equation 5.12

$$t_p = t_0 - \left(\sqrt{\frac{\mu}{a^3}}(E_0 - e\sin E_0)\right) \tag{5.12}$$

A depiction of this can be found in Figure 5.7 (Rao, 2021).
The next step is to find out the number of periapsis crossings. This will be done by calculating the time since the periapsis crossing as shown in Equation 5.13 (Rao, 2021). The proceeding course of action is calculating the period of the orbit *T* with Equation 5.14 (Wakker, 2015). This was done as a means to determine the number of times that the spacecraft had crossed the periapsis *k* as seen in Equation 5.15 (Rao, 2021). In order to get a clearer picture of this, one can look at Figure 5.7 (Rao, 2021).

$$\Delta t = t - t_p \tag{5.13}$$

$$T = 2\pi\sqrt{\frac{a^3}{\mu}} \tag{5.14}$$

$$k = floor(\frac{\Delta t}{T}) \tag{5.15}$$

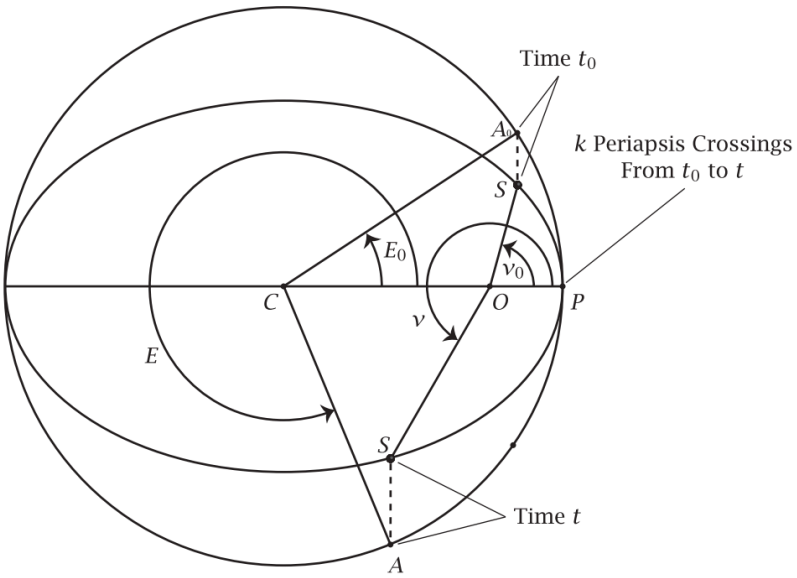

Figure 5.7: Schematic showing two general points on an orbit where the spacecraft is located at point A_0 at time t_0 with a true anomaly and eccentric anomaly ν_0 (θ_0 in this paper) and E_0, respectively, and is located at point A at time t with a true anomaly and eccentric anomaly ν (referred to as θ in this study) and E, respectively. The spacecraft crosses periapsis a total of k times en route from point A_0 to point A (Rao, 2021).

Once the number of periapsis crossings is obtained, the time recurred since the last periapsis crossing is obtained as shown in Equation 5.16. This calculation is carried out aiming to obtain an initial guess for the eccentric anomaly E_{guess} as seen in Equation 5.17.

$$\Delta t_{lastrev} = \Delta t - Tk \tag{5.16}$$

$$E_{guess} = 2\pi \frac{\Delta t_{lastrev}}{T} \tag{5.17}$$

After the initial guess is obtained, an iterative process is carried out as a means to obtain the value of the eccentric anomaly. In order to do this the Newton-Raphson method is used (Wakker, 2015). In the first iteration E_k will be equal to E_{guess}(Rao, 2021).

$$E_{k+1} = E_k - \frac{\mathcal{F}(E_k)}{\frac{d}{dE}\{\mathcal{F}(E)\}\Big|_{E=E_k}} = E_k - \frac{E_k - e\sin E_k - (E_0 - e\sin E_0)}{1 - e\cos E_k} \tag{5.18}$$

The iterative process is carried out until the difference in the iteration reaches a desired value. Nonetheless, literature also presents other methods to choose the number of iterations N, this can be defined as a function of eccentricity as seen in Equation 5.19 (Rao, 2021).

$$N = 10\left[\frac{1}{1-e}\right] \tag{5.19}$$

Once a value for the eccentric anomaly is obtained Equation 5.20 is rewritten to obtain the value for the true anomaly at time t.

$$\tan\frac{\theta}{2} = \sqrt{\frac{1+e}{1-e}}\tan\frac{E}{2} \tag{5.20}$$

5.6. Dynamics

For a satellite in LEO orbiting the Earth below 800 km altitude, the main accelerations acting on it are gravity, atmospheric drag, the J_2 zonal harmonic and solar radiation pressure (Girardin et al., 2018). Typical magnitudes for these accelerations are presented in Figure 5.8.

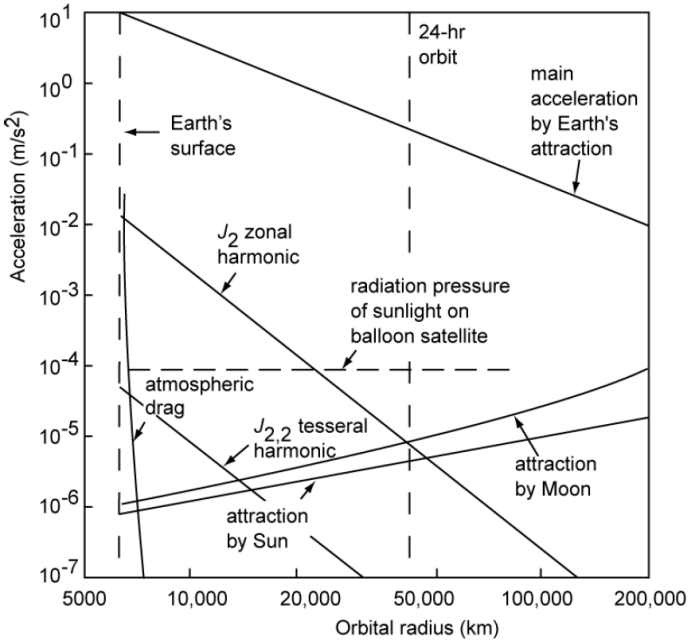

Figure 5.8: Magnitude of accelerations acting on a satellite, based on altitude (Wakker, 2015).

When looking at the acceleration with the largest effect, it can be observed that this corresponds to the acceleration produced by Earth's central attraction. This type of acceleration is independent of the mass of the satellite in question (Wakker, 2015). The acceleration provided by the Earth's gravitational force is defined as seen in Equation 5.21 (Wakker, 2015).

$$\vec{f} = \vec{\nabla}(U) \tag{5.21}$$

The gravitational potential U can be described as a function of the spherical harmonics of the gravity field shown in Equation 5.22.:

$$U = \frac{\mu}{r}\sum_{\ell=0}^{\infty}\left(\frac{a_e}{r}\right)^{\ell}\sum_{m=0}^{\ell}P_{\ell,m}(\sin\phi)\left[C_{\ell,m}\cos m\lambda + S_{\ell,m}\sin m\lambda\right] \tag{5.22}$$

where

- a_e is the semi-major axis of the Earth's reference ellipsoid
- r is the satellite distance in a body-fixed coordinate system
- ϕ is the latitude in a body-fixed coordinate system
- λ is the longitude in a body-fixed coordinate system
- C_{lm} and S_{lm} are spherical harmonic coefficients of degree l and order m
- P_{lm} and S_{lm} are the associated Legendre functions of degree l and order m

The different degrees and orders can be attributed to different elements in the gravity models. When considering the model with degree 0 and order 0 the remaining function is $U = \frac{\mu}{r}$. In this scenario, the body is treated as a point mass (Wakker, 2015). Another commonly used term is that of degree 2 and order 0, this accounts for the oblateness of the Earth. A typical representation of $-C_{l,0}$ can be defined as J_l which in the case mentioned would be J_2. The J_2 is defined as a zonal harmonic coefficient. The perturbation caused by the oblateness is often referred to as the J_2 perturbation (Wakker, 2015) and in this case, is also one of the main accelerations for the case at hand. Other harmonics include the $J_{2,2}$ harmonic depicted in Figure 5.8.

When looking at the acceleration produced by atmospheric drag, the equation is seen in Equation 5.23 (Hall, 2021).

$$\vec{f} = -\frac{1}{2}\rho C_D\frac{A}{m}|\vec{v}|\vec{v} \tag{5.23}$$

where

- $\vec{v}$ is the velocity w.r.t. the ambient atmosphere
- C_D is the coefficient of drag
- A is the reference area
- ρ is the density of the air at the given altitude
- m is the mass of the vehicle

From Equation 5.23, it can be seen that when catching the debris, the increase in mass will not have an effect on the atmospheric drag. This can be associated with the following relationship $m_{new} = m_{old} + m_{added}$. Given that the study concerns itself with small fragments, the added mass would not have a significant impact to affect the accelerations acting on the spacecraft which are mass dependent.

Looking at the next dominating perturbation (Figure 5.8) acting on the spacecraft, solar radiation pressure, the governing equation is as follows (Wakker, 2015).

$$\vec{f} = -C_r\frac{WA}{mc}\vec{e}_s \tag{5.24}$$

where

- C_r is the radiation pressure coefficient which defines the satellite's reflectivity
- W is the power density of the solar radiation near the Earth taken to be 1360 W/m^2

- A is the effective cross-sectional area of the satellite
- m is the mass of the satellite
- c is the speed of light in a vacuum
- $\vec{e_s}$ is a unit vector from the satellite to the Sun

From Equation 5.24, it can also be seen that an increase in mass will not affect the solar radiation pressure given the relationship $m_{new} = m_{old} + m_{added}$.
In order to obtain an approximation of the effect of the perturbations on the spacecraft and the debris, the equation provided for each acceleration by Wakker, 2015 are used. Given the magnitude of the accelerations and the time the spacecraft would spend in orbit i.e. one week, it can be seen that the effect of the perturbations is very important.
Wakker, 2015 provides references for the effect of these perturbations on orbital elements using an example for a satellite at 500 km with an inclination of $45°$. For the perturbation caused by the J_2 term, the largest effect would be on the right ascension of the ascending node. For a duration of a week in orbit, this effect would result in $38.64°$. Nonetheless, Wakker, 2015 shows that for higher inclinations such as the one used in this study, this value would be lower by a factor of 10.
The effect of drag on the semi-major axis for the duration of a week would result in 733.80 km. Similarly, when looking at solar radiation pressure, using the maximum change in the right ascension of the ascending node per revolution (Wakker, 2015), a maximum value of $6.34°$ is obtained.

Given this result it is evident that the effect of the perturbations at such low altitudes is not negligible. While the use of perturbations was considered it was deemed computationally expensive. Given that the study focuses on the relative behavior of a spacecraft and the debris fragments, it can be assumed that the perturbations will affect both the spacecraft and the debris in a similar manner. This can be due to the fact that they will be travelling on about very similar orbits. For this reason, the perturbations will not be taken into account when simulating the orbits. However, their effect will be kept in mind when analyzing the results.

5.7. Orbit Changes and Delta V

Although the passive ADR method prizes itself on not having to carry out any maneuvers, over time a loss of velocity would occur attributed to the recurring impacts of the debris fragments. This would imply, that with the passage of time, maneuvers would have to be carried out as a means to re-orbit the spacecraft in its desired orientation. Moreover, if the ADR technique demonstrates the ability to remove debris successfully in the chosen orbit, it could possibly be re-positioned to another orbit where a fragmentation event had occurred or was expected to occur. Comparably, were the spacecraft to find itself in a collision course with another spacecraft, a maneuver would have to be carried out to avoid a collision. So as to achieve this, the availability of enough Δv would be needed to have the ability to accomplish the required maneuver. The Δv required by such a maneuver can be described by the following equation (Wakker, 2015).

$$\Delta V^2 = V_1^2 + V_2^2 - 2V_1V_2 \cos \Delta i \tag{5.25}$$

Should the necessity to perform a maneuver arise, typical Δv values at 750 km altitude are 130 m/s per degree for a plane change and 0.52 m/s per km for an altitude change at an inclination of $98°$ (Wertz, 2009). However, the Δv and altitude changes are out of the scope of this study and will therefore not be considered further.

5.8. Spacecraft Orientation

With the purpose of increasing the catchment area, the orientation of the spacecraft will be considered. It was adjudged that the spacecraft orientation with the best outcome would be perpendicular to the movement. In an effort to obtain a clearer picture, Figure 5.9 shows the case of the perpendicular movement of the spacecraft and the orientation at an angle. It is readily apparent that when flying with the perpendicular orientation the expected number of space debris fragments caught is larger. This observation strengthens the initial hypothesis.

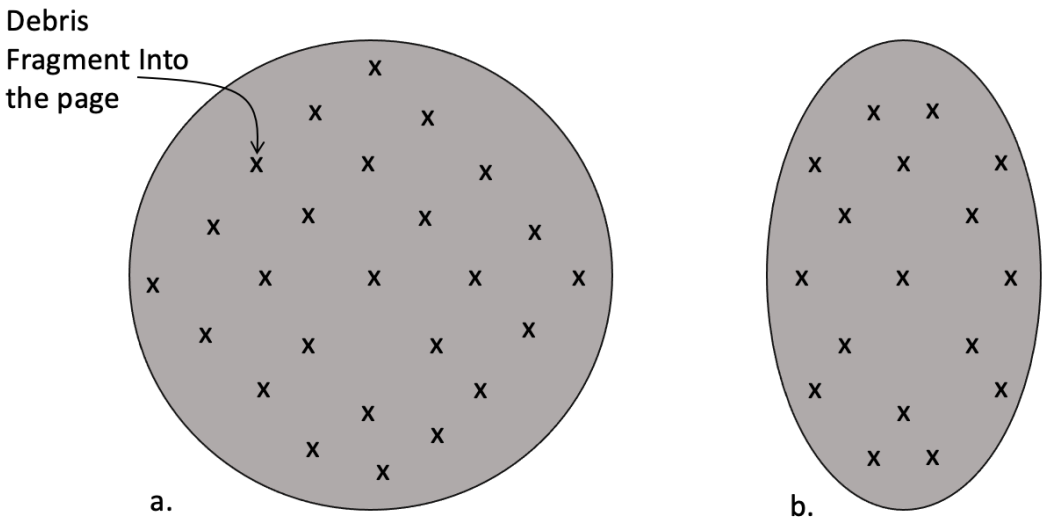

Figure 5.9: a. Depiction of spacecraft orientation perpendicular to debris object flying towards the spacecraft. b. Depiction of angled orientation (front view).

5.9. Potential Debris Capture

In order to gain a clearer picture of the initial feasibility of the passive capture device, it was looked at as both a general mitigation device as well as an emergency mitigation device in the case of a fragmentation event. The possible number of objects captured was obtained with a set of calculations. In terms of a very first idea on general clean-up, the number of particles and orbit location of the clean-up was determined using Figure 5.10. Here an inclination and altitude with a high density of debris were chosen and then the volume of a sphere and a circular orbit was used to estimate the number of debris particles that could be captured per year (Carceller, 2021).

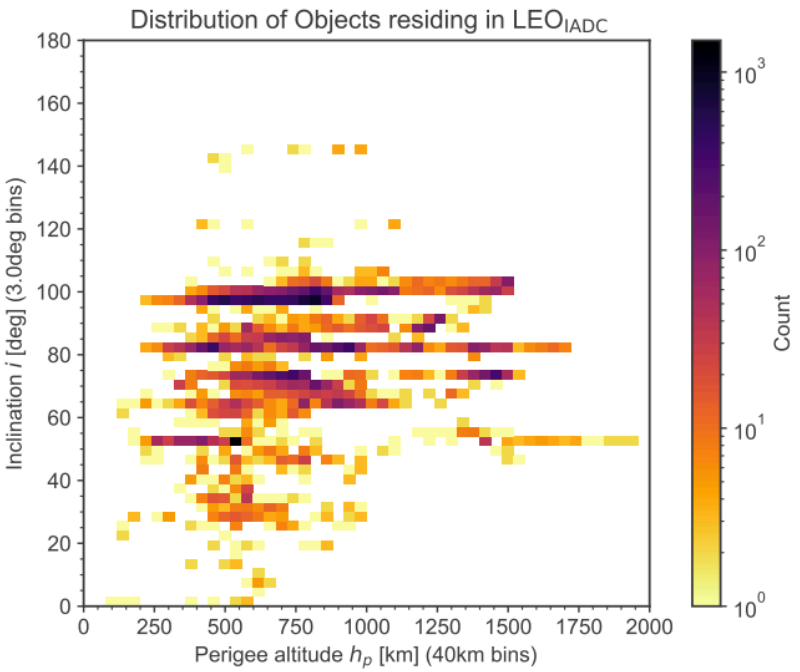

Figure 5.10: Distribution of objects residing in Low Earth Orbit (Lemmens and Letizia, 2022).

From Figure 5.10, a bin between 730 and 770 km altitude was taken for all altitudes. The following

equation was used to get the volume of a sphere with 730 km as the inner radius and 770 km as the outer radius.

$$V = \frac{4}{3}\pi((R_{outer} + R_E)^3 - (R_{inner} + R_E)^3) \tag{5.26}$$

This would result in a volume of 2.554×10^{10} km^3.

Then the number of particles was obtained from the graph as approximately 3,000 particles for the chosen altitude bin. Accounting for the non-tracked debris particles between 1 cm and 10 cm as 30 times more than the tracked particles of the given number (Lemmens & Letizia, 2022) resulting in 90×10^3 particles. Using the number of particles and the volume, the density of the particles in the volume was obtained as follows using Equation 5.27.

$$Density = \frac{\#Particle_{debris}}{V} \tag{5.27}$$

A density of 3.524×10^{-6} particles per km^3. In order to obtain a proper estimate, the catchment area of the spacecraft was calculated with Equation 5.28.

$$A = \pi r^2 \tag{5.28}$$

where the radius *r* was taken as 20 m. This resulted in an area of 1.257×10^{-3} km^2. The particle capture number was obtained as follows, using Equation 5.29.

$$\#Particles_{captured} = A \times v_{rel} \times Density \times t \tag{5.29}$$

Using a relative velocity of 14 km/s (Wakker, 2015), it resulted in 6.200×10^{-8} particles caught per second. Using the particle number obtained per second the particle number per week was obtained to be 0.0375. Compared to the original number of particles this would mean that 4.166×10^{-5} % of the particles were caught.
Next, the number of particles for the aforementioned fragmentation of Kosmos 1408 was calculated. The number of particles was chosen based on a similar event, namely the Chinese anti-satellite missile test conducted in 2007. The Chinese test resulted in a generation of 100,000 debris fragments of size 5 cm and smaller (Kan, 2007).
In order to obtain preliminary numbers the volume considered was taken as a ring around the Earth with an estimate for the cross-sectional area of the cloud taken to be 20 km by 20 km at an altitude of 555 km (Kan, 2007). This resulted in the expression seen in Equation 5.30.

$$V = 2\pi(R_E + h)wl \tag{5.30}$$

where

- R_E is the Earth's Radius taken as 6,378 km
- h is the altitude taken as 555 km
- w is the width of the cross-section taken as 20 km
- l is the length of the cross-section taken as 20 km

This resulted in a volume of 1.7425×10^7 km^3.

Next, the density of the cloud was calculated by using the total number of particles and the density as seen in Equation 5.31.

$$Density = \frac{\#Particle_{debris}}{V} \tag{5.31}$$

The number of particles here was chosen for an altitude and inclination bin resulting in 30×10^3 particles. Using the aforementioned volume obtained and the number of particles a density of 1.7×10^{-3} particles per km^3 was obtained.

Given that the catcher vehicle would be the same, the same value for the area of 1.257×10^{-3} km^2 is used. Finally, the preliminary number for the particles captured in the case presented was calculated using Equation 5.32.

$$\#Particles_{captured} = A \times v_{rel} \times Density \times t \tag{5.32}$$

Using a relative velocity of 14 km/s (Wakker, 2015), it resulted in 3.029×10^{-5} particles caught per second. Using the particle number obtained per second the particle number per week was obtained to be 18.31 per week. This equates to 0.061% of the particles caught.

As can be seen, both the percentage of particles caught for the explosion case is more than 1000 times larger than that of the general explosion. Similarly the number of particles caught is almost 500 times larger. Moreover, given the fact that the explosion results in a high-density cloud, it can be expected that simulation results would lead to a higher number. For this reason, it was chosen to carry out the simulation for a break-up event in particular.

5.10. Concluding Remarks

All in all, upon concluding the astrodynamical analysis, it was found that although perturbations play a significant role in defining an accurate orbit including them would be too computationally expensive. Given that it is a feasibility study, it will focus on the interaction between the spacecraft and the debris looking at relative motion and mechanical interactions such as momentum. Considering that both the spacecraft and the debris are acted upon by perturbations, when considering relative motion they can be neglected to first order. For this reason, perturbations will not be considered however their importance is acknowledged were this concept to prove feasible (Carceller, 2021).

In terms of the best choice for reference frames and coordinate systems, it was concluded that the most optimal reference frames for this study are the ECI frame to describe the movement of the spacecraft and the LVLH frame for the position of the debris with respect to the spacecraft (Carceller, 2021). Comparably, regarding the coordinate systems, Keplerian elements will be used for the orbit simulations of the spacecraft and the debris and Cartesian coordinates will be used for the motion of the debris relative to the spacecraft. This will ensure an accurate representation of the relative motion of the spacecraft and the debris fragments.

6

Satellite Breakup

In order to be able to generate a dataset of debris fragments in line with a real-life satellite breakup, an existing breakup model will be used. Breakup models serve as a tool to model the behavior and characteristics of debris fragments after an explosion or collision. The thesis at hand will make use of the state of the Russian satellite Kosmos 1408 at time of explosion in November 2021. For this reason, a breakup model will be used to generate the required data for the simulation the thesis will deal with. This chapter will discuss the history of models, how models are created, and which model was chosen for the application at hand.

6.1. History

Since the space era first began, there have been more than 550 known fragmentation events (Lemmens & Letizia, 2022). Over time these events have been catalogued along with their respective debris clouds. This section will take a set of historical events and look at the resulting debris clouds (Johnson et al., 2001). In Anz-Meador et al., 2018's 15^{th} edition the debris population in 2018 was as shown in Figure 6.1. According to Anz-Meador et al., 2018 the diverse peaks can be attributed to different

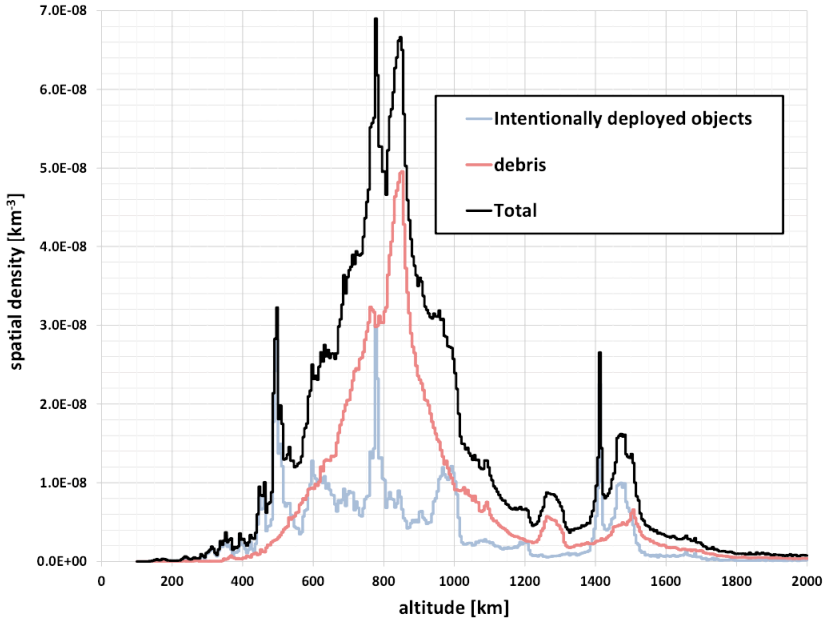

Figure 6.1: The near-Earth (up to 2000 km) altitude-dependent debris population (Anz-Meador et al., 2018).

events. For example, at an altitude of 890 km, the peak can be attributed to the anti-satellite missile

test conducted by China that destroyed the weather satellite Fengyun 1C. Similarly, the peak found at 770 km can be attributed to the Iridium-Cosmos collision which was presented in earlier chapters. Needless to say, these catastrophic events resulted in an important increase in space debris visible to this day.

Taking a closer look at the individual impact of the aforementioned spacecraft, it was clear to see that the breakup that generated the most trackable debris was the Fengyun 1C with 3,442 catalogued fragments and 2,832 still in orbit (Anz-Meador et al., 2018). Similarly, the Comos-Iridum collision lead to a generation of 1,668 catalogued fragments with 1,076 still in orbit originating from Cosmos 2251 and 628 catalogued fragments with 333 still in orbit belonging to Iridium 33 (Anz-Meador et al., 2018). The resulting debris clouds can be observed in Figures 6.2 to 6.4 (Anz-Meador et al., 2018).

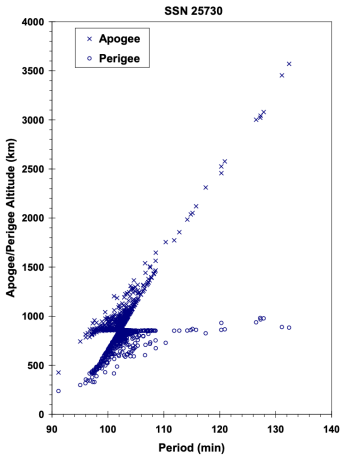

Figure 6.2: Fengyun 1C debris cloud remnant of 2000+ cataloged fragments 6 months after the event as reconstructed from the US SSN database (Anz-Meador et al., 2018).

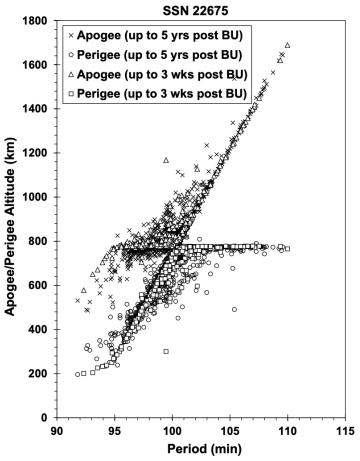

Figure 6.3: The COSMOS 2251 debris cloud, including 1648 fragments cataloged up to 5 years after the event (Anz-Meador et al., 2018).

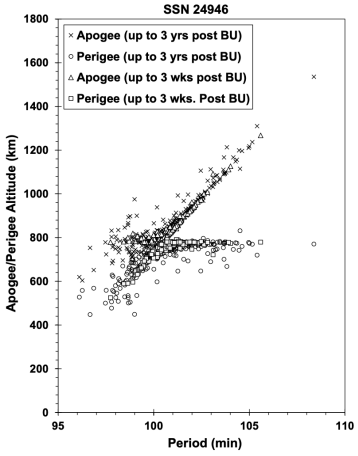

Figure 6.4: The IRIDIUM 33 debris cloud, including 621 fragments cataloged up to 3 years after the event (Anz-Meador et al., 2018).

However, although these are the most famous breakup events, there are others such as the Nimbus 4 R/B which generated 441 catalogued with 299 still in orbit, this occurred the 17^{th} of October 1970 due to unknown causes. NOAA 3 R/B 220 catalogued with 198 still on orbit and broke up due to propulsion the 28^{th} of December 1973. Another breakup that occurred the 25^{th} of November 2015 is the NOAA 16 for which the causes are unknown and generated 458 trackable of which 458 were defined as still in orbit (Anz-Meador et al., 2018).

6.2. Breakup Models

Satellite breakup models serve as a means to represent the end result of a breakup event such as an explosion or a collision. In order to successfully do this, the fragment size, area-to-mass ratio and the distribution of the Δv are collected as a means to generate distributions. These distributions can be obtained empirically (based on existing data) and theoretically. These models are critical in being able to predict the behavior of the debris if such an event is predicted and successfully identify the risks of the debris both short- and long-term. In literature, the model that is most used is the NASA Breakup Model 4.0. This model will be further explained later in the chapter.

Other models include the Aerospace Corporation's model IMPACT. This model is a semi-empirical model based on on-orbit and ground data (Mains & Sorge, 2022). The most recent update of the model, IMPACT 8.0, was updated with a more recent hypervelocity impact test conducted by Debrisat. This test aims at obtaining a breakup model reflecting the behavior of new materials used in satellites such as Carbon-fiber-reinforced polymers (CFRP). The difference between the previous model and the current model versus the data obtained from the Debrisat hypervelocity impact test can be seen in Figure 6.5 where the width-to-length ratio of copper was plotted for the previous model, current model and

the Debrisat explosion. It can be seen that the updated model follows the real life data much closer than the previous model. This shows the importance of finding an updated model for breakups in space. However, given that the Impact 8.0 model is very recent and more apt for more modern satellites, it will not be used. This can be attributed to the fact that the Kosmos 1408 was launched in 1982 so an older model would be more appropriate.

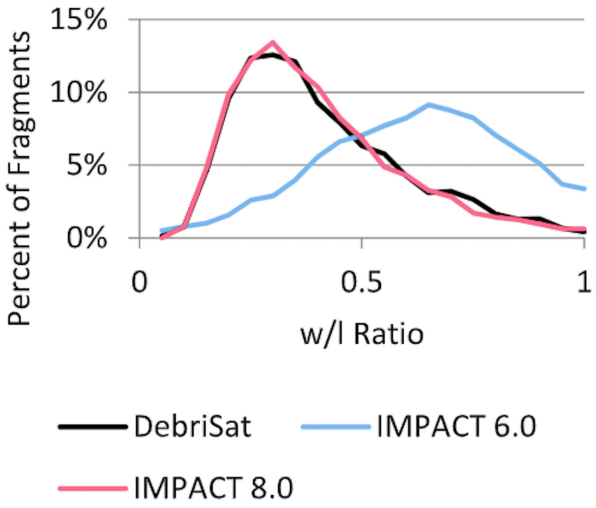

Figure 6.5: DebriSat,IMPACT 8.0 and IMPACT 6.0 copper fragment w/l ratio distribution (Mains & Sorge, 2022).

6.3. NASA Breakup Model 4.0

The main model used to describe the behavior of the debris fragments upon explosion in this study is the NASA Breakup model 4.0. This model serves to provide, density, size, Δv and area-to-mass ratio. The NASA breakup model can be divided into two sections: explosion and collision. For the case at hand, the explosion model was used. The explosion part of the model was created with a set of real-world data based on seven on-orbit explosions. An example of how the model was created can be seen in Figure 6.6 where the trend line was obtained from the set of data on these real-life cases.

6.3.1. Density

The model defines the particles as spherical in nature with a density of aluminum for objects smaller than 1 cm defined by ThyssenKrupp as 2,710 kg/m^3. For larger debris, diminishing density for larger debris, the density was defined as seen in Equation 6.1 (Johnson et al., 2001).

$$\rho = 92.937 d^{-0.74} \tag{6.1}$$

where

- d is the debris diameter in meters equivalent to L_c which will be mentioned later.

6.3.2. Size Distribution

The model provides a relationship between the cumulative number of debris as a function of debris size as seen in Equation 6.2 (Johnson et al., 2001).

$$N = 6 L_c^{-1.6} \tag{6.2}$$

where

- L_c is the characteristic length in meters.

In order to obtain a valid size distribution, the unique debris numbers for each debris size had to be found. This was done using the chosen sizes of 1 mm to 10 cm since the study concerns itself with

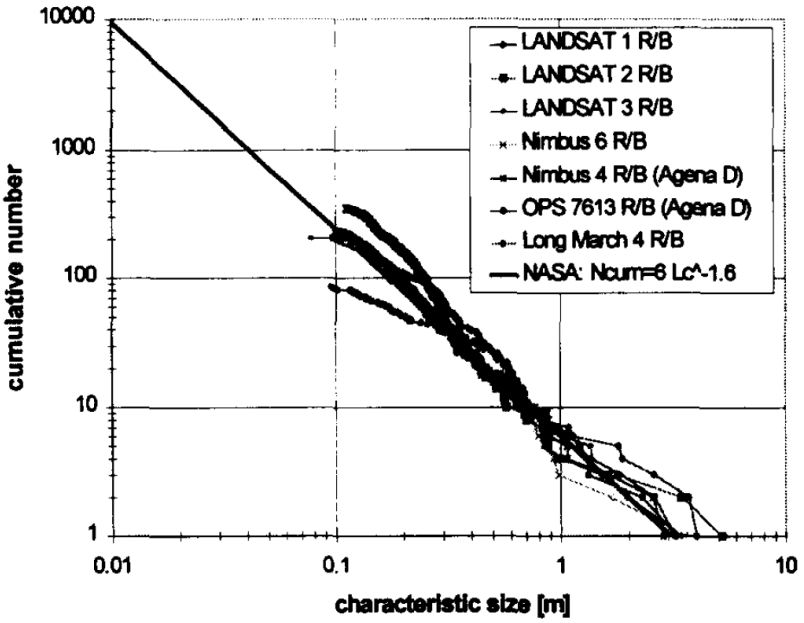

Figure 6.6: Sample debris size distributions from seven upper explosions, collisions and stage breakups, as derived from SSN data (Johnson et al., 2001).

small fragments. The results were obtained by subtracting the number of larger fragments from the number of smaller fragments in bins of 1 mm, an example can be seen in Equation 6.3.

$$N_{unique} = N_{1mm} - N_{2mm} \tag{6.3}$$

This modification can be seen and contrasted with the cumulative number of fragments in Figures 6.7 (based on Equation 6.2) and 6.8 (based on Equation 6.3) (Johnson et al., 2001). A verification and

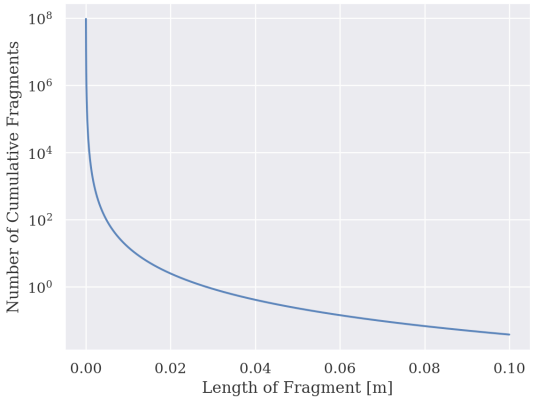

Figure 6.7: Cumulative number of debris as a function of fragment sizes in meters.

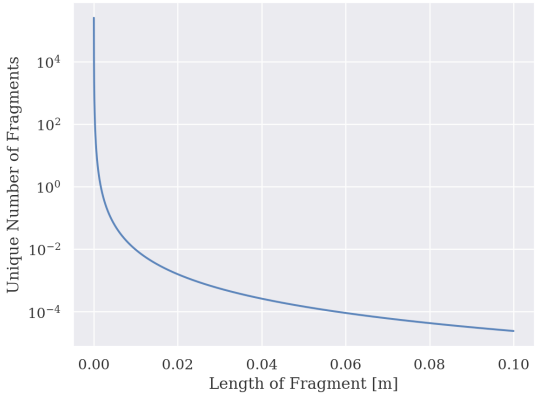

Figure 6.8: Unique number of fragments as a function of fragment sizes in meters.

validation of the obtained data versus the model can be osberved in Chapter 9. Once the unique number of fragments was obtained for the desired fragment sizes, a size probability curve was developed by dividing the unique numbers by the total number of fragments. The results can be observed in Figure 6.9. Using the probability distribution, a random generator was used to generate a population of 10,000 fragments with sizes based on the probability curve. This resulted in the distribution seen in Figure 6.10.

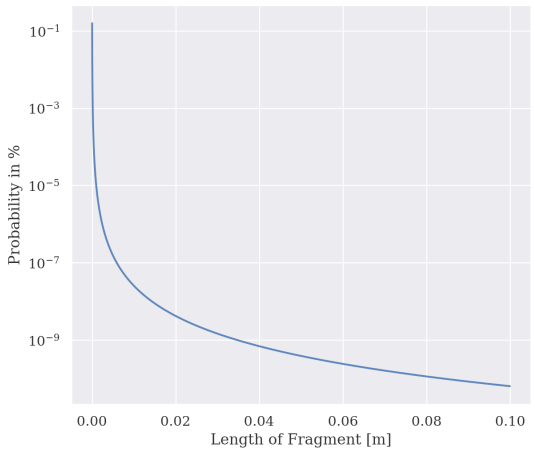

Figure 6.9: Probability of respective sizes of the debris fragments.

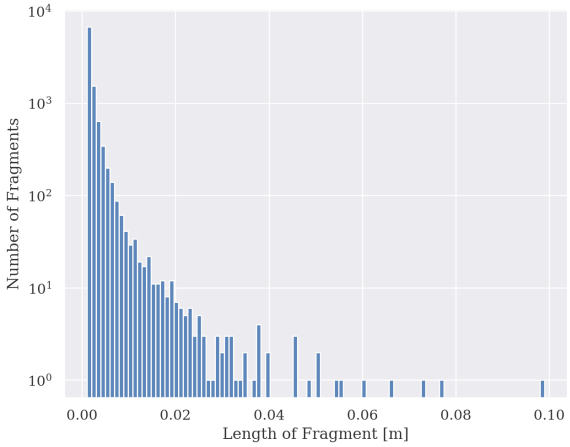

Figure 6.10: Distribution of the number of fragments as a function of size in meters, for total population of 10,000 fragments.

6.4. Area-to-Mass Distribution

For objects with L_c smaller than 8 cm, a single area-to-mass (A/M) distribution function was derived from a set of hypervelocity impact tests for both spacecraft and upper stages. The results of said hypervelocity impact tests were formulated into a set of equations seen in Equations 6.4 to 6.9 (Johnson et al., 2001).

$$D_{A/M}^{SOC}(\lambda_c, \chi) = N(\mu^{SOC}(\lambda_c), \sigma^{SOC}(\lambda_c), \chi) \tag{6.4}$$

$$\lambda_c = log_{10}(L_c) \tag{6.5}$$

$$\chi = log_{10}(A/M) \tag{6.6}$$

$$N(\mu, \sigma, \chi) = [1/\sigma(2\pi)^{0.5})]e^{-(\chi-\mu)^2/2\sigma^2} \tag{6.7}$$

$$\mu^{\text{soc}} = \begin{cases} -0.3 & \lambda_c \leq -1.75 \\ -0.3 - 1.4\,(\lambda_c + 1.75) & -1.75 < \lambda_c < -1.25 \\ -1.0 & \lambda_c \geq -1.25 \end{cases} \tag{6.8}$$

$$\sigma^{\text{soc}} = \begin{cases} 0.2 & \lambda_c \leq -3.5 \\ 0.2 + 0.1333(\lambda_c + 3.5) & \lambda_c > -3.5 \end{cases} \tag{6.9}$$

The distribution provided by NASA can be seen in Figure 6.11 . The one obtained with the use of the model in this research was plotted in order to be able to successfully verify and validate it. The results can be seen in the proceeding Chapter 9.

6.4.1. Velocity Distribution

The NASA model describes the distribution of the relative velocity magnitudes of explosion fragments as seen in Equation 6.10. The velocity distributions were obtained from on-orbit as well as ground tests (Johnson et al., 2001).

$$D_{\Delta v}^{EXP}(\chi, v) = N(\mu^{EXP}(\chi), \sigma^{EXP}(\chi), v) \tag{6.10}$$

where the respective variables are defined as seen in Equations 6.11 to 6.14

$$\chi = log_{10}(A/M) \tag{6.11}$$

$$v = log_{10}(\Delta v) \tag{6.12}$$

$$\mu^{EXP} = 0.2\chi + 1.85 \tag{6.13}$$

$$\sigma^{EXP} = 0.4 \tag{6.14}$$

where

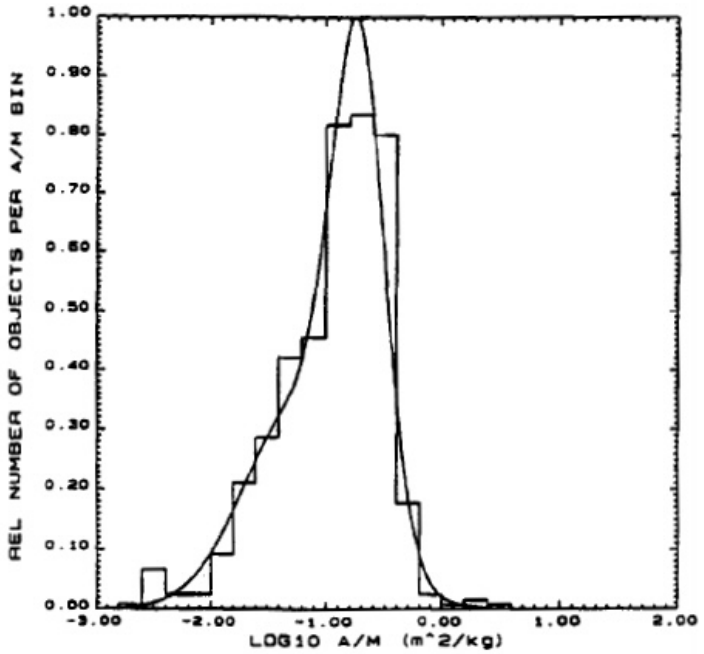

Figure 6.11: Sample A/M distribution function matched to data for 508 spacecraft debris in the size regime of l l .2 cm to 35 cm (Johnson et al., 2001).

- μ^{EXP} symbolizes the mean
- σ^{EXP} symbolizes the standard deviation.

NASA's Breakup model provides the velocity distribution curve obtained from composite ejection velocities for 1,486 objects created in the breakups of Delta, Ariane, and Cosmos upper stages. The results of this distribution can be observed in Figure 6.12 (Johnson et al., 2001).

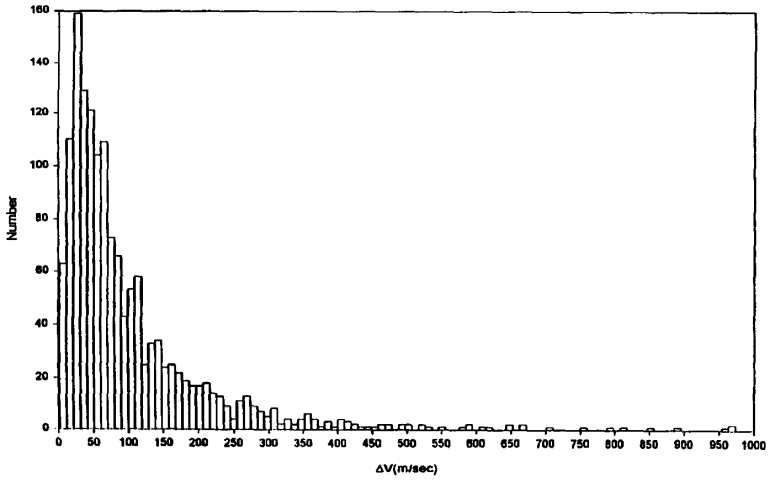

Figure 6.12: Composite ejection velocities for 1,486 objects created in the breakups of Delta, Ariane, and Cosmos upper stages (Johnson et al., 2001).

In order to obtain the velocities for the fragments used for the simulation the same approach was used as the one used for the size distribution. A velocity probability curve was generated using the original distribution. Similarly, a random generator was used to generate a population of 10,000 fragments with their respective velocities based on the probability curve. These were then combined with the sizes based on an index assigned to each of the fragments. In this way, a population was created with 10,000 fragments each with its unique size and velocity.

6.5. Explosion Geometry

Once the sizes and the relative velocity magnitudes were obtained the initial position vectors of the 10,000 debris fragments were generated. This was done by assuming that the exploded fragments have an equal probability of exploding in all directions. A unit sphere was used with random generation, for both elevation and azimuth. The results can be seen in Figure 6.13. As can be seen the sphere looks evenly populated in all directions.

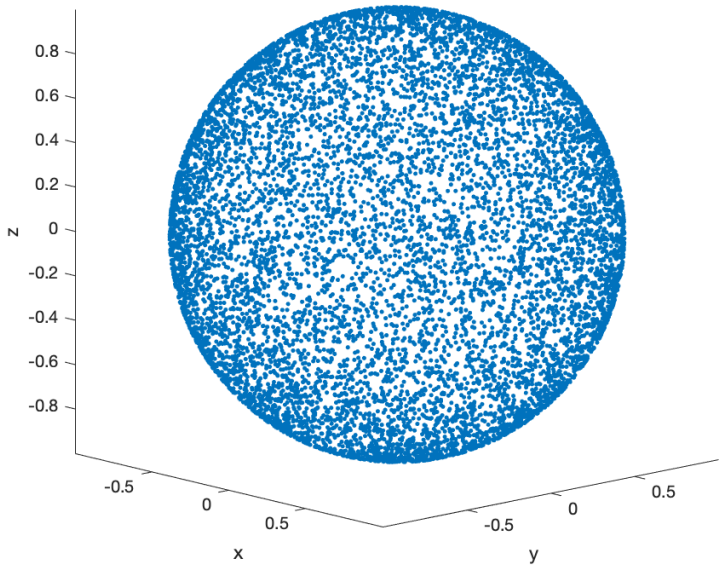

Figure 6.13: Results of fragments distribution on a randomly generated unit sphere.

6.6. Final Fragment Data Generation

Once the raw data (size, mass, velocity, three-dimensional direction of the velocity) was obtained for the fragments, the original satellite velocity was added to obtain the initial state vectors of the fragments as observed in Equation 6.15.

$$\vec{V}_{fragment_i} = [V_{x_0}, V_{y_0}, V_{z_0}]_i + [V_{x_{sat_0}}, V_{y_{sat_0}}, V_{z_{sat_0}}] \tag{6.15}$$

where

- $V_{x_0}, V_{y_0}, V_{z_0}$ are the initial velocity components in x, y, z, of the fragments obtained from the model at the time of explosion
- $V_{x_{sat_0}}, V_{y_{sat_0}}, V_{z_{sat_0}}$ are the initial velocity components in x,y,z of the satellite right before the explosion.

It is important to note that the explosion is instantaneous, so the initial position of the debris and the satellite can be assumed to be the same at the moment of explosion. This led to a data set of 10,000 fragments with their respective position, velocity, size and mass. A deeper insight into the specifics of the data generated will be provided in the Methodology chapter. It is important to note, that given the procedure mentioned for the data generation, the velocity magnitude, velocity direction and size distributions are independent of each other. Meaning that, all combinations are possible i.e. small fragments with low velocities, small fragments with high velocities, etc.

7

Conjunction Analysis

This chapter will look at the conditions put in place to determine if a conjunction between the catcher spacecraft and the debris fragments takes place. In order to do this a set of steps was followed as a means to simplify the problem at hand and reduce Central Processing Unit (CPU) time. The chapter will describe an ellipse intersection analysis, the minimum distance analysis, interpolation, conjunction conditions and case studies used.

7.1. Ellipse Intersection

Given that Kepler orbits were used for both the debris and the catcher spacecraft, a simple ellipse intersection analysis was done to discard fragments that would never intersect within a desired distance *D*. This step was done at the beginning of the analysis to reduce CPU time. This analysis is described by Hoots et al., 1984 as the Perigee-Apogee test.

When looking at two objects, their orbits can be described as an ellipse with unique values for their apogee and perigee radii. In this case, the smaller of the two apogee radii will be defined as Q while the larger of the two perigee radii will be defined as q. The two objects compared were each individual debris fragment to the catcher spacecraft. In said case, if the condition in Equation 7.1 was met, the fragment was discarded.

$$q - Q > D \tag{7.1}$$

where *D* denotes a desired distance chosen by the user, in this case, 20 meters was chosen, as this is defined as the minimum passing distance. The depiction of this test can be seen in Figure 7.1

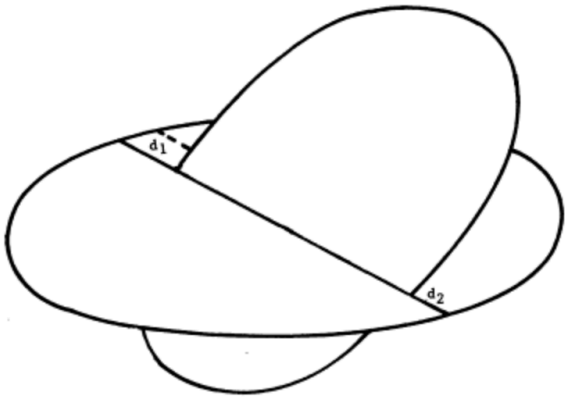

Figure 7.1: Geometric ellipse intersection prefilter (Hoots et al., 1984).

Once the ellipse intersection test was carried out on all fragments, those which met the condition shown in Equation 7.1 were discarded. Nonetheless, given the nature of the problem, all fragments came

within the desired limit so none of them were discarded according to the ellipse problem. This can be attributed to the fact that at least during one point in the ellipse, both the fragments and the spacecraft share a position, namely the initial position.

7.2. Relative Distance

The key element of this thesis, is to be able to determine the relative distance between the debris fragments and the catcher spacecraft, in order to be able to determine if there is a conjunction, i.e. capture situation. In order to do this, it was crucial to have both the debris fragments and the spacecraft in the same coordinate system. As aforementioned, both Kepler elements and Cartesian elements were used throughout the simulation for the thesis.

7.3. Fragment Orbit Propagation

While the catcher satellite was propagated for steps of 0.1 seconds, carrying out the same task for 10,000 debris fragments demonstrated to be a CPU-expensive task. Consequently, a time step of 60 seconds was chosen. For the latter, this implies that in a matter of one time step, with a relative velocity of approximately 15 km/s, the relative distance can change by almost 1000 km. The reasoning for the choice of numbers will be further explained later in the chapter. Every time step, the relative distance was computed, checked and a set of criteria were defined to decide upon the proceedings of the data. One procedure which was implemented, to deal with the large possible variation in the relative distance, was the minimum distance, explained in the next section. In short, the analysis is done in a numerical way as opposed to analytically. This involves sampling and testing against conditions.

7.4. Minimum Distance

Although the perturbations were discarded and Kepler orbits were used for all fragments, CPU time still proved to be a problem. For this reason, minimum distance was used as opposed to standard propagation. This entailed looking at the initial state of the debris and the spacecraft at a certain time and calculating the predicted minimum distance if the debris were to fly (relatively) in a straight line. The relationship shown in Figure 7.2 can be summarized into Equation 7.2.

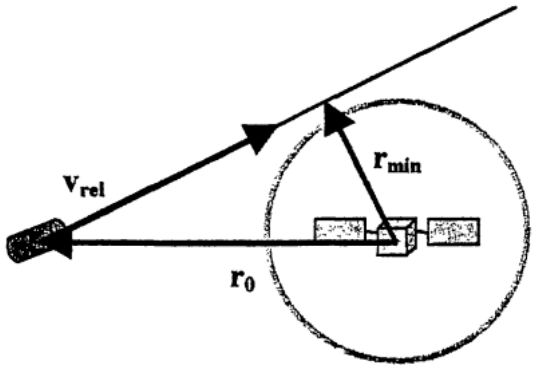

Figure 7.2: Minimum distance neglecting acceleration (Alarcón Rodríguez et al., 2002).

$$r_{min} = \sqrt{r_0^2 - \left(\vec{r}_0 \cdot \frac{\vec{v}_{rel}}{v_{rel}}\right)^2} \tag{7.2}$$

However,since it is based on a linear relative motion, the minimum distance rule can only be used for small distances r_0 (corresponding to small time intervals between the reference epoch and the moment of minimum distance). Given large initial distances, the error incurred between the linearized minimum distance and the real distance at that time could very well be significant. For this reason, once the minimum distance was obtained with Equation 7.2, the time taken to travel from r_0 to r_{min} was

calculated. This was done by taking the distance traveled as seen in Figure 7.2 with Equation 7.3.

$$r = \sqrt{r_0^2 - r_{min}^2} \tag{7.3}$$

Once the distance traveled was obtained, the time taken was estimated with Equation 7.4.

$$\Delta t = \frac{r}{v_{rel}} \tag{7.4}$$

The Δt (Figure 7.3) obtained was then added to the original time t_0 and then the Kepler propagation was used to obtain the real state of the fragment at the time of the linearized minimum distance r_{min}. This led to a new value of r_0 and v_{rel} and using these, Equations 7.2 to 7.4 were implemented again and the real minimum distance state was obtained again. This process was carried out until the minimum distance converged within the imposed limits for the minimum passing distance, in this case, 20 meters. Smaller possible radii of the spacecraft were explored in post processing. A depiction of the error incurred between the linearized minimum distance r_{min} and the real distance $r_{min}real$ can be seen in Figure 7.3. The grey dot would be the state of the debris fragment where it to follow a linear trajectory and the blue dot represents the fictitious real state of the fragment. This results in the difference in r_{min} that is mentioned above. For this reason the real state of the fragment is calculated at time t_f to correct for the uncertainty incurred by assuming linear behavior.

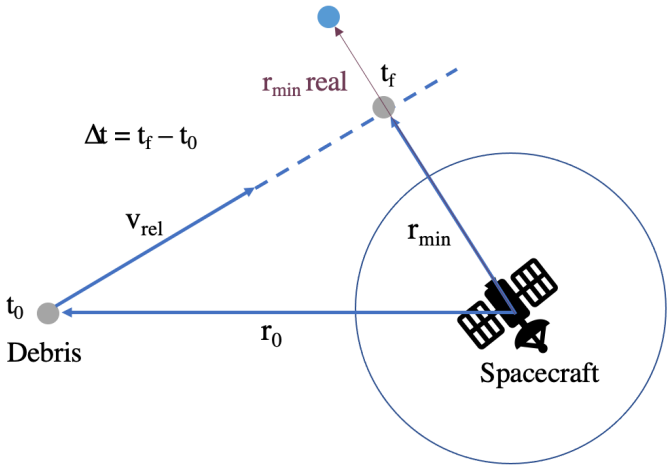

Figure 7.3: Minimum distance obtained using linearization versus real minimum distance due to curvature of the orbit. The blue dot represents the real debris and its position, the grey dot is the debris fragment position with the linearized formula.

7.5. Interpolation

In order to save CPU time, the state of the catcher spacecraft was first propagated in steps of 0.1 seconds and stored. This allowed for a direct comparison of the relative distance between the fragments and the spacecraft. However, as described in Sections 7.3 and 7.4, the fragments are propagated in steps of 60 seconds. Similarly, when carrying out the minimum distance calculation a new arbitrary time is obtained which is not necessarily an epoch which corresponds exactly to the spacecraft data calculated (i.e. not a multiple of 0.1). An example of this can be observed in Figure 7.4. Here it can be seen that the states for the satellite at multiples of 0.1 s are known however when a different time is taken into account position and velocity are unknown. For this reason, interpolation was carried out to obtain the position and velocity of the satellite at that particular moment in time. When looking at interpolation types three were taken into account: linear, quadratic and cubic spline. A small overview of each will be given along with the one chosen and the reason why. In order to be able to chose the best interpolation type an accuracy requirement of 1 mm will be set given that the data set sizes range from 1 mm to 10 cm.

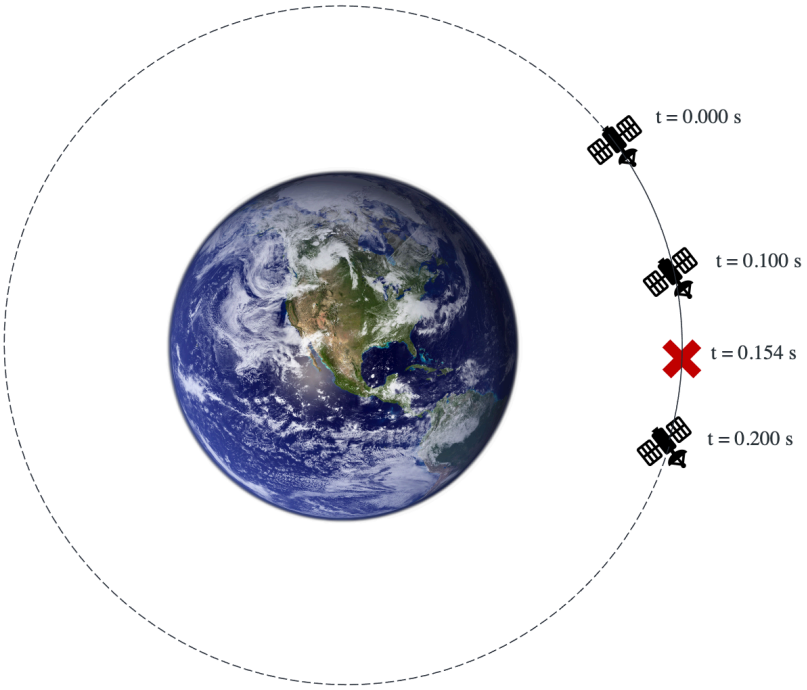

Figure 7.4: Illustration of known positions (at discrete steps of 0.1 s) versus unknown position (at 0.154 s).

7.5.1. Linear

One of the possible interpolation types often used is linear interpolation. This type of interpolation is a first-order polynomial representing a straight line between two points as seen in Figure 7.5 (Steffensen, 2006).

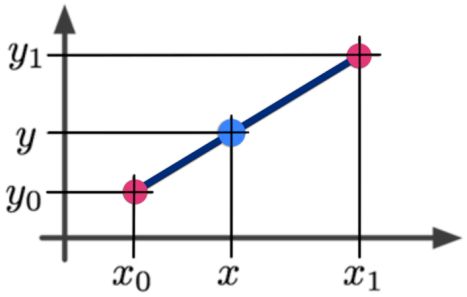

Figure 7.5: Depiction of linear interpolation.

This relationship can be seen in Equation 7.5 (Steffensen, 2006).

$$y_1(x) = y(x_0) + \frac{y(x_1) - y(x_0)}{x_1 - x_0}(x - x_0) \tag{7.5}$$

However, linear interpolation incurs large errors when looking at non-linear curves or at large intervals (Steffensen, 2006). In the case at hand, the satellite position and velocity were obtained every 0.1 s and although that may seem like a small interval when traveling at 7.5 km/s one can travel 750 meters in such an interval. Given the accuracy requirement for the problem (1 mm), it can be seen that linear interpolation would not work for the problem at hand. However a better insight into this will be provided throughout the chapter.

7.5.2. Quadratic

As aforementioned in the case of a curve, the error resulting from linear interpolation is expected to be very large. For this reason, a second-order polynomial interpolation can be used. This can only be

used when there are at least three data points available. The expression to describe this interpolation can be seen in Equation 7.6 (Steffensen, 2006).

$$y_2(x) = b_0 + b_1 (x - x_0) + b_2 (x - x_0)(x - x_1) \tag{7.6}$$

where the different coefficients are defined as seen in Equations 7.7 to 7.9 (Steffensen, 2006).

$$b_0 = f(x_0) = y(x_0) \tag{7.7}$$

$$b_1 = \frac{y(x_1) - y(x_0)}{x_1 - x_0} \tag{7.8}$$

$$b_2 = \frac{\frac{y(x_2) - y(x_1)}{x_2 - x_1} - \frac{y(x_1) - y(x_0)}{x_1 - x_0}}{x_2 - x_0} \tag{7.9}$$

7.5.3. Cubic Spline

Cubic Spline Interpolation consists of using a third-degree polynomial such as that seen in Equation 7.10:

$$f(x) = \begin{cases} a_1 x^3 + b_1 x^2 + c_1 x + d_1 & \text{if } x \in [x_1, x_2] \\ a_2 x^3 + b_2 x^2 + c_2 x + d_2 & \text{if } x \in (x_2, x_3] \\ \dots & \\ a_n x^3 + b_n x^2 + c_n x + d_n & \text{if } x \in (x_n, x_{n+1}] \end{cases} \tag{7.10}$$

In this case, the unknown coefficients are determined by generating a matrix given the known points of passing. This results in an accurate solution for functions that have multiple inflection points.

7.5.4. Interpolation Choice

In order to be able to choose the optimal interpolation technique the error incurred by the interpolation options was compared. The error was obtained by getting the difference between the interpolated position for arbitrary time steps and the position obtained with the Kepler solver. This was carried out for linear, quadratic, and cubic spline interpolation. The same procedure was carried out for the velocity. The results of the errors incurred in the position can be observed in Figure 7.6.

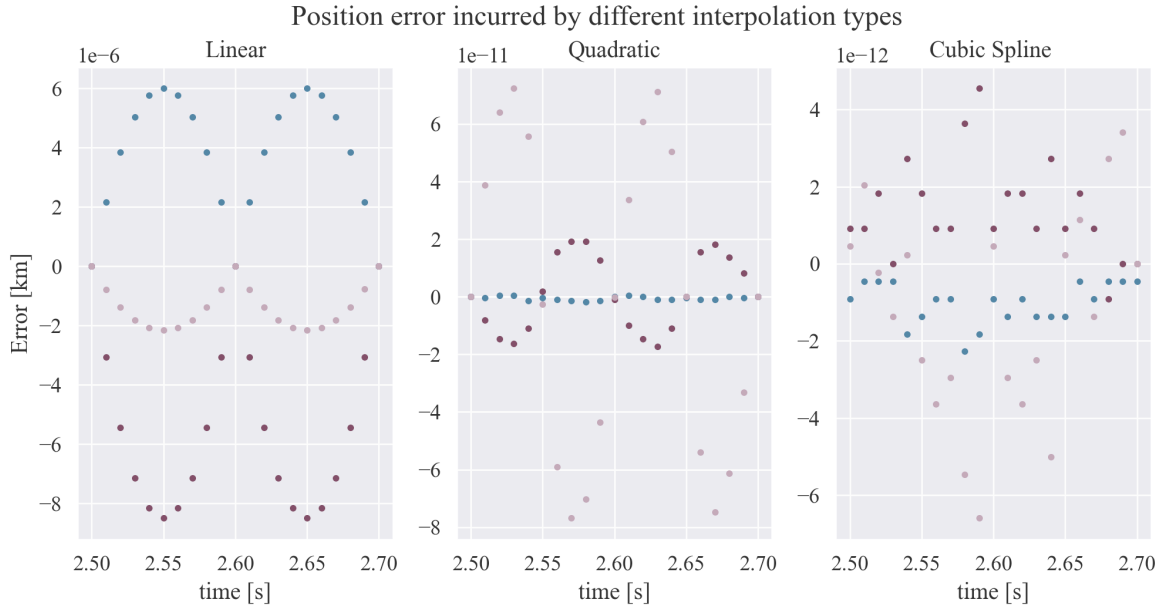

Figure 7.6: Error incurred by linear, quadratic and cubic spline interpolation for a set of data points between the interpolated position of the catcher of the satellite and the position obtained through the Kepler solver for the x, y, z components.

Next the same error was shown for the velocity of the satellite. The errors incurred by the interpolation types can be seen in Figure 7.7. At the time steps which are multiples of 0.1s, the real position is

known, and thus used to interpolate. For the linear and quadratic case, at these time steps, the error is 0 km as expected (Figure 7.6). This holds for both the position and the velocity. In the linear case the error increases the further you get from the known time steps (i.e. 2.55, 2.65, etc.). The quadratic case shows the minimum error every half a time step, and maximum error at a quarter time step(i.e. 2.555, 2.655, etc.). The error incurred by cubic spline interpolation shows a randomized behavior, this could be attributed to the small magnitude of 1e-15 km which could be attributed to noise.

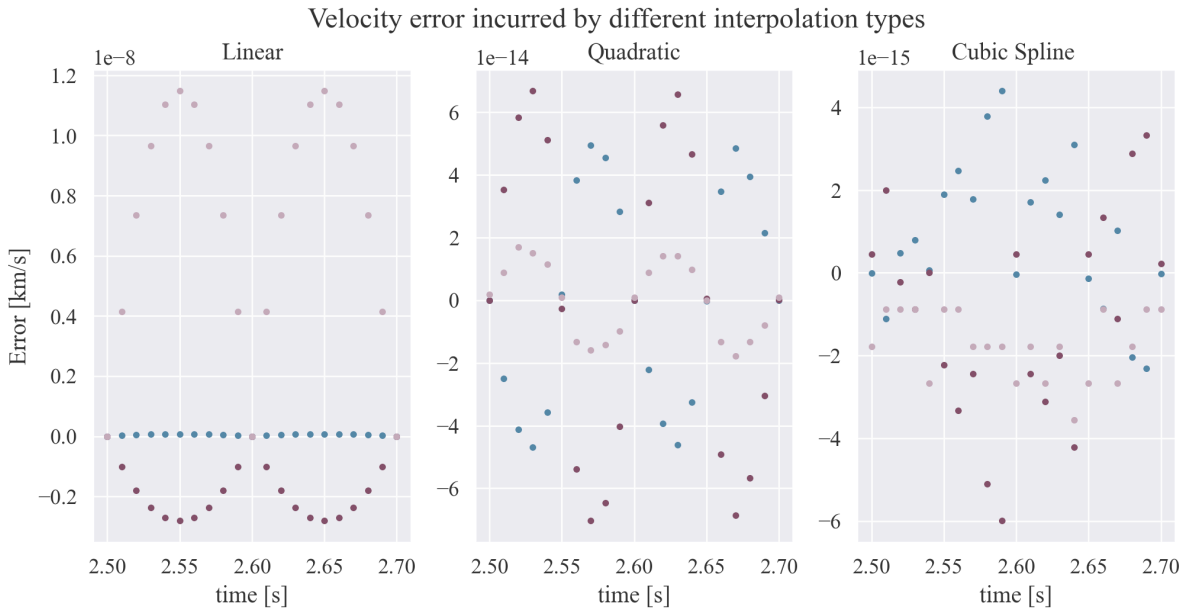

Figure 7.7: Error incurred by linear, quadratic and cubic spline interpolation for a set of data points between the interpolated velocity of the catcher of the satellite and the position obtained through the Kepler solver for the x, y, z velocity components.

Similarly, all interpolation types provided similar CPU times so there wasn't a drawback in using a third-degree interpolator over a second or first-degree.
Overall, it can be seen that the cubic spline interpolator yields the best accuracy. Linear interpolation shows better accuracy than expected but is above the desired value of 1 mm. Quadratic interpolation also shows very accurate results but given that cubic spline has a a better accuracy this will be used. The errors incurred for the velocity calculations are smaller but the same applies here; cubic spline yields a more accurate results and thus will be used for the study at hand.

7.6. Capture Conditions

In order to be able to successfully define a conjunction, or in other words, when a fragment was caught, a set of conditions had to be put into place. These conditions were defined as follows:

- The minimum passing distance between the debris and the catcher spacecraft will be defined as 20 m, for the conjunction stopping criterion.
- The catcher spacecraft will be simulated to move in the opposing direction of the fragments
- The catcher spacecraft will be placed in the same orbit as that of the Kosmos 1408 with the exception of the direction of motion as aforementioned.

The first condition served as a limit to be able to quantify the number of fragments caught with such a large radius. However, all data which passed the initial test of 1,000 km (see Chapter 8) was saved to be able to analyze what would happen if smaller or larger spacecraft were to be employed. The second condition was established such that the catcher spacecraft doesn't chase the debris but encounters them head-on, resulting in a larger expected number of potential conjunctions. The third condition was put into place as the nominal orbit is approximately the mean orbit of all fragments.
In the following Methodology chapter, an overview will be given to provide an outlook of how these individual sections will result in the overall conjunction simulation.

8

Methodology

In the previous chapters, a general outlook was given on individual parts of the data generated as well as the simulation. This chapter will provide an outlook on the combination of said aforementioned tasks in an attempt to provide a clear picture of how the results were obtained.
To do this, it will provide a general overview of the methodology and go into each individual part in detail to bring forth a detailed description of the methodology implemented for this thesis. This will include detailed fragment data generation, satellite data generation and the overall simulation.

8.1. Summary of the Simulation

On a general scale, the simulation consisted of three main parts dealt with in Chapters 4 to 6, these were then combined as described in Figure 8.1. Starting from the first task, the break-up model found was the NASA Break-up model 4.0, this was verified as described in Chapter 9: Verification and Validation. Next, the geometry of the explosion was defined, in this case, it was defined as a catastrophic explosion with equal probability of particles ejecting in all directions. Combining these steps, a dataset of 10,000 fragments, with their respective position and velocity, was generated.
Once the fragment dataset was created, a Python script going from Cartesian coordinates to Kepler elements was developed as described in Appendix A. This served to obtain the orbital elements of all fragments as a means to efficiently propagate the orbit. The next step was to generate a Python function for the orbit propagation.

During this study, a set of case studies (Table 8.1) was defined pertaining to the time of deployment as well as injection inaccuracies to get a better picture of the evolution of the cloud and the interaction with the catcher spacecraft. Each of these case studies has individual initial conditions for both the fragments as well as the catcher spacecraft. In the next step, these initial conditions were defined for one of the case studies chosen.
Next, the orbit of the catcher satellite was propagated given said initial conditions. Similarly, the new orbital elements of the fragments were obtained following the initial conditions.

Once all the necessary data was obtained, the overall simulation was run in order to determine if the fragments could be caught or not. A more detailed insight into the simulation will be given in the proceeding sections. Upon the conclusion of the simulation, the new case study's initial conditions were defined and the process was repeated as shown in Figure 8.1.

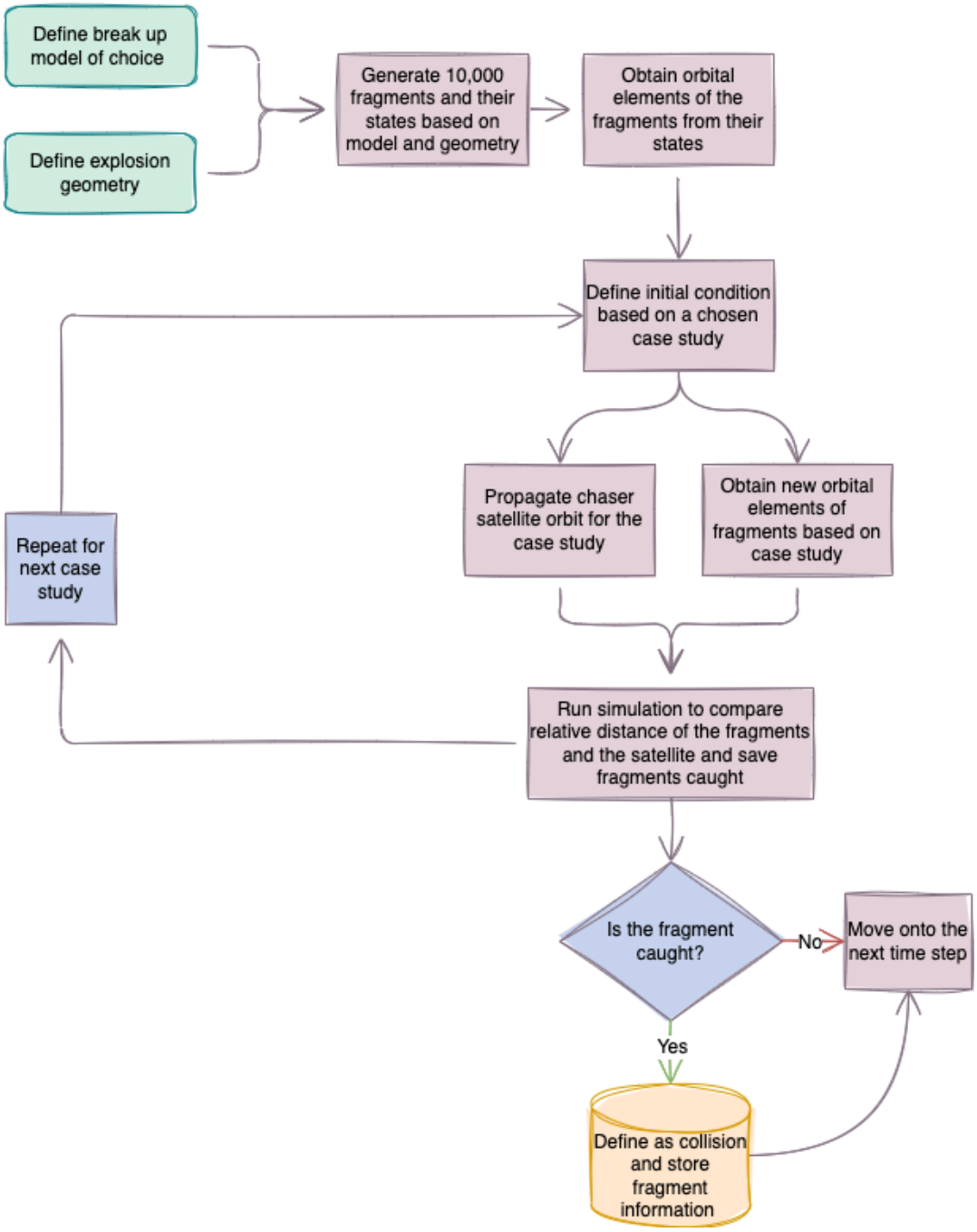

Figure 8.1: Top-level flow chart of the methodology used to obtain the final number of caught fragments.

8.2. Fragment Data Generation

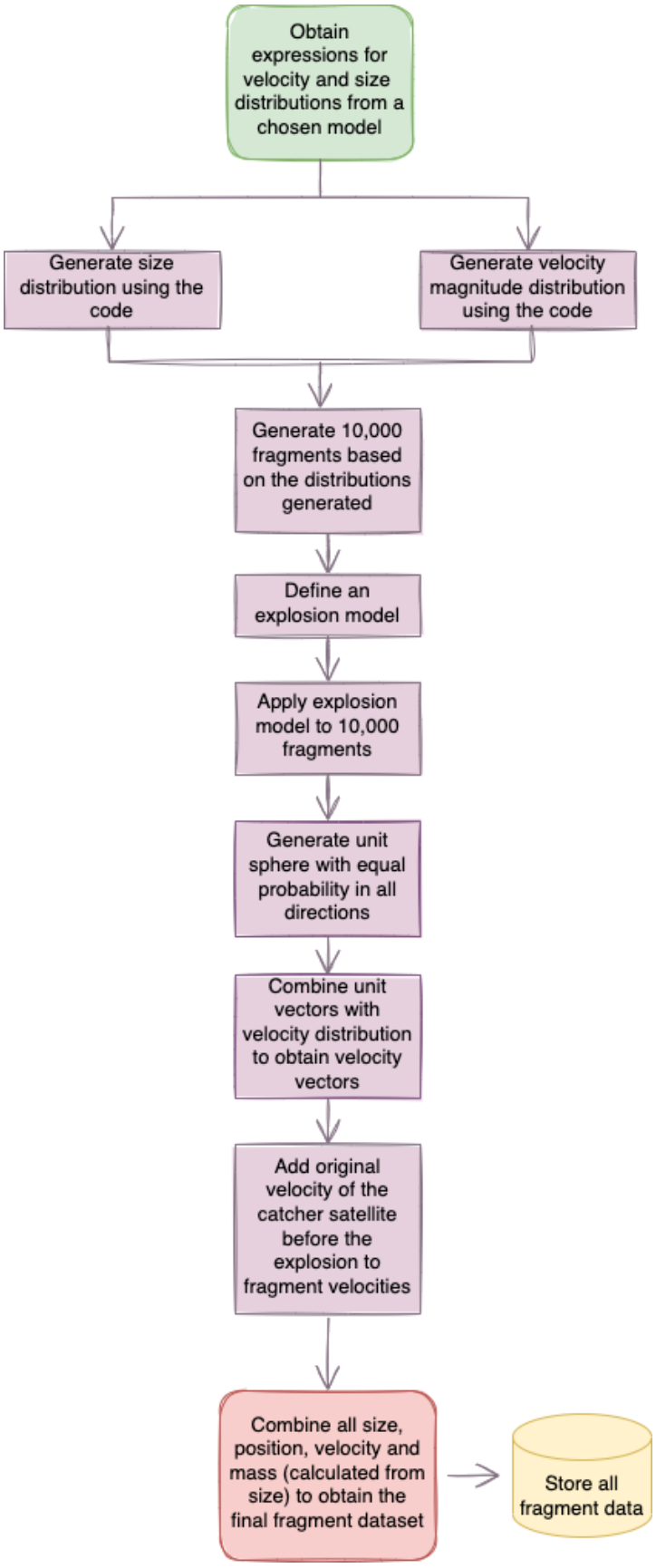

Figure 8.2: Flow chart of the methodology used to obtain the fragment data.

This section will provide a deeper insight into fragment data generation. In order to get an overview of the procedure one can refer to Figure 8.2. As mentioned in Section 8.1 the first step of the data generation was to define the break-up model. In order to assure that this model was recreated properly on software of choice, in this case Python, it was important to verify it with the provided data and plots. An overview of this verification can be seen in Chapter 9.
Once the model was verified and comprehended, the necessary expressions for the distributions of fragments due to an explosion were identified. These were then modeled in Python in order to obtain two different distributions; velocity magnitude, and fragment size. These distributions were then used to generate 10,000 fragments with their individual data points for the distributions mentioned. Using Equation 6.1 the mass was calculated from the size distribution.
Nonetheless, in order to be able to simulate the orbit, the velocity direction was necessary which brings about the second part of the fragment generation, namely the explosion model. In order to simulate the explosion the following assumptions were made:

1. The explosion was deemed to be catastrophic

2. The fragments could explode with equal probability in all directions

Given those two assumptions, the explosion was modeled by generating a unit sphere with 10,000 points generated with equal probability in all directions as that presented in Figure 6.13 in Chapter 6. This provided a set of 10,000 three-dimensional unit vectors. These vectors were combined with the generated velocity magnitude dataset, to obtain the initial three-dimensional velocity of the fragments upon explosion, thus giving a starting point for the simulation. However, in order to obtain the real initial velocity of the fragments, the original satellite velocity was added, given that, when the satellite explodes, it is moving with a certain velocity and is not stationary. In the case of Kosmos 1408, the original velocity can be seen in Equation 8.1.

$$\vec{v}_{sat_0} = \begin{bmatrix} 0.07862035 & -1.85851714 & 7.39725628 \end{bmatrix} \text{km/s} \tag{8.1}$$

Lastly, the new velocities were combined with the size, position and mass to obtain the final fragment data set.

8.3. Satellite Data Generation

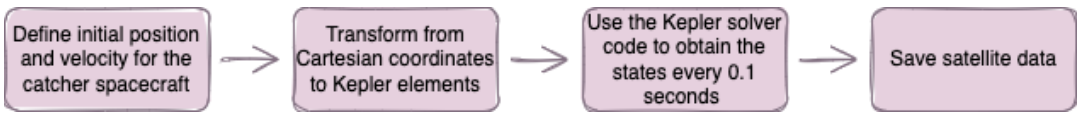

Figure 8.3: Flow chart of the methodology used to obtain the catcher spacecraft data.

The satellite data was generated once at the beginning of each simulation in order to reduce CPU time. As seen in Figure 8.3 first the initial position and velocity of the catcher spacecraft were determined based on the case study. Next, these were transformed from Cartesian elements to Kepler elements and then the state was propagated in time steps of 0.1 seconds. The results were then converted back to Cartesian coordinates and stored.

8.4. Ellipse Intersection

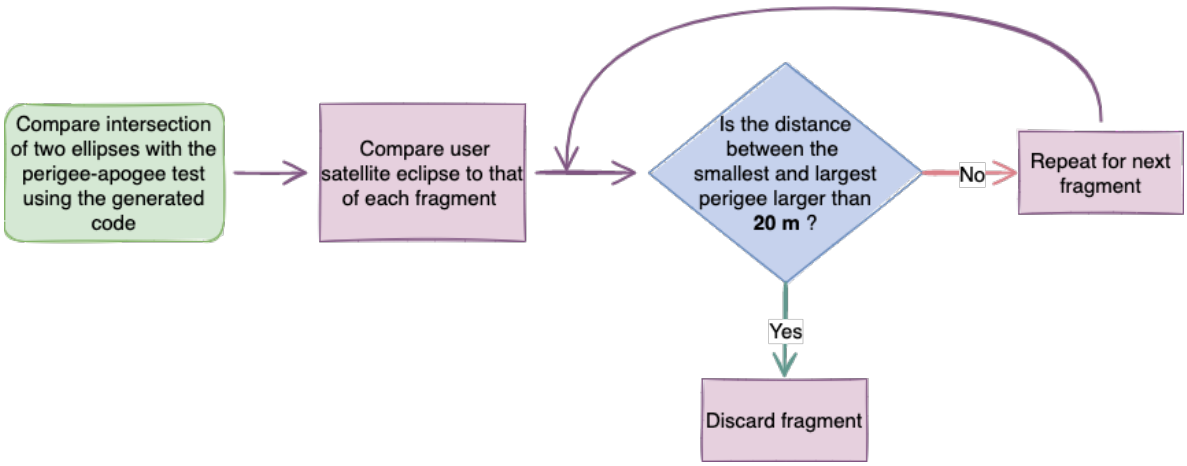

Figure 8.4: Flow chart of the methodology used to carry out the ellipse intersection check.

The ellipse intersection was carried out before the simulation as a means to discard fragments that could never intersect. To do this the perigee apogee test was used. Using the test, it was calculated if the distance was larger than 20 m. If it was, the fragment was discarded and if not the fragment was kept as a candidate conjunction element.

8.5. Main Simulation

This section will provide a detailed overlook of the simulation. The simulation was initialized by loading the position and velocity of the satellite at time = 0 s. Similarly, the fragment data was loaded and converted to Cartesian elements to obtain position and velocity at the initial time. Once those were obtained, the relative distance was calculated and if it was 20 m or less, the fragment and its data was stored. If the distance was larger the next epoch was propagated. Step sizes of 60 seconds were used as a means to save CPU time. This implies that at the epoch one time equates to 0 seconds, the second epoch refers to 60 seconds, the third to 120 and so on.

Once the states of the fragment were propagated for 60 seconds, the relative distance to the spacecraft at 60 seconds was calculated. The first distance check was done for 1,000 km, this is because at a relative velocity of approximately 15 km/s such as that encountered in this study, in 60 seconds the relative distance traveled would be 900 km. If this test failed, no conjunction could be possible anywhere in the current 60 second interval and then the state was propagated to the next epoch and the process repeated. However, if the test passed, then the minimum distance calculations were carried out as explained in Chapter 7.

As soon as this was done, the next check had to be carried out, this time for a distance criterion at 100 km with the same outcome. If negative the state at the next epoch was calculated and if positive the minimum distance procedure was carried out. This iterative process kept being repeated decreasing the distance by a factor of 10 every time. In the end the checks carried out were 10^3, 10^2,10^1,10^0,10^{-1},10^{-2} and 10^{-3} km. If the outcome of all of the checks was positive then the outcome was defined as a collision and the fragment was deemed caught. Once this process was completed, the next fragment was analyzed. This was repeated for all 10,000 fragments.

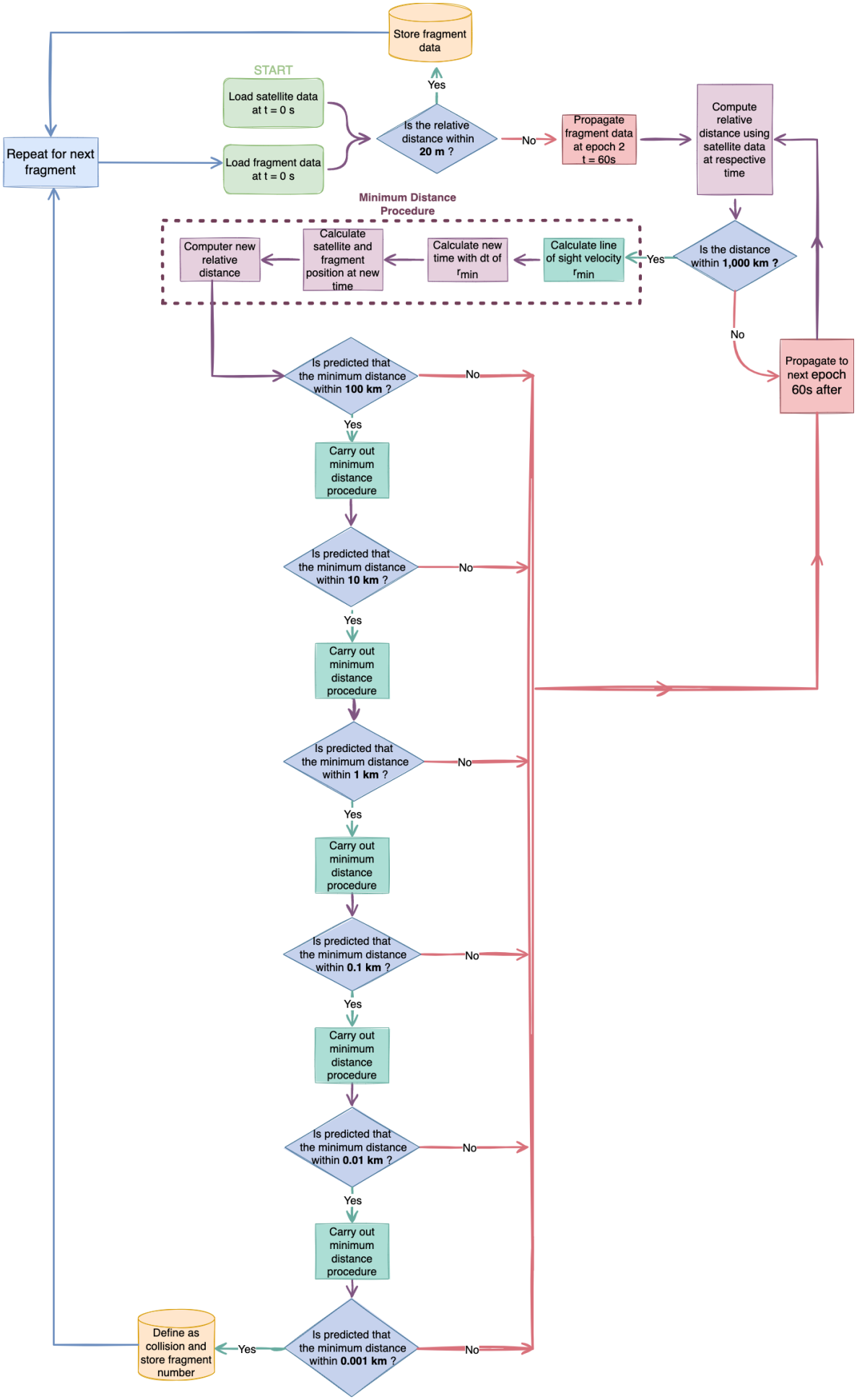

Figure 8.5: Flow chart of the methodology used to create and carry out the simulation.

8.5.1. Case Studies

The main simulation will be carried out for a set of case studies as a means to answer the posed sub questions. These case studies encompass the injection time of the satellite with respect to the time of the explosion which will be defined as t = 0. Next, two case studies will be analyzed in which there are injection inaccuracies for the altitude and for the inclination, these case studies will be combined with a nominal injection time as seen in Table 8.1. This combination of case studies will yield a set of eight case studies seen in Table 8.1. Next the effect of varying the size of the catcher radius will be examined by analyzing the resulting the dataset of the main simulation for the eight case studies. The catching radius sizes analyzed will be 1 m, 5 m, 10 m, 20 m, 50 m and 100 m.

Case Study Number	Injection Time	Injection Inaccuracy
1	10 s	N/A
2	3 h	N/A
3	6 h	N/A
4	12 h	N/A
5	24 h	N/A
6	48 h	N/A
7	12 h	+ 0.1 deg inclination
8	12 h	+ 10 km altitude

Table 8.1: Definition of case studies explored in this study.

9

Verification and Validation

This chapter will deal with the verification and validation of the constituents used to obtain the results of this thesis study. This will include the break up model, the explosion geometry and the respective parts of the code used to create the simulation. Verification will be used to make sure that the respective parts do what they are supposed to while validation will serve to check that everything is done correctly and is in agreement with ”physical truth”. This will ensure that the results of the model are correct.

9.1. NASA Breakup Model 4.0

The main model used to describe the behavior of the debris fragments upon explosion in this study is the NASA Break-up model 4.0 (Chapter 6). This model served to provide density, size, Δv and area-to-mass ratio. The model provides various equations for different-sized fragments but only illustrates the behavior of larger fragments. This study concerns itself with fragments smaller than 10 cm, and therefore the equations at hand had no direct verification method. For this reason, the parameters for larger fragments were coded and compared to the illustrations provided in the report; once those were verified the variables were changed to correspond to the smaller fragments. In this manner, it was reassured that the application of the model in the code was correct. These illustrations will be shown in the proceeding subsections.

9.1.1. Size Distribution

The expressions for size distribution were presented in Chapter 6. The results were plotted and compared to the existing model plots. As aforementioned, the NASA Break-up 4.0 model deals with fragments of sizes ranging from 10 cm to 10 m. Nonetheless, as can be seen in Figure 9.1, if the model were extended, it would fit perfectly with the model used in the thesis. For this reason, the size distribution of the model was deemed validated and verified.

9.1.2. Area-to-Mass Ratio

In order to verify the area-to-mass ratio part of the model, the distribution for the area-to-mass ratio was plotted and compared to the distribution provided in the NASA model (Johnson et al., 2001). When looking at Figure 9.2 it can be observed, that when plotted together, the NASA model and the model obtained for the thesis are nearly identical. This claim stems from the fact that both plots have the maximum at 1, and the beginning and end points are the same, along with a match for the general shape.

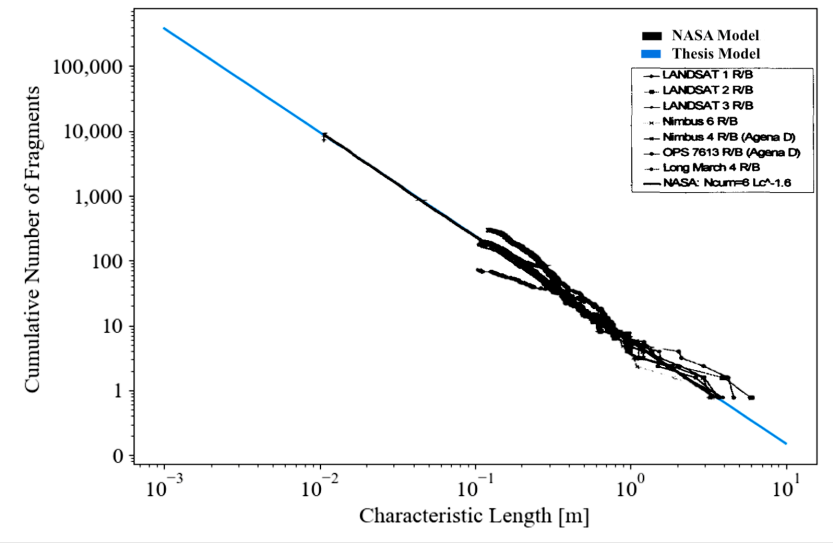

Figure 9.1: Comparison of NASA sample debris size distributions from seven upper stage breakups, as derived from SSN data with the model used for the thesis.

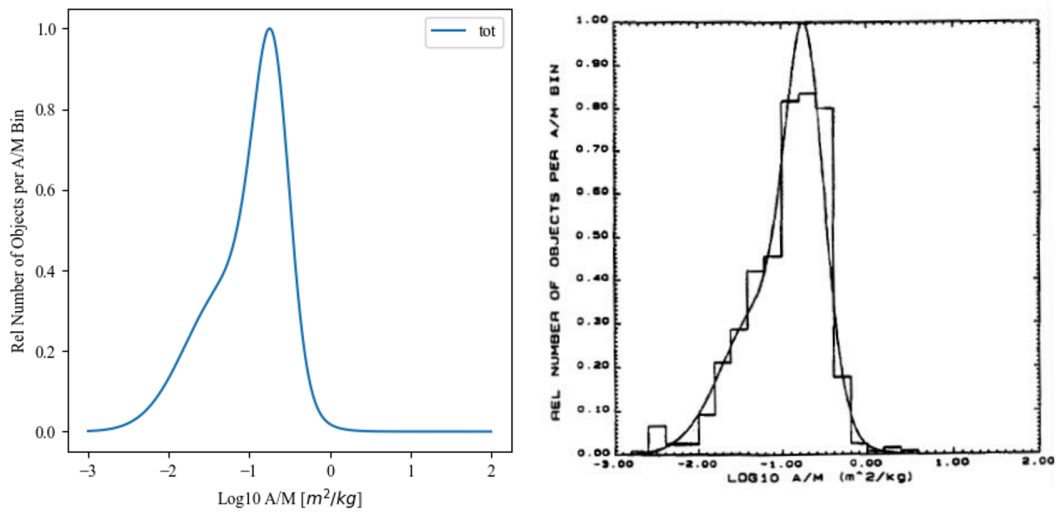

Figure 9.2: **a.** Distribution obtained for the model used in the thesis (left) **b.**Sample A/M distribution of 508 spacecraft debris in the size regime of 11.2 cm to 35 cm (right) compared to the model used for the thesis.

9.1.3. Velocity Distribution

In order to verify the velocity magnitude predictions, the distribution provided in Chapter 6 was used. In order to do this a set of values was generated using the provided equations. This resulted in the distribution seen in Figure 9.3. Johnson et al., 2001 did not provide an overall distribution to compare with. Nonetheless, using the distribution they generated from a real dataset (Figure 9.4) it can be seen that the general trend of the distribution was very similar with a peak at the earlier Δv values and decreasing towards higher values. For this reason, the velocity distribution was deemed verified and validated.

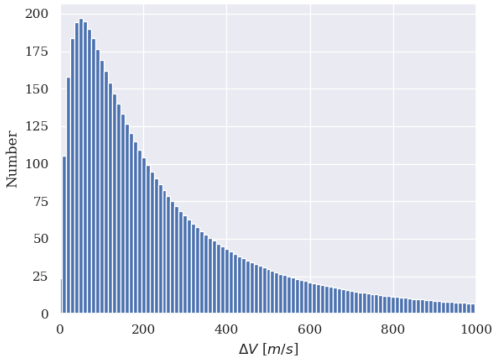

Figure 9.3: Velocity distribution obtained with the model for a population of 10,000 fragments in m/s.

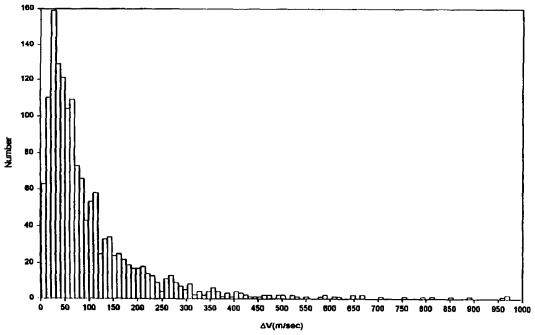

Figure 9.4: Composite distribution of calculated ejection velocities for 1,486 debris from Delta, Ariane, and Cosmos upper stages (Johnson et al., 2001).

9.2. Explosion Geometry

In order to verify the explosion geometry, it was checked that the distribution was uniform for x, y and z coordinates, as can be observed from the top view seen in Figure 9.5.

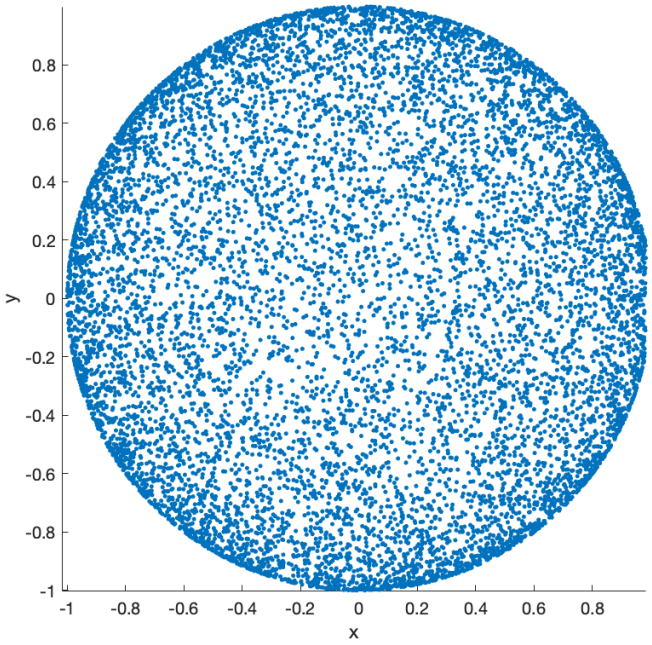

Figure 9.5: Top view of the sphere resulting from the generation of the explosion geometry with equal probability in all directions.

Similarly, in order to ensure that the distribution was the same in all directions for x, y and z the distributions were plotted. The results can be seen in Figure 9.6. It can be observed that the distribution is even from -1 to 1 for all coordinates. There is no larger probability of having coordinates at any specific values for any coordinate. Thus the explosion geometry was deemed verified. Furthermore, from the top view it can clearly be seen that the poles do not show concentration.

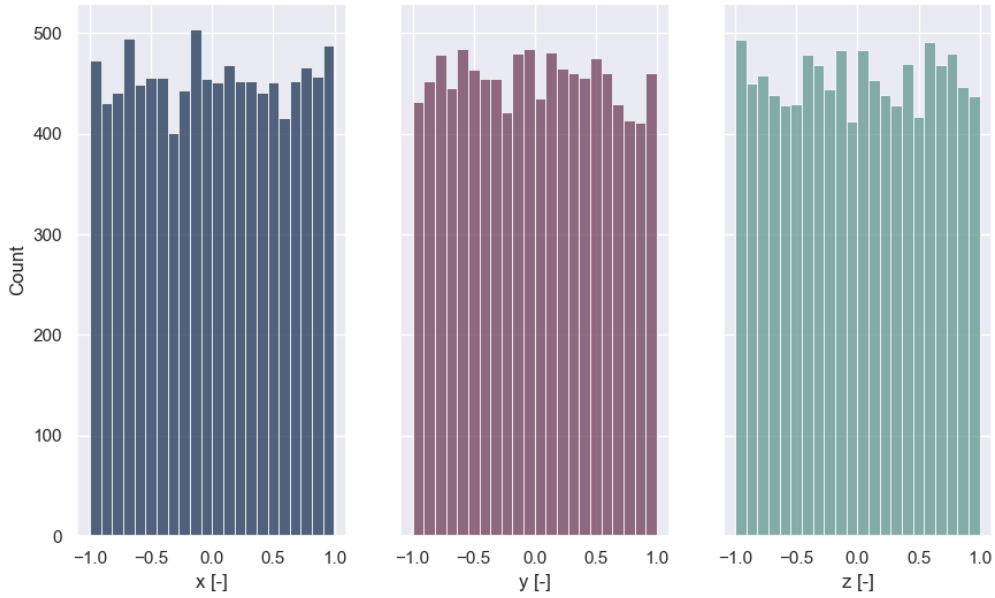

Figure 9.6: Distribution of sphere coordinates resulting from the generation of the explosion geometry with equal probability in all directions with x distribution left, y distribution middle, z distribution right.

9.3. Cartesian to Keplerian

In order to verify the Cartesian coordinate to Kepler element conversion, existing ISS coordinates were used which were known both in Cartesian and in Kepler elements. These were input as Cartesian coordinates into the Python code developed and the outcome was then compared. The results of this comparison can be found in Table 9.1. It can be observed that the results proved to be identical to those provided by NASA (NASA, 2014). The error was calculated to be 0.000% for the maximum number of significant figures displayed by NASA.

Parameter	NASA Value	Obtained Value	Error [%]
a [m]	6787746.891	6787746.891	0.000
e [-]	0.000731104	0.000731104	0.000
i [deg]	51.687144860	51.687144860	0.000
Ω[deg]	127.548670600	127.548670600	0.000
ω[deg]	74.219871370	74.219871370	0.000
Θ[deg]	24.100276770	24.100276770	0.000
E [deg]	24.083177660	24.083177660	0.000
M [deg]	24.066084260	24.066084260	0.000

Table 9.1: Kepler elements contained by the Cartesian coordinates to Kepler Elements transformation compared to the original NASA values for the ISS.

.

9.4. Keplerian to Cartesian

The same procedure as that carried out for the conversion from Cartesian to Kepler elements was carried out for the transformation from Kepler to Cartesian elements. Similarly, ISS coordinates were used here too and the results proved to be identical in this case as well as can be seen in Table 9.2.

For this reason, the function developed for Kepler to Cartesian coordinates was deemed verified. ISS coordinates were also checked for other epochs but not included for redundancy purposes.

Parameter	NASA Value	Obtained Value	Error [%]
x [m]	-2700816.14	-2700816.14	0.000
y [m]	-3314092.80	-3314092.80	0.000
z [m]	5266346.42	5266346.42	0.000
v_x [m/s]	5168.606550	5168.606550	0.000
v_y [m/s]	-5597.546618	-5597.546618	0.000
v_z [m/s]	-868.874450	-868.878445	0.000

Table 9.2: Cartesian coordinates contained by the Kepler Elements to Cartesian coordinates transformation compared to the original NASA values for the ISS (“Spot the Station: International Space Station”, 2022).

9.5. Kepler Solver

The Kepler solver is the main function to successfully propagate the orbit. In order to verify this, two approaches were taken. The first approach was to plot the orbit and then three-quarters of the orbit and see if the orbit would change accordingly when plotted. The results can be observed in Figures 9.7 and 9.8 where the first figure depicts the full orbit along with the initial point of the spacecraft and the latter depicts three-quarters of the orbit. As can be observed by looking at the plot it can be assumed that when the propagation time is three-quarters of the period, the orbit changes accordingly as expected. Although the results depicted are sufficient to consider the Kepler solver verified, a second approach was taken.

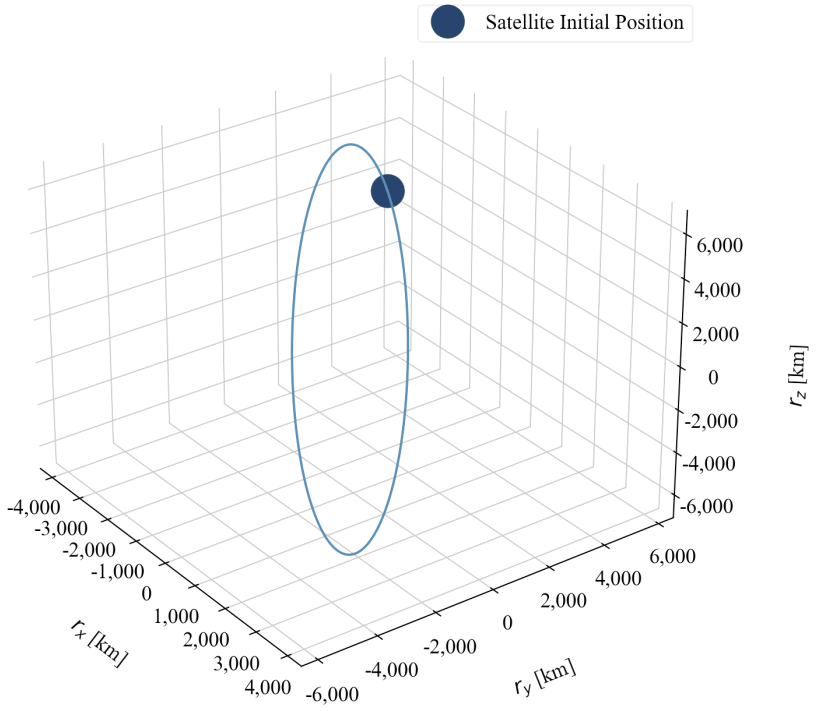

Figure 9.7: Full orbit obtained with the Kepler Solver and initial point of the satellite shown.

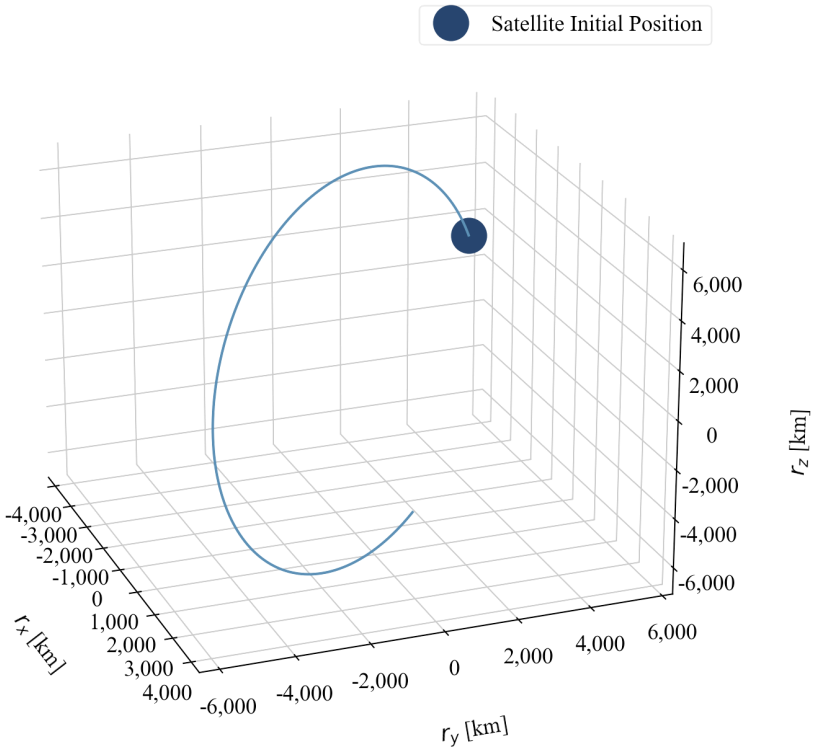

Figure 9.8: Three-quarters of an orbit obtained with the Kepler Solver and initial point of the satellite shown.

Another way to successfully verify the Kepler solver was to plot the eccentric anomaly E, mean anomaly M and true anomaly θ as a function of time. These were plotted for one full orbit. The results can be seen in Figure 9.9.

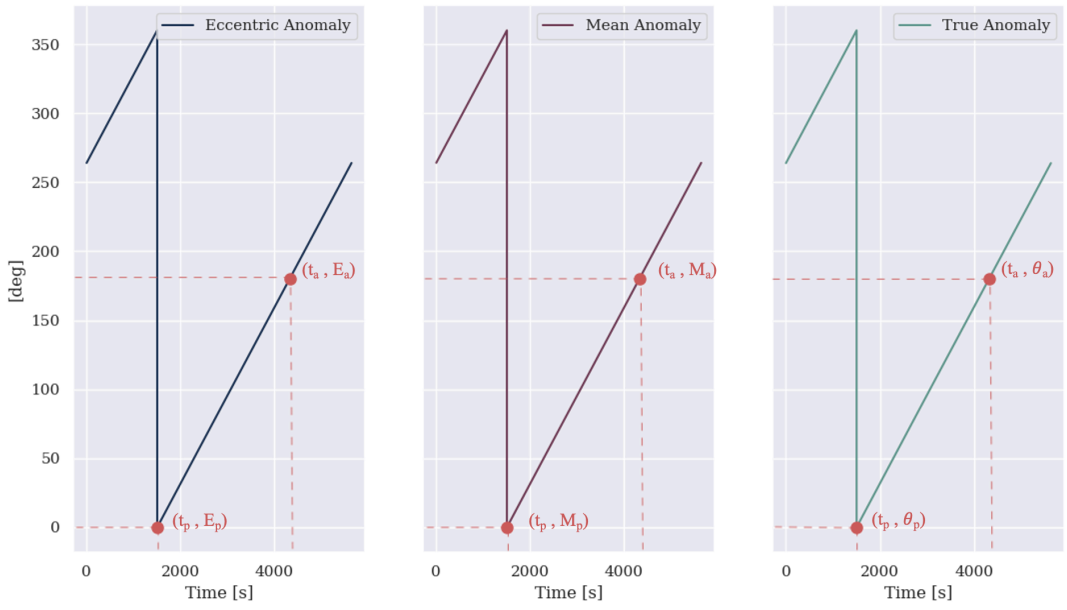

Figure 9.9: Eccentric, mean and true anomaly over one period of the satellite with value and time at perigee *p* and apogee *a*.

It can be seen that for all cases the behavior is periodic and ends at the same value as it starts. Similarly it can be seen that at perigee the value of the anomalies is $0°$ and at apogee it is at $180°$ as expected. Thus the Kepler solver was considered verified.
Similarly the same approach was taken with the altitude, Figure 9.10 a (left) shows the altitude during

the course of one period of the satellite while the right figure shows the altitude during three-quarters of a period. Here it can be observed that the altitude changed proportionally by three-quarters when propagated for three-quarters of a period, strengthening the correctness of the code implemented.

Another way to verify the propagation by looking at the altitude is to identify the perigee and apogee altitudes (Figure 9.7). Given that the orbit was propagated for the existing satellite, the original apogee and perigee altitudes were known. This helped verify if the propagated altitude resulted in the same apogee and perigee altitudes as those provided by literature. McKnight, 2021 defined the perigee and apogee altitudes of the Kosmos 1408 as *465* km and *490* km respectively. When the maxima and minima of the altitude graph were obtained, the values were *464.76* km and *490.24* km. Given that the McKnight, 2021 data only provided three significant figures, when rounding the data obtained from the propagation, the error would be 0.00%.

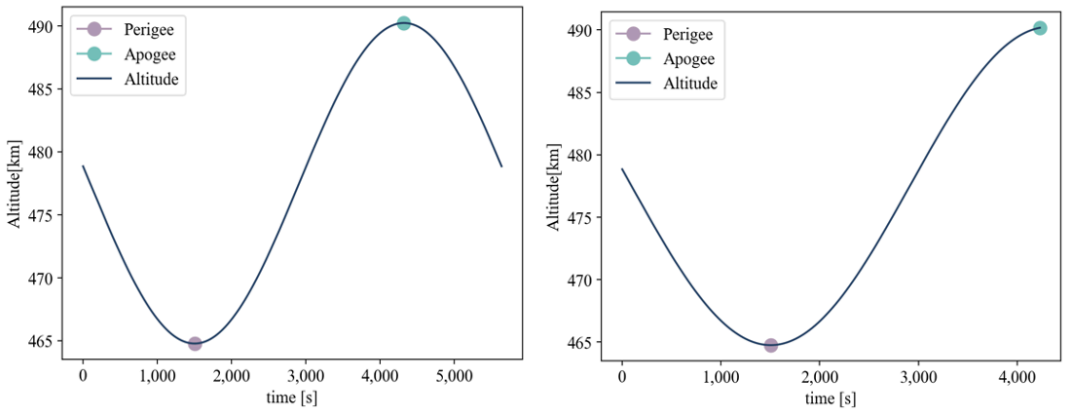

Figure 9.10: **a**. The altitude of a full Kepler orbit of the satellite (left) **b**. The altitude of three-quarters of a Kepler orbit of the satellite (right).

9.6. Interpolation

In order to obtain the best interpolator, an analysis was carried out in Chapter 7. Here the error was plotted as a function of time. It could be seen that at every time step where the position is known, the error was 0. Similarly linear interpolation resulted in the largest error, followed by quadratic interpolation and cubic spline had the smallest error. This was to be expected and served as validation and verification. Nonetheless, the results were further analyzed by using the Kepler Solver to obtain the real position and velocity of the satellite at an arbitrarily chosen time, in this case, 0.125 seconds. Then dataset containing the satellite positions was used and both quadratic and cubic interpolation was carried out to be verified. The results of this verification can be found in Table 9.3. As can be seen to the required accuracy of 1 mm the error is 0 for quadratic and cubic interpolation.

Parameter	Kepler Solver	Quadratic Interpolation	Cubic Interpolation	Error [km] Quadratic	Error [km] Cubic
x [km]	2467.281574	2467.281574	2467.281574	9.095×10^{-13}	4.547×10^{-13}
y [km]	−2295.731797	−2295.731797	−2295.731797	-1.819×10^{-11}	-1.819×10^{-12}
z [km]	−5971.909896	−5971.909896	−5971.909896	6.776×10^{-11}	3.865×10^{-12}
vx [km/s]	3.3159607	3.3159607	3.3159607	-4.405×10^{-14}	-2.442×10^{-15}
vy [km/s]	−5.82610214	−5.82610214	−5.82610214	6.239×10^{-14}	3.331×10^{-15}
vz [km/s]	3.62151529	3.62151529	3.62151529	1.599×10^{-14}	-1.776×10^{-15}

Table 9.3: Verification results for the position of the satellite for the case study of two days at a time of 0.125 seconds.

10

Results and Discussion

This chapter will be divided into sections pertaining to the category of the results. These will consist of velocity, orbital elements, orbits and simulation results. Within each of these sections there will be two sub-sections: results and discussion. The results section will report the main findings of this study in a concise and objective manner. This will be followed by a discussion of the results, in which the answer to the research question and sub questions will be provided.

10.1. Velocity

The first data that will be presented is on velocity. Figure 10.1 shows the Δv values obtained using the NASA Model. These values represent the velocity magnitude obtained after the explosion simulation. These ranged from 0.0 km/s to 1.0 km/s with a larger number of data points at the lower velocities. The distribution is a right-skewed bell shape with the majority of values at about 0.1 km/s.

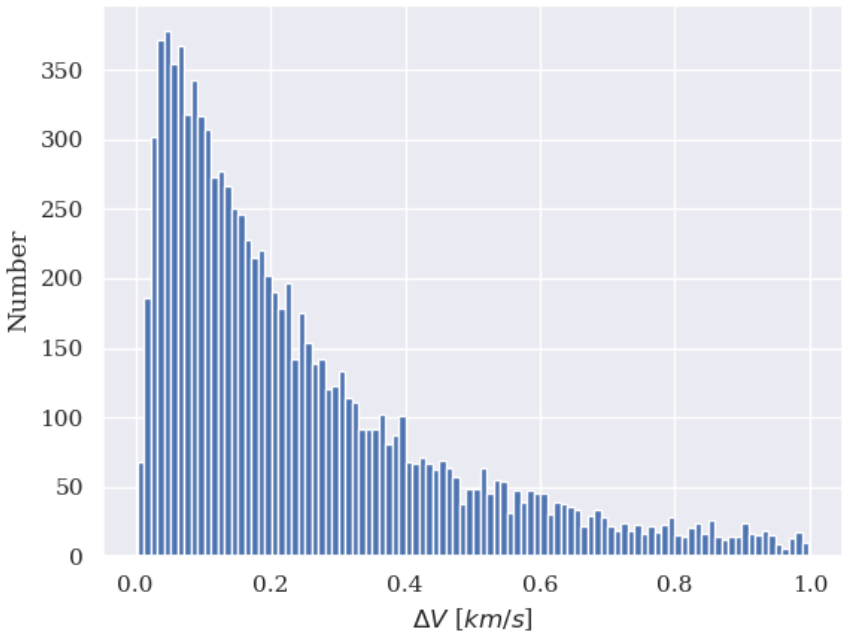

Figure 10.1: Δv distribution generated for 10,000 fragments with the NASA Breakup Model 4.0.

Once the velocities seen in Figure 10.1 were obtained, they were combined with the directional unit vectors obtained from the explosion model. The explosion was then plotted as a form of the velocity

vectors, with an origin at x = 0, y = 0, z = 0. The results of this explosion can be observed in Figures 10.2 and 10.3. It can be observed that the explosion is in all directions with lower density towards the outside. A better depiction of the fragment velocity values can be observed in Figure 10.4 where the

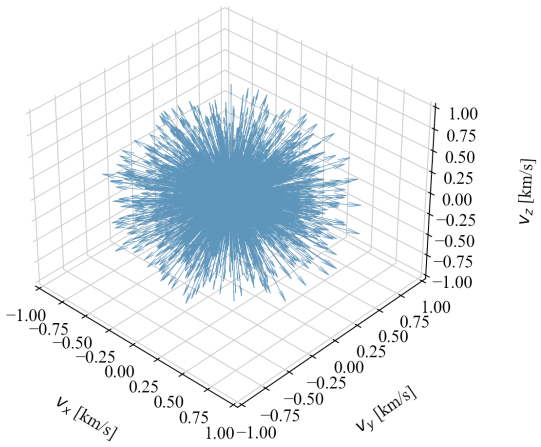

Figure 10.2: Explosion velocity vectors prior to adding original satellite velocity (3D).

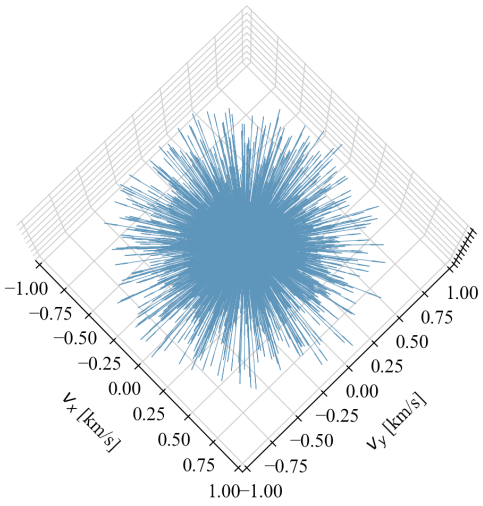

Figure 10.3: Explosion velocity vectors prior to adding original satellite velocity (top view)

velocity values were plotted as points for clarity purposes.

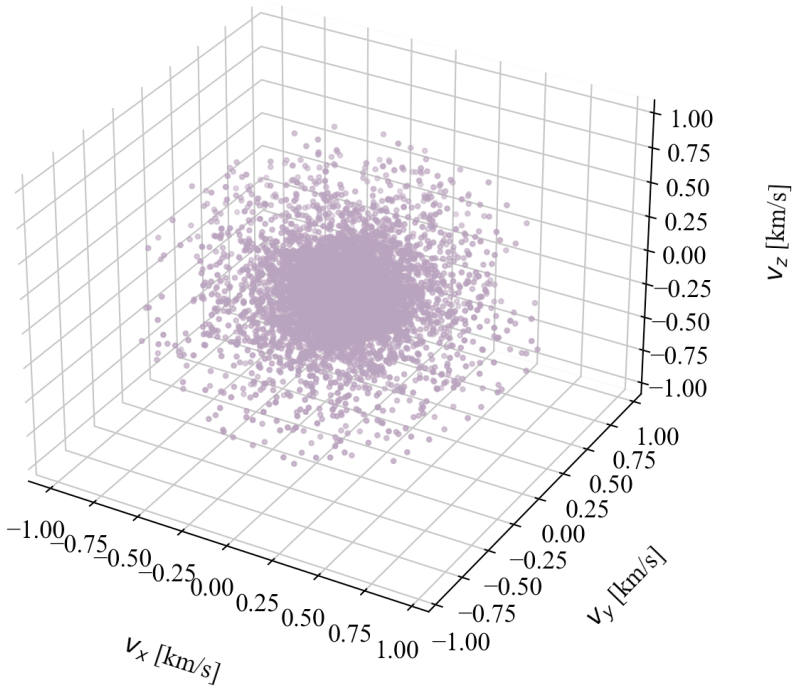

Figure 10.4: Explosion velocity depicted with a scatter plot.

Upon having included the satellite's initial velocity ([0.0786 -1.8585 7.3973] km/s) the resulting vectors can be observed in Figure 10.5. Here the vectors face in the general direction of velocity vector of the original satellite.

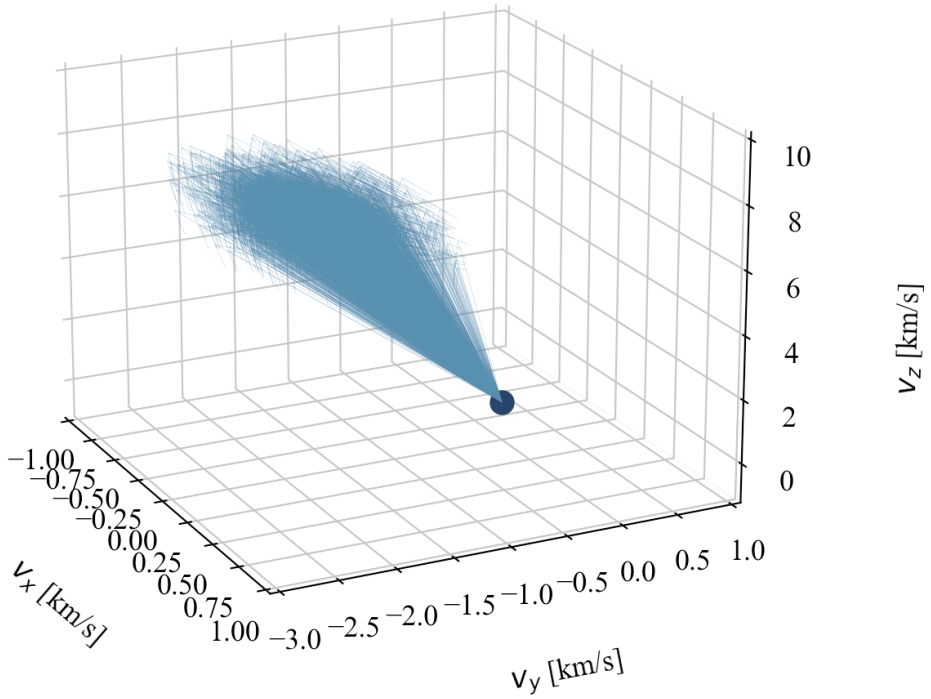

Figure 10.5: Explosion velocity vectors after to adding original satellite velocity depicted with the satellite original position at [0,0,0].

In order to get an insight into the distribution of the velocity components, they were plotted as seen in Figure 10.6. The x-component of the velocity values range from -1.00 to 1.00 km/s, the y-component values range from -3.00 to -1.00 km/s, and the z-component values range from 6.25 to 9.00 km/s. Averaging to a total velocity range of 7.00 km/s to 9.11 km/s. Overall, the diverse distributions are bell-shaped with peaks at a count of 700.

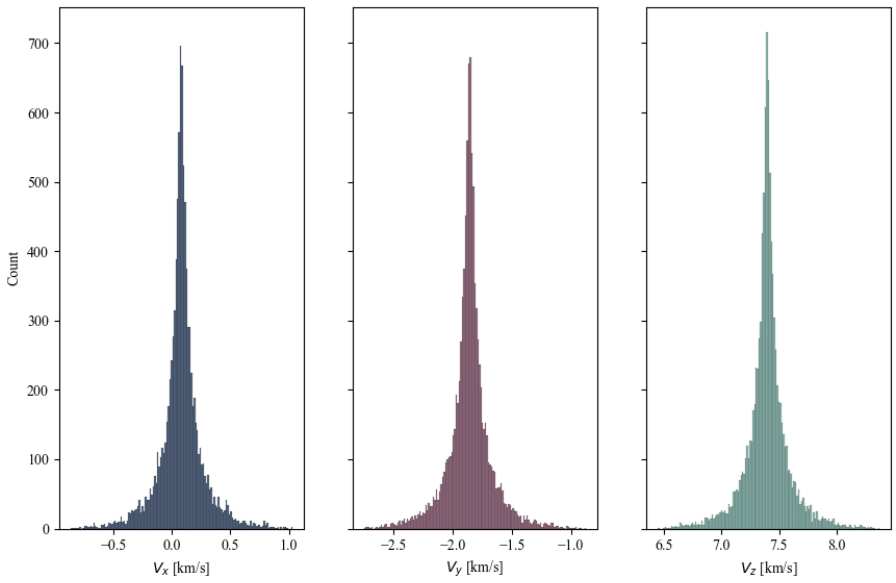

Figure 10.6: Distribution of velocity components upon adding the original velocity of the satellite.

The norm of the velocity contributions depicted in Figure 10.6 can be seen in Figure 10.7. This distribution ranges from 6.50 km/s to 9.00 km/s, it consists of a bell-shaped curve with a peak at 7.65 km/s.

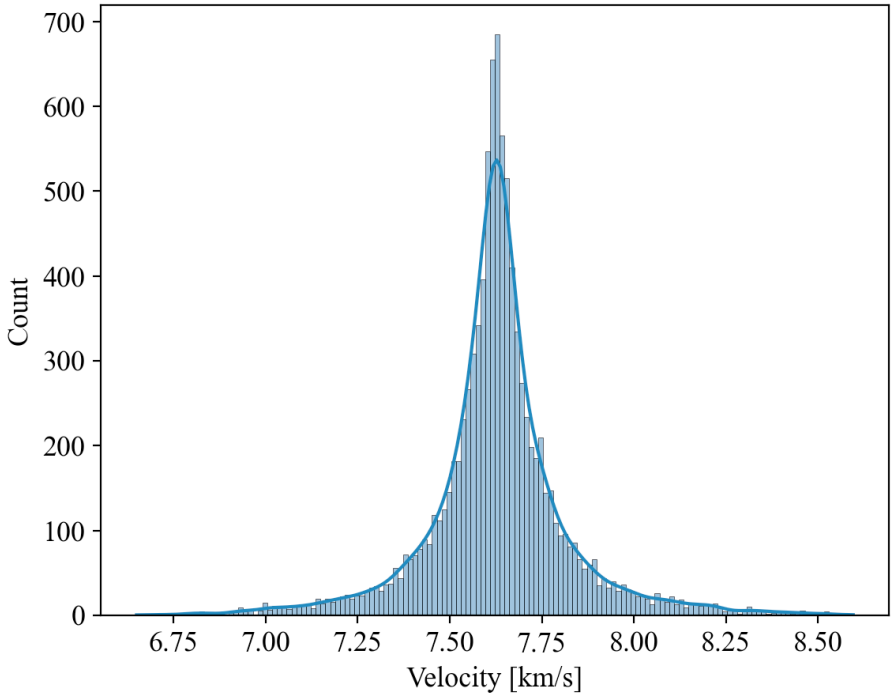

Figure 10.7: Distribution of the norm of the velocity upon adding the original velocity of the satellite.

As aforementioned, the velocity vector of the satellite right before the explosion was [0.0786 -1.8585 7.3973] km/s. Looking at the distributions in Figure 10.6, it can be noted that the peak of the distribution, where most velocities are found for the x-direction, is at around 0.1 km/s. This value is relatively close to the original satellite velocity component. A similar trend can be observed for the y and z-direction, where the y-component peak is at approximately -1.8 km/s and the z-component is at approximately 7.4 km/s, both of which are almost identical to the original satellite velocity. This can be expected, given that the distribution provided by the model has velocities that range up to 1 km/s. When combined with the unit vectors obtained from the explosion geometry, this value is distributed throughout the three components of the vectors, thus none of them equating to more than 1 km/s. A better depiction of this can be observed in Figures 10.2, 10.3, and 10.4. When looking at the x-component of the original velocity, 1 km/s is tenfold the original value, so the contribution of the distribution is larger. However, looking at the z-direction, 1 km/s is less than one-seventh of the original velocity so the contribution of the distribution is smaller, proportionally speaking. This is strengthened by Figure 10.7, where the norm of the distribution is almost identical to that in the z-direction, given that this is the direction of the trajectory. Figure 10.5 also strengthens this claim, given that once the initial velocity is added, the vectors have a bias in the direction of motion of the original satellite. None of the fragments are going in the opposite direction of the explosion, but rather fanning out in the general direction of the original velocity.
Looking at the initial vectors provided in Figure 10.5, it can be seen that even at the moment of the explosion, the direction varies a large amount and it can be expected that this will results in a large dispersion across the globe thus making it more difficult to catch the fragments.

10.2. Orbital Elements

Although the components of all the velocities were bell-shaped, the orbital elements showed diverse behaviours in their distribution. In order to compare the fragments orbits to that of the original satellite the distributions were plotted. As seen in Figure 10.8, the semi-major axis, eccentricity, inclination and right ascension of the ascending node were all bell-shaped. The semi-major axis was slightly right-

skewed, while the eccentricity is very right-skewed. The argument of periapsis, true anomaly, eccentric anomaly and mean anomaly, have multimodal distributions with three visual peaks, one in the center and one peak in each extreme. However, in reality this is two peaks as $0°$ is equivalent to $360°$.

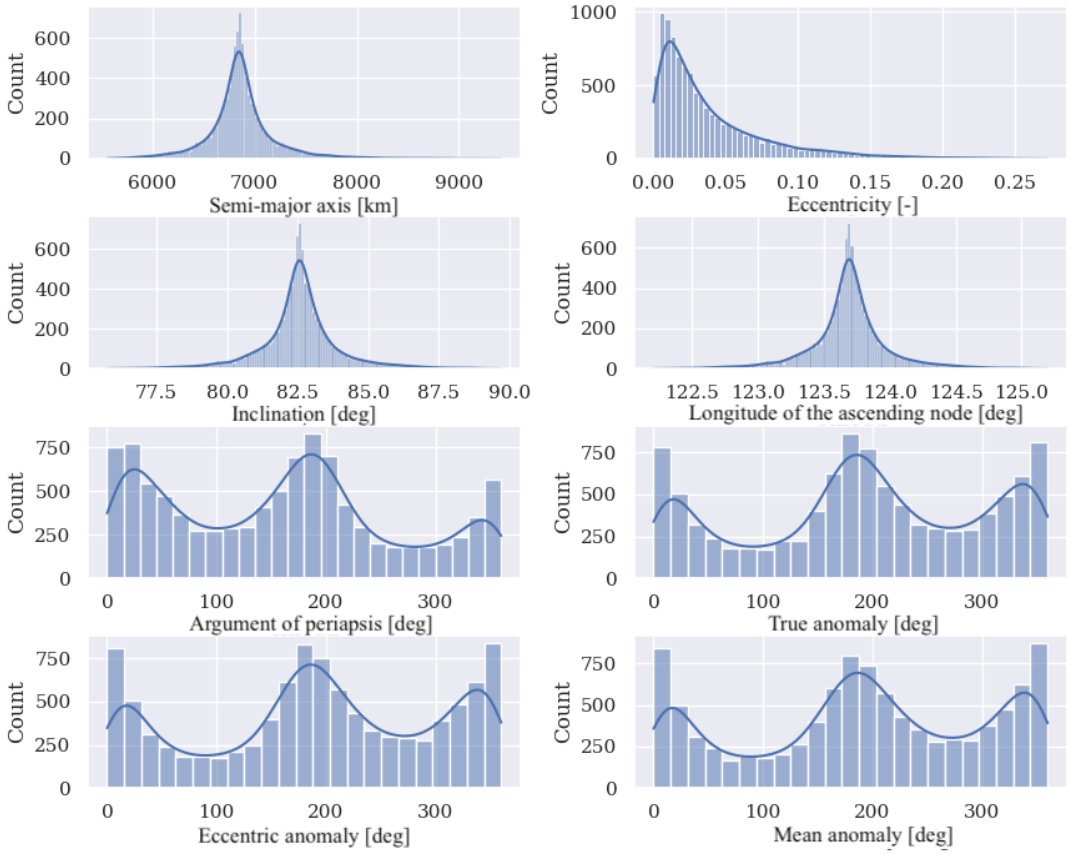

Figure 10.8: Distributions of the various orbital elements of the 10,000 generated fragments right after the explosion.

Looking at the distribution of the orbital elements, it can be observed that, as expected, the semi-major axis, eccentricity, inclination and right ascension of the ascending node all experience the peak at the values of the original satellite. The argument of periapsis, true anomaly, eccentric anomaly and mean anomaly have peaks at $0°$, $180°$ and $360°$ with $0°$ and $360°$ effectively the same. At Δv values in the direction of the orbit, where the largest component is in the z-direction, the local velocity is increased so the apogee radius is increased. Similarly, looking at a Δv in the opposite direction of the trajectory, the velocity is reduced so the perigee decreases. The perpendicular Δv vectors are not affecting the orbit as drastically. For this reason, there is a peak at $0°/360°$ and 180 degrees.

10.3. Orbits

Once the orbital elements were obtained, the orbits were propagated. In order to get a perception of the relationship between the movement of the original satellite versus that of the debris fragments, four arbitrary fragments were chosen. Figure 10.9 depicts the orbits of said fragments, along with that of the satellite and the satellite's position at the time of explosion (t = 0) and the Earth. These were propagated for one period of the satellite. It can be observed, that the orbits are all fairly close to that of the original satellite. This is strengthened by the distributions presented in Figure 10.8.

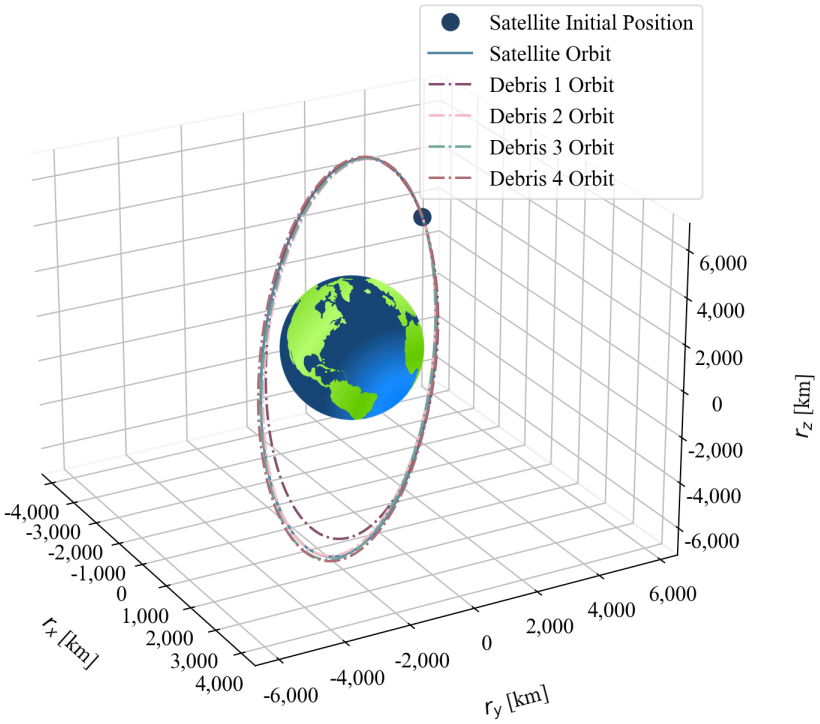

Figure 10.9: Depiction of original satellite orbit, satellite initial position and the orbits of four arbitrary fragments with respect to the Earth (size is not proportional to real size for clarity purposes).

When taking a closer look at an orientation of the orbit, as seen in Figure 10.10, it can be observed that all orbits cross the initial satellite position at one point in their orbit.

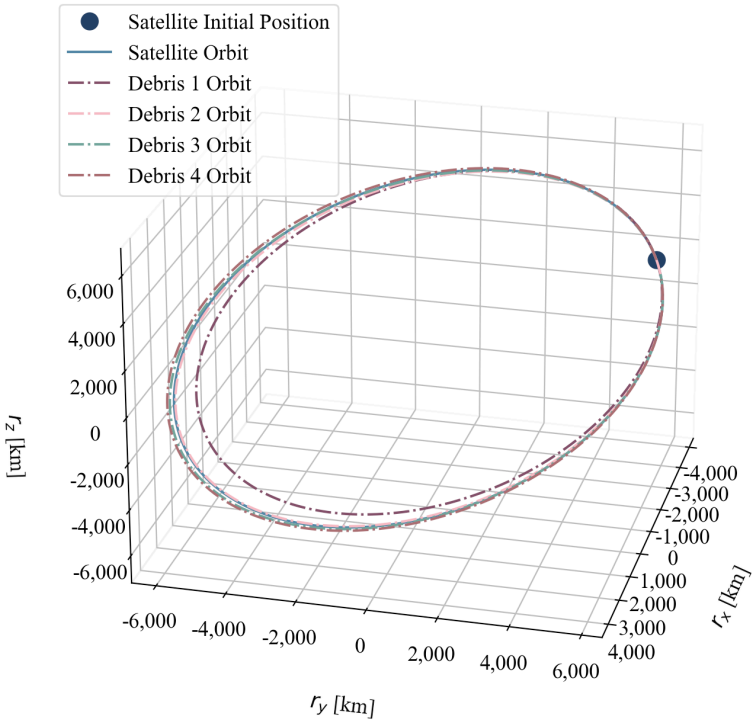

Figure 10.10: Depiction of original satellite orbit, satellite initial position and the orbits of four arbitrary fragments (perpendicular to orbit).

Similarly, looking at the altitude of the original satellite and the same four arbitrary debris fragments, Figure 10.11 shows that the altitudes vary among the debris, as well as with respect to the satellite. In some cases, the perigee altitude is even lower than the Earth's radius such as in the case of Debris 1, meaning that it would decay upon entering the Earth's atmosphere given that we are handling small fragments in this simulation. For the rest, the altitudes vary slightly, some going up to 650 km while some going to approximately 450 km.
It is important to note that in Figure 10.9 the size of the Earth is not proportional to each real size, had this been the case one could see how the orbit of Debris 1 would fall inside the Earth. Nonetheless, for clarity purpose of reading the plot the Earth was only included to get an idea of the relative movements.

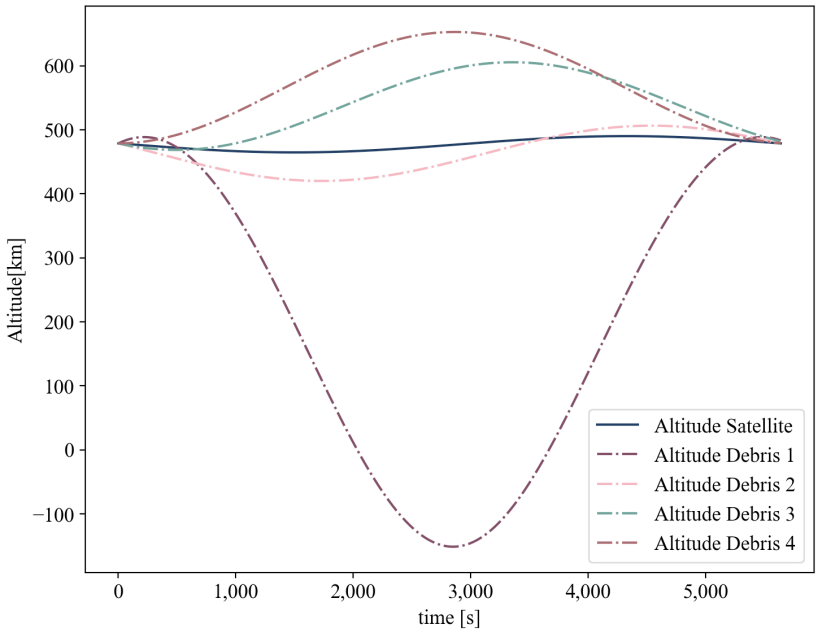

Figure 10.11: Depiction of satellite altitude and the altitude of four arbitrary fragments.

In terms of the behavior seen in Figures 10.9 and 10.11 the results are as expected, given that as a result of the explosion, the fragments are dispersed in all directions. However, once the satellite velocity is added, all of the resulting vectors point in the direction of the satellite. Nonetheless, the fragments have largely varying perigees and apogees. Given that the orbits simulated are Keplerian, they will all cross the initial explosion point during one point of their orbit. This could potentially be used to catch more fragments. Even though the velocity gained from the explosion model, is small relative to the initial velocity, it can be observed that a disturbance such as an explosion, causes a large variation in certain aspects the astrodynamical behavior of the fragments generated while others remain close to the original values of the satellite as seen in the orbital element distribution in Figure 10.8 and also evident in the orbit depictions in Figures 10.9 and 10.10.

10.4. Simulation Results

Once the simulations were completed for the eight case studies mentioned in Chapter 8 Table 8.1, the findings were summarized in a table. The results express the closest relative distance achieved by each individual fragment, with respect to the catcher satellite. These were then grouped, depending on the radius of the catcher spacecraft. The smallest radius considered was 1 m while the largest was 100 m. The results of the caught fragments can be observed in Table 10.1. The results presented are cumulative, meaning that the 100-m radius number for fragments caught includes all those caught with all the smaller radii.
It can be seen, that the general trend is that the number of fragments decreases as the time of deployment is delayed. However, for a 20-m radius, the trend varies, given that the 12-hour case study shows the highest number of fragments caught. Similarly, the 6-hour case study shows a higher number frag-

ments caught with a spacecraft of 50-m and 100-m radii. The case studies with injection inaccuracies result in no fragments caught for a spacecraft of a 20-m radius and below.

	Catching Radius					
Case Study	**1 m**	**5 m**	**10 m**	**20 m**	**50 m**	**100 m**
10 s	25	92	171	321	720	1203
3 h	15	79	151	277	723	1226
6 h	16	70	139	278	681	1251
12 h	12	64	140	288	646	1168
1 day	15	60	116	247	611	1104
2 days	11	53	103	212	486	1040
12 h + 0.1 deg incl	0	0	0	0	2	33
12 h + 10 km alt	0	0	0	0	0	8

Table 10.1: Results of cumulative fragments caught depending on catching radius and deployment time.

To get a better perspective of how many fragments could be gained by increasing the radius of the catcher spacecraft, the unique values were calculated and are presented in Table 10.2. It can be observed that the unique case studies show a different trend. For example, for a deployment delay of 2 days, when the radius is increased to 100 m, a larger number of fragments is caught than for the case studies of 1 day, 12 hours and 3 hours. Similarly, the 1-day case study shows a higher number of fragments retrieved when using a 50-m radius spacecraft than the 12-hour case study. Looking at the 20-m case study, the 12-hour case study shows a higher number of fragments gained than all case studies with the exception of 10 seconds.

	Catching Radius					
Case Study	**1 m**	**5 m**	**10 m**	**20 m**	**50 m**	**100 m**
10 s	25	67	79	150	399	483
3 h	15	64	72	126	446	503
6 h	16	54	69	139	403	570
12 h	12	52	76	148	358	522
1 day	15	45	56	131	364	493
2 days	11	42	50	109	274	554
12 h + 0.1 deg incl	0	0	0	0	2	31
12 h + 10 km alt	0	0	0	0	0	8

Table 10.2: Results of unique fragments caught depending on catching radius and deployment time.

In order to visualize the change incurred by the increase in spacecraft radius, as well as the change experienced with the different case studies, the number of fragments caught is plotted as seen in Figure 10.12. Note that the 100-m radius was omitted, in order to have a better view of the trend and not obscure the smaller data. The x-axis shows the spacecraft radii, while the y-axis along with the bubble size shows the number of cumulative fragments caught. One can see the scale representing the bubble size is generated proportional to the diameter. It can be recognized, that as the spacecraft radius increases, so does the number of fragments caught. The general trend shows that earlier deployment times result in more fragments caught. Another observation is, that the increase appears linear for an increasing radius.

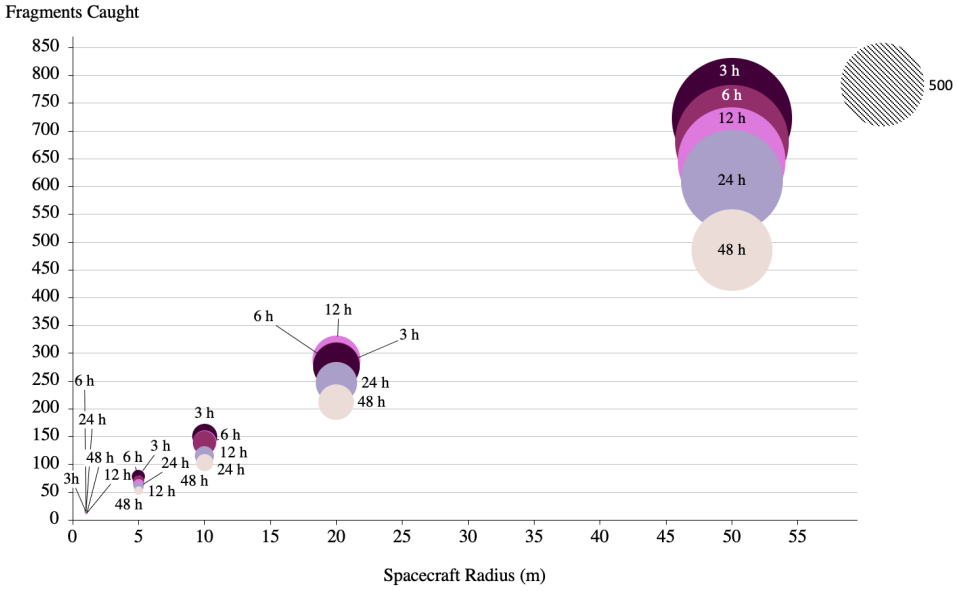

Figure 10.12: Bubble chart depicting the number of fragments caught as a function of space radius with the bubble diameter representing the number of fragments caught.

The first thing to consider when analyzing the overall results in Tables 10.1 and 10.2, is the improvement from the initial calculations carried out in Chapter 5. In said calculations (Equation 5.29), the number of fragments caught, was calculated to be 18.31 particles per week. Nonetheless, it can be seen, that with the same conditions as those mentioned in the preliminary calculations the number of fragments caught equates to a maximum number of 288 fragments caught (Table 10.1) The 10-second case study served as a proof of concept, but will not be considered a realistic option. This is an extraordinary improvement on the preliminary numbers in Chapter 5, given that there is an additional 270 fragments caught.

It was mentioned, that the general trend is for the fragments caught to increase as the radius increases, and the fragments caught to decrease, as the spacecraft is deployed later in time. Nonetheless, it was noted that there are some outlying cases. This can be associated with the statistical nature of the problem. It can be the case, that when deploying six hours later, one simply encounters more fragments. Although the orbits of the fragments intersect with that of the original satellite, they need to be at the same place in the orbit at the same exact time. Given that the influential factor is the time, it is possible that when deployed after six hours, the geometry of the fragments with respect to the satellite, is more favorable for encounters with the fragments. This is observed in the results. On another hand, the simulation does not take perturbations into consideration, the fragments spread out over the planet at a slower rate, so in this case, an increase is shown when deployed six hours after versus three hours after. Nevertheless, in a case where perturbations had been taken into consideration, the J_2 effect would influence the right ascension of the ascending node and the argument of perigee, thus making the debris spread out over the globe faster (Wakker, 2015). It is also important to note, that using a 100-m radius spacecraft, depending on the time of deployment, 11.68 % to 12.51 % of the original fragments are caught. Nonetheless, a spacecraft that large is not realistic, at the current moment in time, in terms of advances in satellite sizes. When looking at a more realistic, yet still large size, such as 20 meters, that percentage drops drastically to a maximum of 2.88 %, in other words, a decrease of almost 1,000 fragments less caught. This puts the feasibility of this passive technique into question. Looking at the cases with injection inaccuracies, it can be seen, that if this technique were to be used, accuracy would be absolute key. This can be attributed to the fact, that a slight deviation in both in altitude or inclination, results in the number of fragments caught, to drop to 0 for most spacecraft radii. Although the inaccuracy in inclination results in slightly better results than the altitude inaccuracy, this result is still unacceptable.

The next goal was to see the effect of the various case studies on the distribution of the relative distance

when caught. The results were depicted in a set of box and whisker plots (Figure 10.13).

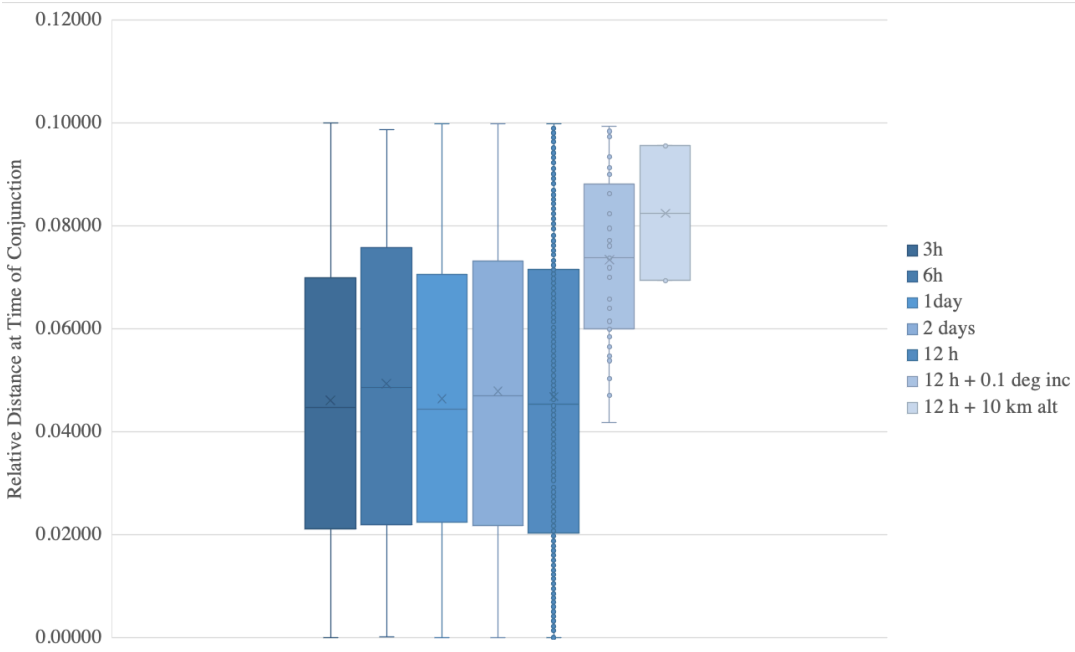

Figure 10.13: Box and whiskers plots for each case study representing the relative distance when caught.

It can be noted, that the maxima and minima are 0.1 for almost all case studies except when deployed 6 hours after the explosion time and when deployed 12 h after with a 10 km injection accuracy in altitude. For all case studies without injection inaccuracies, the minimum distance is 0.000 km whereas those with inaccuracies experienced larger minimum distances. These are slightly above 0.400 km for the inclination inaccuracy, while its approximately 0.070 km for the altitude inaccuracy. For all cases without injection inaccuracies, the mean is slightly above the median and ranges from 0.046 km to 0.049 km. Contrarily, the mean for the inclination inaccuracy is below the median while for the altitude inaccuracy it is equal to the median. The first quartile is lowest for the 3-hour case followed by the 1-day case and the 12-hour case. The cases with the injection inaccuracies have the highest quartiles, with the altitude inaccuracy resulting in a higher value for the first quartile. The third quartile, on the other hand, is lowest for the 12-hour case, followed by the 3-hour and 6-hour cases. The highest third quartile is experienced by the cases with injection inaccuracies.

When taking a closer look at the distribution depicted by the box and whisker plots, in Figure 10.13, it can be observed that for cases with injection inaccuracies, the relative distance at the time caught, is significantly higher than for the cases without inaccuracies. The distributions of the remaining case studies come to show that the relative distance when caught is not largely dependent on the time of deployment. All cases have similar distributions, the inconsistencies can be attributed to the statistical nature mentioned before.

Another factor that was looked at, was the error incurred by the minimum distance calculation. Namely, the difference between the relative distance obtained using the minimum distance formulas presented in previous sections, versus the relative distance obtained with the Kepler solver. The results were plotted as a function of the time difference incurred from the initial position up to the minimum distance. The outcome of said analysis can be seen in Figure 10.14. It can be seen, that as dt (the difference between the time of the simulation and the new time obtained with the minimum distance) increases, the minimum distance error increases. The maximum error incurred for the case presented is approximately 0.090, while the minimum error is 0.000. The low error region has a higher density than the higher error region.

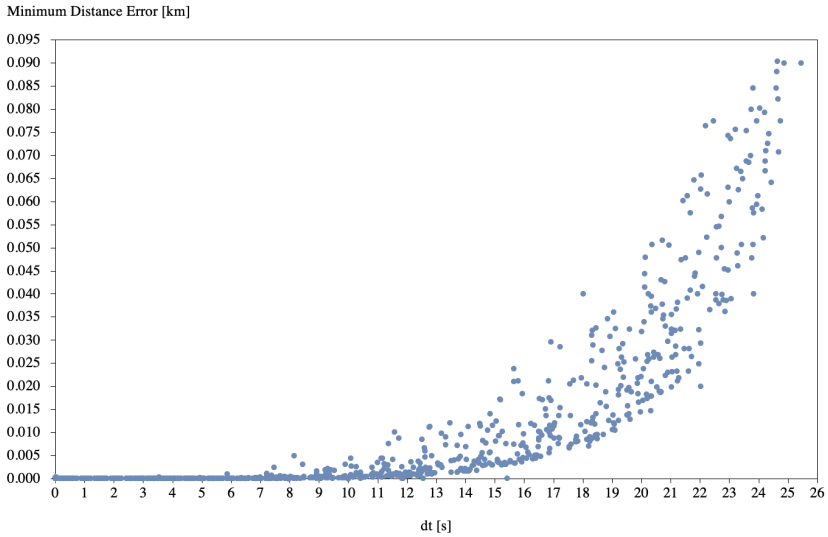

Figure 10.14: Error incurred using the minimum distance formula as a result of the time taken from the initial position to the final position.

When looking at the error results, a key factor mentioned by Alarcón Rodríguez et al., 2002 in their paper, is the use of small step sizes for the minimum distance calculations. This can be attributed to the fact that the orbit is circular so when using large step sizes, larger errors are incurred. This study accounted for this, by propagating the real position and velocity at the time when the linearized minimum distance was incurred. However, the error was still taken into account, to see the success of this technique, were it to be used in further studies. As expected, the error between the linearized distance and the real distance increased with larger time steps. The maximum error incurred for the case at hand, was approximately 0.09 km, this is a large error when looking at something like catching space debris, since the accuracy of proximity is key. However, up to 10 seconds, the error obtained is close to 0.000 km. This means that depending on the application and the accuracy required, if the time step were to be lower than 10 seconds, it would be acceptable to not propagate the real position since it is most likely identical for most cases.

In order to see when the fragments were caught, early in the simulation or later, the relative distance versus the time at which it was caught throughout the seven-day simulation, was plotted. Figure 10.15 shows that at the beginning of the simulation a smaller number of fragments is caught. However, from approximately 75,000 seconds onwards the plot becomes dense signifying more fragments caught.

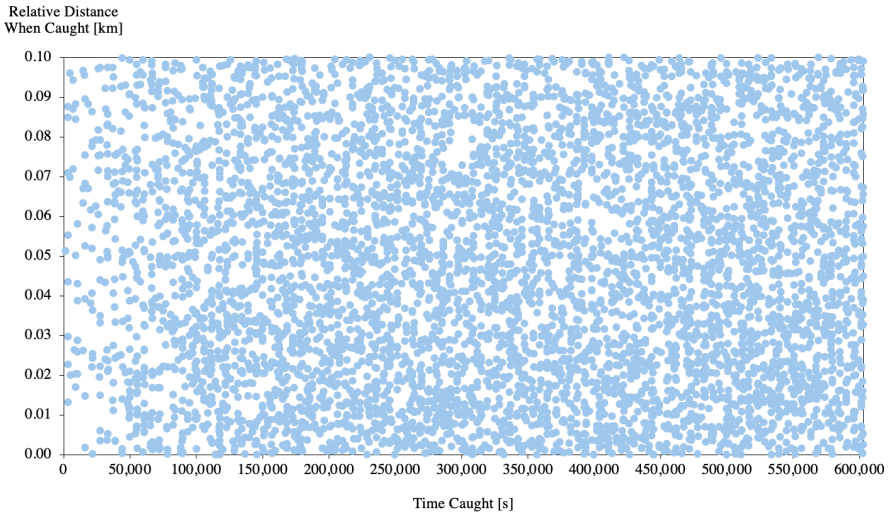

Figure 10.15: Relative distance of the fragments when caught as a function of the time when they were caught.

A similar overview of the fragments caught over time is presented in Figure 10.16. Here, the number of fragments caught is presented as a cumulative number, based on the day caught. As aforementioned, on the first day, there is a lower number of fragments caught, this gradually increases between the second and third day, then decreases again for days three to five and increases again from day five to six.

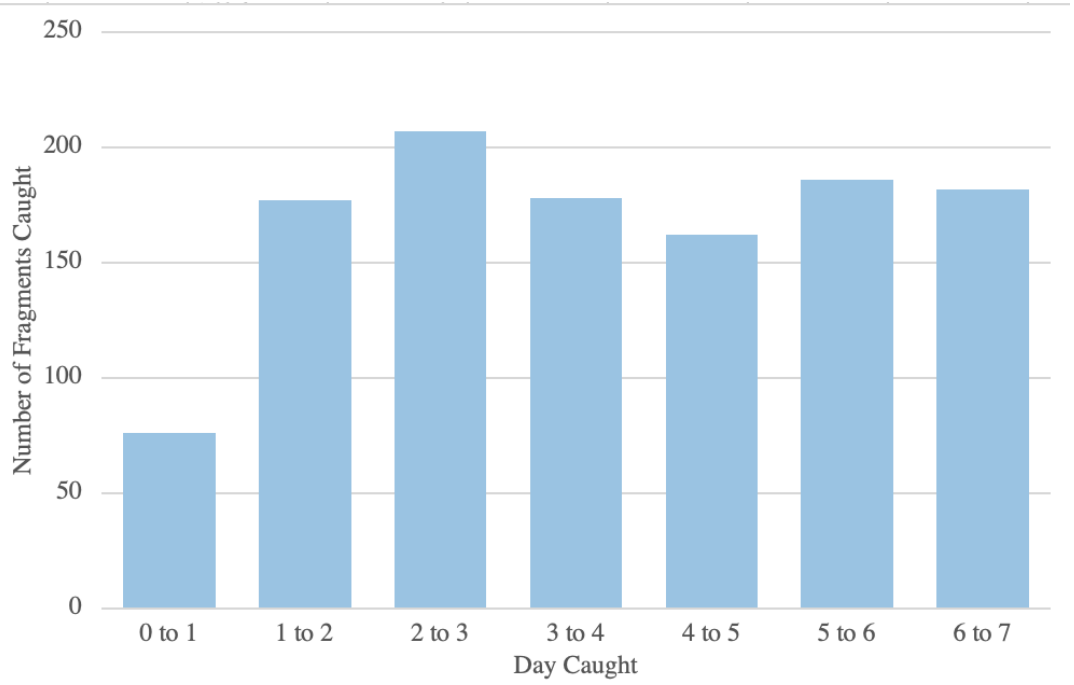

Figure 10.16: Number of fragments caught per day for the duration of one week.

All in all, both Figures 10.15 and 10.16 show an initially low number of fragments caught. This could be attributed to the positioning of the spacecraft. Given that the point of deployment follows the orbit of the original spacecraft in opposite direction and the simulation starts by obtaining the position of the fragments after a certain number of hours or days. When the spacecraft is input into an orbit, it is expected that it finds itself in the middle of the debris cloud, going in the opposite direction of the debris. However, when encountering the same situation, it will pass the forefront of the debris cloud, so setting the spacecraft at an offset before would not influence the number caught, but rather the time when caught. Furthermore, it can be observed, that by the end of the week, the fragments caught do not decrease as would be expected. In the case at hand, this means that one would likely benefit from having a mission spanning for a longer time and not just a week. On the other hand, as was mentioned before, the J_2 perturbation would result in the plot at hand looking very different, and the number of fragments caught would be dying off towards the end, given its effect on Ω and ω (Wakker, 2015).

Taking a closer look at Figure 10.16, the findings mentioned above are strengthened, when on the first day the number of fragments caught is below 100, in comparison to the second day, where it is around 175. Looking at the general trend, it can be recognized, that it is somewhat periodic, the number of fragments peaks every three days. However, given that the simulation time is only 7 days, the remainder of this behavior is uncertain.

Next, the more mechanical aspect of the fragments was analyzed by looking at the momentum. Figure 10.17 shows that more than half of the fragments have a relatively small momentum close to 0.01 kg m/s. However, there are some fragments that have a momentum between 50 and 200 kg m/s. whilst three fragments have momentum values of up to 526 kg m/s. Given that most fragments are smaller than 1 cm, and thus the density considered is that of aluminium (Johnson et al., 2001), the leading parameter is the size as well as the velocity. A zoomed-in version of the momentum can be seen in Figure 10.18. Here, one can see that a large number of fragments accumulates at smaller momentum

values.

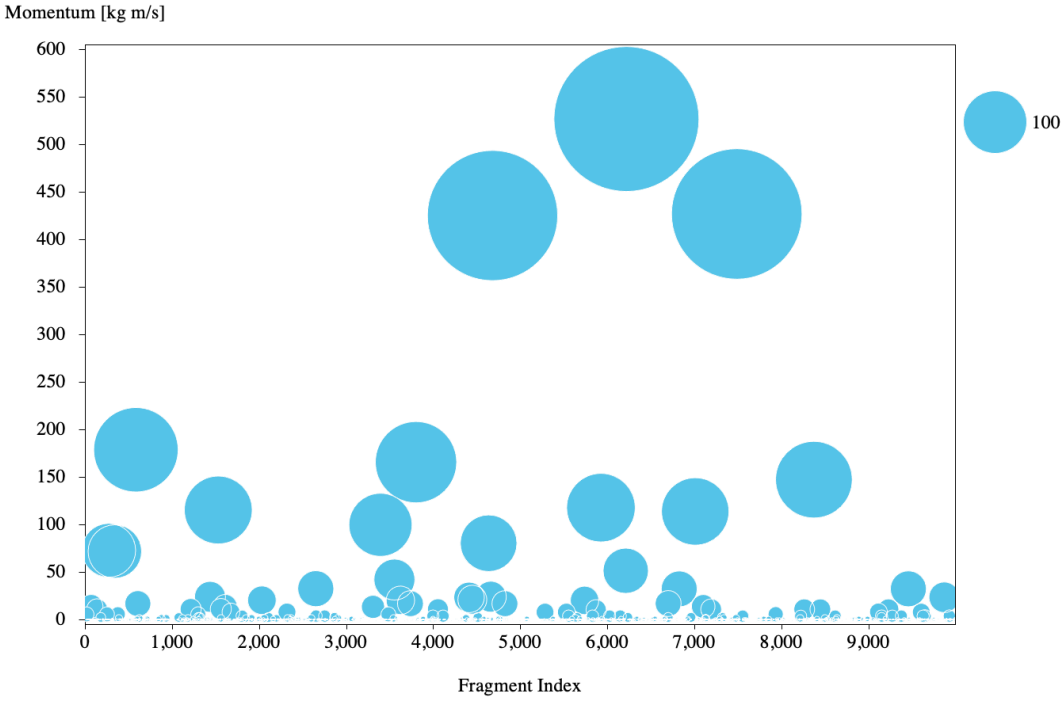

Figure 10.17: Momentum of the fragments caught depicted with the fragment and bubble size diameter representing the momentum for the 6-hour case study.

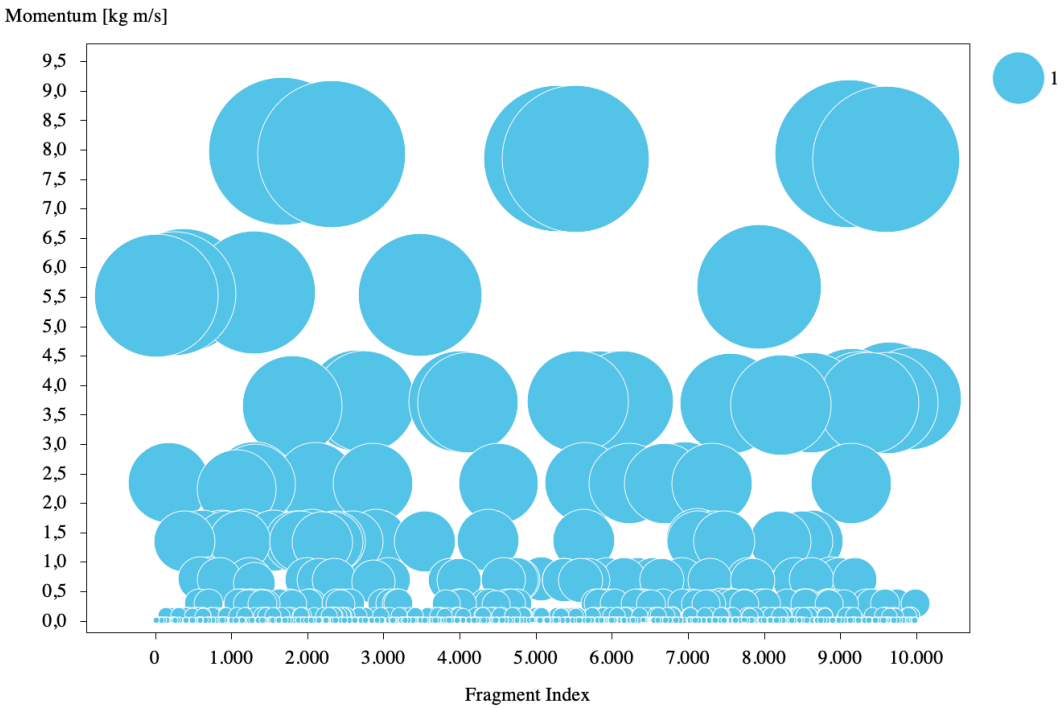

Figure 10.18: Zoomed version of the momentum of the fragments caught depicted with the fragment and bubble size diameter representing the momentum for the 6-hour case study.

The momentum was obtained based on the mass of the fragments and the velocity. It was noted, that most fragments are found at lower momentum values, while some fragments had incredibly high mo-

mentum values. This pertains to the fact that as a debris mitigation method the catcher satellite should not generate further debris. Although this was not the scope of this study, it is important to take into consideration, that in a possible design of this method, although the majority of the momentum is found at low values, the design has to account for the higher values in order to not result in a breakup when encountering said larger fragments. This puts the difficulty of debris removal into perspective, given that one has to plan for a worst-case scenario no matter the probability of encounter. If precautions are not taken and the spacecraft is not designed for the largest momentum value the results could be catastrophic and worsen the environment.

Another analysis that was carried out, was the comparison of the fragment indices caught (not depicted), to examine if all case studies resulted in the same fragments caught; or if deploying at different times resulted in different fragments being caught. From this analysis, it was concluded, that all case studies resulted in 3,227 unique fragments being caught for a spacecraft of a 100-m radius. Looking at the cumulative unique number of fragments caught (Table 10.1), it was observed that for the largest spacecraft radius 32% of the overall fragments were caught for all case studies. This strengthens the claim that the problem is of a statistical nature. The different deployment times result in different parts of the debris cloud being encountered. This implies that if the method were to be left in space for a longer period more fragments would be caught.

The next analysis carried out, was the distribution of the relative distance on the spacecraft surface. To do this, the relative distance when caught was plotted in x, y and z LVLH coordinates. The results of this can be seen in Figure 10.19. It can be observed, that the fragments all align on the same plane, namely the surface of the spacecraft upon contact (z = 0). Moreover, it can be seen, that most debris fragments are caught at the center of the surface. It is important to note, that only fragments caught within a 20-meter distance were plotted.

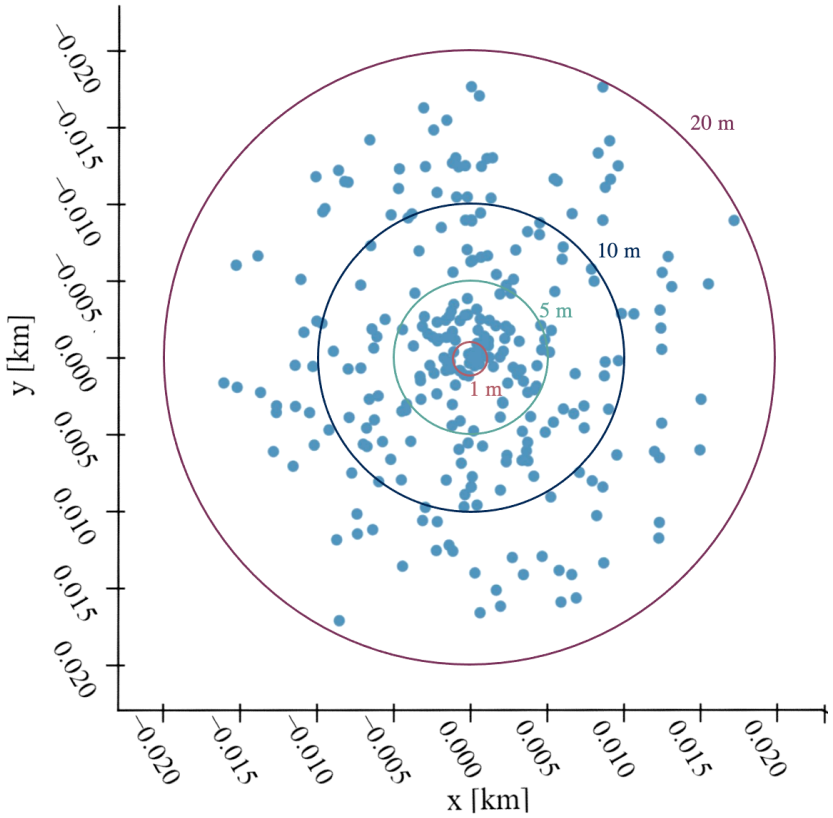

Figure 10.19: Three-dimensional depiction of the relative distance of the fragments when caught for the 3 hour case study.

Looking at the positioning on the surface of the spacecraft when caught, seen in Figure 10.19. The agglomeration of fragments at the center of the sphere can be attributed to the fact that at the center

of the circular surface of the spacecraft would be directly in the initial orbit, this part experiences most fragments caught. However, there is still a large number of fragments which are caught on the outer ends of the spacecraft. This implies, that one would benefit from a larger spacecraft, which we already saw from the results provided in Tables 10.1 and 10.2. Nonetheless, it has to be recognized that impacts on the outer edge of the spacecraft correspond to an instantaneous torque and hence would lead to a rotation of the vehicle which would be crucial for a design of such a concept, however this is outside the scope of this study and will not be further explored.
Another interesting fact which was looked at, was the relative positions of both the spacecraft and the fragments when caught, with respect to the center of the Earth. Moreover, the position of the explosion of the original satellite was plotted in the form of a purple cross. The results of this can be seen in Figure 10.20. It can be seen, that the majority of the fragments encounter the spacecraft at a similar position, as opposed to spread throughout the orbit. This position is relatively close to the position of the explosion of the original satellite.

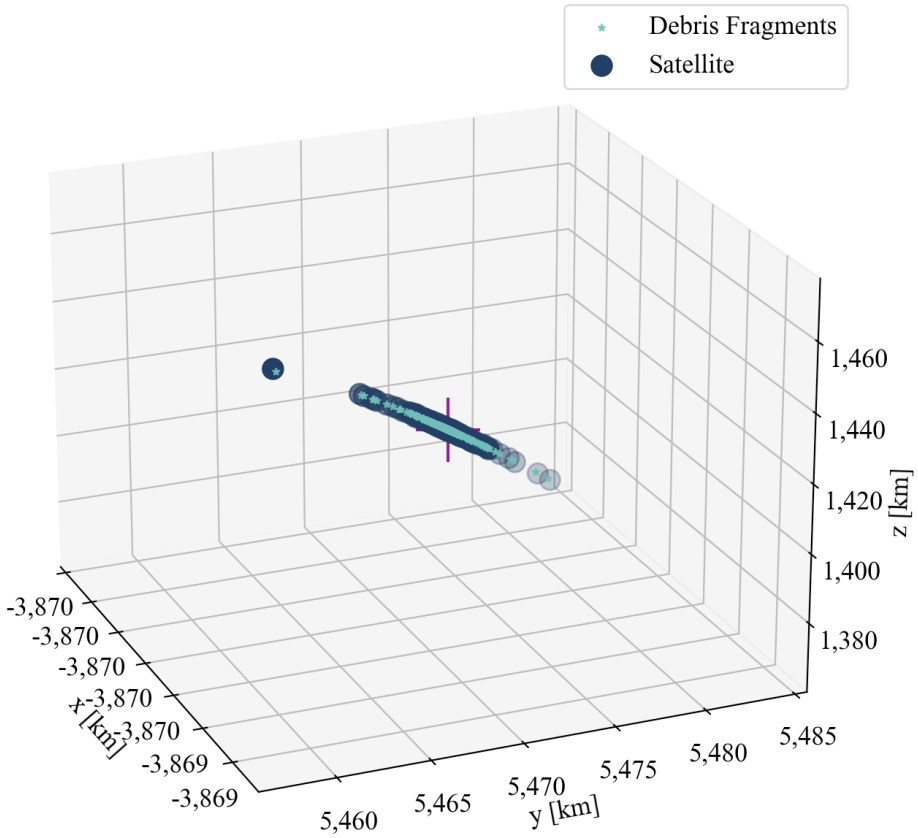

Figure 10.20: Three-dimensional depiction of the absolute distance of the spacecraft and the fragments when caught for the 3 hour case study with the position of the original explosion market by a purple cross.

Moreover, when the results presented in Figure 10.20 were analyzed, it was seen that as expected most particles are caught in the same part of the orbit. This can be attributed to some of the factors mentioned before, namely that the fragments will all cross the position of the initial explosion at one point in their orbit. This is the point where most are caught as seen in Figure 10.20. Not many fragments are caught outside of this part of the orbit. Moreover, if one looks carefully, the relative distance between the spacecraft and the fragments on the position on orbit further away from the initial explosion is larger. This can be attributed to the fact, that the closest point of the two orbits is at the explosion location and from there onwards the orbits start deviating.

11

Conclusions and Recommendations

11.1. Conclusions

The goal of this report was to study the effectiveness of a passive debris removal method to tackle space debris fragments of 10 cm and smaller in a conjunction analysis. As a means to do this a set of sub questions mentioned in Chapter 1 were researched. These will be answered throughout this chapter.

The initial part of the study sought out to find the best concept for such a mission and thus answer the first sub question. It was found that a possible concept for this study would look like a removal method consisting of a circular, flat surface made out of a material capable of catching and stopping the debris, such as possibly aerogel or foam, which flies through space catching the fragments it encounters.

In contemplation of the most favorable orbital setting for the removal method chosen for this research, a study carried out on the space debris environment and situation validated the focus on an explosion event. The case study used to obtain the results of this study was that of the Kosmos 1408 anti-satellite missile test which took place in November 2021. Upon having studied a variety of literature it was found that the NASA Break-up model 4.0 was the proper model to tackle the problem at hand. The study focused on generating a simulation of the break-up event and looking at how many fragments could be caught for a population of 10,000 fragments over a span of 7 days.

The methodology of the data generation and the simulation was explained in extensive detail along with difficulties that CPU time posed on the simulation resulting in the exclusion of perturbations. The minimum passing distance between the spacecraft and the debris was chosen to be 20 m, this aided in setting a limit while leaving the possibility to determine the effective size of such a method by exploring a variety of radii for the catcher spacecraft. The results yielded the best size as the largest size possible, in this case, a spacecraft of a 100-m radius proved to be the most effective.

The next part sought to answer the sub question pertaining to the ideal time of deployment. The results show that deployment time has a small effect on the number of fragments caught, but this could be disputed through the input of the J_2 perturbation. Nonetheless, with the conditions given, it was found that deploying after 6 hours is best for the configuration at hand. Furthermore, it was concluded that for the different deployment times the fragments caught were different ones, namely all case studies resulted in 33% of the fragments being caught. This would mean that multiple deployments with different deployment times would result in a large number of fragments caught.

Similarly, it was seen that over time the number of fragments caught did not decrease, although this too could be disputed through the input of the J_2 perturbation, this would mean that a longer mission would bring about beneficial results in terms of number of fragments caught.

An important sub question which assisted in answering the main research question, was pertaining to

the yield of the system. It was found that for a population of 10,000 fragments, the yield for the largest spacecraft of 100 m, ranges between 11.68 % to 12.51 % of fragments caught, depending on deployment time.

The next factor which was looked at was that of the effect of possible injection accuracies to establish the success of such a method in a non-perfect situation. The results obtained from the study showed that this method would be unsuccessful in the case of injection inaccuracies. It was found that inaccuracies in altitude have a larger effect than that in inclination but in both cases less than 1% of the fragments would be caught with the largest catching radius and 0 fragments would be caught with a catching radius of 20 m or smaller. Meaning that given any sort of injection inaccuracies the number of objects caught would decrease by 99%.

Exploring the mechanical aspects provided the necessary support to determine the possible momentum values encountered by such a method. Upon analyzing the results it was concluded that, while the overall sizes and thus momenta of the fragments are generally small, the possibility of one or two fragments with a large momentum is existent. The momentum values found ranged from a minimum of 0.01 kg m/s to a maximum of 526 kg m/s. This would complicate the mechanical design of the method at hand.

The overall conclusion of this study was that a method such as this one would not be considered very effective at the current time in mitigating space debris smaller than 10 cm. This was concluded based on the fact that the promising percentages are dependent on the currently unrealistic sizes of a spacecraft. A more realistic spacecraft of 20 m, would only result in a capture percentage of 2 % to 3 %. Given the cost of space missions, this would not be a feasible number. On the other hand, one can also observe the mechanical limitations as an added point towards the possible ineffectiveness of this method. While most fragments had small momentum values, others showed drastically large values. This means that in order to not generate new space debris, the larger fragments would have to be considered as the design parameters which could pose design issues.

11.2. Recommendations

Although the conclusion of this study resulted in an unfeasible method one important observation was the fragments caught further in time. Were this to be true it could result in a feasible method. However, in order for this claim to be strengthened, perturbations such as the J_2 perturbation, in particular, would have to be included. If upon adding the perturbation one were to observe a number of fragments being caught further in time, the next recommendation would be to increase the simulation time to a longer period than one week.

Another recommendation would be to further study the statistical behavior of the fragments. It was clearly observed that later deployment times can result in better results which means that if the statistics were further analyzed one could optimize the problem such that the case for the largest number of fragments are found. It would be similar to this study, but starting from a different perspective, and designing the problem based on the statistics as opposed to how it was done here.

A

Coordinate Transformations

A.1. Cartesian Coordinates to Kepler Elements

In order to successfully convert from Cartesian coordinates to Kepler Elements the inertial reference frame vectors are defined as seen in Equations A.1, A.2 and A.3 (Rao, 2021).

$$\vec{I_x} = \begin{bmatrix} 1 \\ 0 \\ 0 \end{bmatrix} \tag{A.1}$$

$$\vec{I_y} = \begin{bmatrix} 0 \\ 1 \\ 0 \end{bmatrix} \tag{A.2}$$

$$\vec{I_z} = \begin{bmatrix} 0 \\ 0 \\ 1 \end{bmatrix} \tag{A.3}$$

First the norm of the position and velocity will be calculated as shown in Equations A.4 and A.5.

$$r = |\vec{r}| \tag{A.4}$$

$$v = |\vec{v}| \tag{A.5}$$

Next the angular momentum vector (km^2/s) is calculated using Equation A.6 (Rao, 2021).

$$\vec{h} = \vec{r} \times \vec{v} \tag{A.6}$$

Similarly the norm of the angular momentum is obtained as seen in Equation A.7

$$h = |\vec{h}| \tag{A.7}$$

Using the obtained variables one has all the necessary values in order to obtain the first Kepler element, namely the semi-major axis, computed with Equation A.8 (Wakker, 2015). Given the planet this study deals with is the Earth μ corresponds to a value of 398,600.441 km^3/s^2 (Wakker, 2015).

$$a = \frac{1}{\frac{2}{r} - \frac{v^2}{\mu}} \tag{A.8}$$

The next Kepler element, the eccentricity, can also be calculated with the aforementioned variables as seen in Equation A.9 (Wakker, 2015). Given the planet this study deals with is the Earth this corresponds to a value of 398,600.441 km^3/s^2 (Wakker, 2015).

$$\vec{e} = \frac{\vec{v} \times \vec{h}}{\mu} - \frac{\vec{r}}{r} \tag{A.9}$$

where the value of the eccentricity is obtained by computing the norm of the eccentricity vector as seen in Equation A.10 (Wakker, 2015).

$$e = |\vec{e}| \tag{A.10}$$

The next Kepler element calculated is the inclination *i*, to do this Equation A.11 is used (Wakker, 2015). As seen in Figure 5.4 the inclination is the angle between the Inertial reference vector in the z direction I_z and the angular momentum vector or, in other words, the z component of the angular momentum and the angular momentum vector.

$$i = cos^{-1}\left(\frac{h_z}{h}\right) \tag{A.11}$$

In order to be able to calculate the remaining orbital elements, Ω, ω and θ the line of nodes $\vec{n}$ needs to be calculated . This is done using Equation A.12 (Rao, 2021).

$$\vec{n} = \frac{\vec{I_z} \times \vec{h}}{|\vec{I_z} \times \vec{h}|} \tag{A.12}$$

The line of nodes is then used to obtain the right ascension of the ascending node Ω using Equations A.13 and A.14 depending on which condition is satisfied (Wakker, 2015). This will ensure that all quadrants are covered as the arc cosine only provides an answer in two quadrants.

$$\Omega = \cos^{-1}(n_x) \text{ for } n_y \geq 0 \tag{A.13}$$

$$\Omega = 2\pi - \cos^{-1}(n_x) \text{ for } n_y < 0 \tag{A.14}$$

The next orbital element calculated will be the argument of periapsis ω using equations A.15 and A.16 depending on the condition satisfied (Wakker, 2015).

$$\omega = \cos^{-1}\left(\frac{\vec{n} \cdot \vec{e}}{e}\right) \text{for } e_z \geq 0 \tag{A.15}$$

$$\omega = 2\pi - \cos^{-1}\left(\frac{\vec{n} \cdot \vec{e}}{e}\right) \text{ for } e_z < 0 \tag{A.16}$$

Before calculating the next orbital element the radial velocity will have to be calculated as seen in Equation A.17 (Wakker, 2015).

$$v_r = \frac{\vec{v} \cdot \vec{r}}{r} \tag{A.17}$$

The orbital element calculated will be true anomaly θ using equations A.18 and A.19 depending on the condition satisfied (Wakker, 2015).

$$\theta = \cos^{-1}\left(\frac{\vec{r} \cdot \vec{e}}{re}\right) \text{for } v_r > 0 \tag{A.18}$$

$$\theta = 2\pi - \cos^{-1}\left(\frac{\vec{r} \cdot \vec{e}}{re}\right) \text{for } v_r > 0 \tag{A.19}$$

Lastly, the eccentric and mean anomaly are obtained from the from the following expressions. Rewriting Equation 5.20 the expression for the eccentric anomaly *E* is obtained as seen in Equation A.20 (Wakker, 2015).

$$E = 2\tan^{-1}\left[\tan\frac{\theta}{2}\sqrt{\frac{1-e}{1+e}}\right] \tag{A.20}$$

Once the eccentric anomaly is calculated Equation A.21 is used to compute the mean anomaly *M*.

$$M = E - e\sin E \tag{A.21}$$

A.2. Kepler Elements to Cartesian Elements

When converting from Kepler Elements to Cartesian elements the eccentric anomaly E is calculated through an iterative process, where the initial E is taken to be equal to M. Using Equation A.22 the iterative process is repeated until the difference between E_i and E_{i+1} is smaller than a desired number, in this case, $1*10^{-10}$. This number was chosen to account for 10 significant figures. However, Chapter 5 also provides other methods to find the convergence limit.

$$E_{i+1} = E + (M - E + e * \sin(E))/(1 - e\cos(E)) \tag{A.22}$$

Once the eccentric anomaly E is obtained the true anomaly θ is calculated as seen in Equation A.23.

$$\theta = 2tan^{-1}\left[\sqrt{\frac{1+e}{1-e}}\tan\left(\frac{E}{2}\right)\right] \tag{A.23}$$

Inside the function, first the semi-latus rectum p is calculated using the aforementioned Equation 5.6 in order to obtain the radius as previously seen in Equation 5.5.
Once the prior steps are carried out, the next course of action is to construct the l_1, l_2, m_1, m_2, n_1 and n_2 matrix elements. This is done using the Euler transformation angles. These transformations are composed of three transformation matrices. The purpose of the transformation is to transform position and valocity vectors from a perifocal basis to an ECI basis.
The first transformation matrix is a transformation about the third axis with the right ascension of the ascending node Ω. The second transformation is a transformation about the first axis with the inclination i and the last transformation is a transformation about the third axis with the argument of periapsis ω. Note that the superscripts and subscripts in the transformation matrices denote the transformation from one basis to the next, ie. T_N^I denotes the transformation from basis $I = (I_x, I_y, I_z)$ to an intermediate basis $N = (n_x, n_y, n_z)$.

The first transformation matrix can be seen below in Equation A.24.

$$T_N^I = \begin{bmatrix} \cos\Omega & -\sin\Omega & 0 \\ \sin\Omega & \cos\Omega & 0 \\ 0 & 0 & 1 \end{bmatrix} \tag{A.24}$$

The second transformation matrix is defined as seen in Equation A.25.

$$T_Q^N = \begin{bmatrix} 1 & 0 & 0 \\ 0 & \cos i & -\sin i \\ 0 & \sin i & \cos i \end{bmatrix} \tag{A.25}$$

The third transformation matrix is presented as observed in Equation A.26.

$$T_P^Q = \begin{bmatrix} \cos\omega & -\sin\omega & 0 \\ \sin\omega & \cos\omega & 0 \\ 0 & 0 & 1 \end{bmatrix} \tag{A.26}$$

Multiplying these three transformation matrices as seen in Equation A.2 transforms the perifocal coordinates to planet-centered inertial coordinates.

$$T_P^I = T_N^I T_Q^N T_P^Q \tag{A.27}$$

This yields a combination of the l_1, l_2, m_1, m_2, n_1 and n_2. The final T_P^I matrix and its constituents can be observed in Equation A.28

$$T_P^I = \begin{bmatrix} \cos\Omega\cos\omega - \sin\Omega\sin\omega\cos i & -\cos\Omega\sin\omega - \sin\Omega\cos\omega\cos i & \sin\Omega\sin i \\ \sin\Omega\cos\omega + \cos\Omega\sin\omega\cos i & -\sin\Omega\sin\omega + \cos\Omega\cos\omega\cos i & -\cos\Omega\sin i \\ \sin\omega\sin i & \cos\omega\sin i & \cos i \end{bmatrix} \tag{A.28}$$

Using Equations A.29 and A.30 the planet-centered inertial coordinates are then calculated.

$$\vec{r} = T_N^I T_Q^N T_P^Q \begin{bmatrix} r\cos\theta \\ r\sin\theta \\ 0 \end{bmatrix} \tag{A.29}$$

$$\vec{v} = T_N^I T_Q^N T_P^Q \sqrt{\frac{\mu}{p}} \begin{bmatrix} -\sin\theta \\ e+\cos\theta \\ 0 \end{bmatrix} \tag{A.30}$$

Bibliography

Aglietti, G. S., Taylor, B., Fellowes, S., Salmon, T., Retat, I., Hall, A., Chabot, T., Pisseloup, A., Cox, C., Mafficini, A., et al. (2020). The active space debris removal mission RemoveDebris part 2: In orbit operations. *Acta Astronautica*, *168*, 310–322.

Airbus. (2021). Removedebris. Retrieved August 10, 2021, from https://www.airbus.com/space/space-infrastructures/removedebris.html.

Alarcón Rodríguez, J. R., Martínez Fadrique, F., & Klinkrad, H. (2002). Collision Risk Assessment with a 'Smart Sieve' Method. In B. Battrick & C. Preyssi (Eds.), *Joint ESA-NASA space-flight safety conference* (p. 159).

Alves Teixeira, G., Bögel, E., Bas Fernández, J., Buurmeijer, H., Meijering, F., Rehling, D., Struzinski, J., van Wolfswinkel, P., Veithen, L., & Zanvliet, N. (2022). Space sweeper final report creating space in space. *TU Delft*.

Andrenucci, M., Pergola, P., & Ruggiero, A. (2011). *Expanding foam application for active debris removal* (Doctoral dissertation). University of Pisa.

Anz-Meador, P. D., Opiela, J. N., Shoots, D., & Liou, J.-C. (2018). *History of on-orbit satellite fragmentations*. NASA.

Biesbroek, R., Aziz, S., Wolahan, A., Cipolla, S.-f., Richard-Noca, M., & Piguet, L. (2021). The Clearspace-1 mission: ESA and Clearspace team up to remove debris. *Proc. 8th Eur. Conf. Sp. Debris*, 1–3.

Bonilla, D. (2015). Gravity tractor. Retrieved September 3, 2021, from https://www.nasa.gov/content/asteroid-grand-challenge/mitigate/gravity-tractor.

Britannica. (2021). Vacuum. Retrieved November 16, 2021, from https://www.britannica.com/science/vacuum-physics.

Caldwell, S. (2021). 13.0 deorbit systems. Retrieved February 10, 2022, from https://www.nasa.gov/smallsat-institute/sst-soa/deorbit-systems.

Carceller, P. (2021). *Literature report: Mitigation of small space debris*. Technische Universiteit Delft.

Dunbar, B. (2008). Catching comet dust with aerogel. Retrieved August 10, 2021, from https://www.nasa.gov/mission_pages/stardust/mission/index-aerogel-rd.html.

El-Rashid, F., Gossner, T., Kappeler, T., & Ruiz-Peris, M. (2021). A life-centred design approach to innovation: Space vulture, a conceptual circular system to create value from space debris.

ESA. (2021a). About space debris. Retrieved June 22, 2021, from http://www.esa.int/Safety_Security/Space_Debris/About_space_debris.

ESA. (2021b). Active debris removal. Retrieved December 12, 2021, from https://www.esa.int/Safety_Security/Space_Debris/Active_debris_removal.

ESA. (2021c). ESA commissions world's first space debris removal. Retrieved June 2, 2021, from https://www.esa.int/Safety_Security/Clean_Space/ESA_commissions_world_s_first_space_debris_removal.

ESA. (2021d). Space debris by the numbers. Retrieved June 10, 2021, from https://www.esa.int/Safety_Security/Space_Debris/Space_debris_by_the_numbers

ESA. (2021e). Space environment statistics. Retrieved June 9, 2021, from https://sdup.esoc.esa.int/discosweb/statistics/

ESA. (2022). Space debris: Analysis and prediction. Retrieved June 10, 2021, from https://www.esa.int/Space_Safety/Space_Debris/Analysis_and_prediction.

ESA/UNOOSA. (2020). The history of space debris creation. Retrieved February 1, 2022, from https://www.esa.int/ESA_Multimedia/Images/2021/03/The_history_of_space_debris_creation

Girardin, V., Arnold, D., Bertone, S., & Jäggi, A. (2018). Non-gravitational forces acting on spacecraft: Impact of different atmospheric models on leo orbits.

Hall, N. (2021). The drag equation. Retrieved October 13, 2021, from https://www.grc.nasa.gov/www/k-12/airplane/drageq.html.

Hoots, F. R., Crawford, L. L., & Roehrich, R. L. (1984). An analytic method to determine future close approaches between satellites. *Celestial mechanics*, *33*(2), 143–158.

Johnson, N. L., Krisko, P. H., Liou, J.-C., & Anz-Meador, P. D. (2001). Nasa's new breakup model of evolve 4.0. *Advances in Space Research*, *28*(9), 1377–1384.

Jones, S. M., & Sakamoto, J. (2011). Applications of aerogels in space exploration. *Aerogels Handbook*, 721–746. https://doi.org/10.1007/978-1-4419-7589-8_32

Kan, S. (2007). China's anti-satellite weapon test.

Kelso, T. S. (2009). Analysis of the Iridium 33-Cosmos 2251 collision. Retrieved September 16, 2021, from https://celestrak.com/publications/AMOS/2009/AMOS-2009.pdf

Kelso, T., & Gorski, A. (2022). Space surveillance: Lessons learned from the iridium-cosmos collision.

Kessler, D. J., Johnson, N. L., Liou, J., & Matney, M. (2010). The kessler syndrome: Implications to future space operations. *Advances in the Astronautical Sciences*, *137*(8), 2010.

Lemmens, S., & Letizia, F. (2022). *ESA's annual space environment report*. Technical Report GEN-DB-LOG-00288-OPS-SD, ESA Space Debris Office.

Mains, D. L., & Sorge, M. E. (2022). The impact satellite fragmentation model. *Acta Astronautica*, *195*, 547–555. https://doi.org/https://doi.org/10.1016/j.actaastro.2022.03.030

May, C. R. (2021). Triggers and effects of an active debris removal market.

McKnight, D. (2021). Leolabs. *Proc. 8th Eur. Conf. Sp. Debris*.

Montenbruck, O., & Gill, E. (2012). *Satellite orbits: Models, methods and applications*. Springer Science & Business Media.

NASA. (2021). Ares. Retrieved June 7, 2021, from https://orbitaldebris.jsc.nasa.gov/measurements/debrisat.html

Pham, L. N., Tabor, G. F., Pourkand, A., Aman, J. L., Hermans, T., & Abbott, J. J. (2021). Dexterous magnetic manipulation of conductive non-magnetic objects. *Nature*, *598*(7881), 439–443.

Pieters, L. C., & Noomen, R. (2020). Space-based laser ablation for space debris removal. *Proc. 8th Eur. Conf. Sp. Debris*.

Rao, A. (2021). *Orbital mechanics: An introduction*. University of FLorida. Retrieved December 16, 2021, from https://www.anilvrao.com/resources/EAS4510-Course-Notes.pdf.

Reinthal, E. (2017). Relative orbit propagation and control for satellite formation flying using continuous low-thrust.

Scharring, S., Kästel, J., Wagner, G., Riede, W., Klein, E. M., Bamann, C., Döberl, E., Weinzinger, D., Promper, W., Flohrer, T., et al. (2021). Potential of using ground-based high-power lasers to decelerate the evolution of space debris in leo. *8th European Conference on Space Debris*.

Shan, M., Guo, J., & Gill, E. (2016). Review and comparison of active space debris capturing and removal methods. *Progress in Aerospace Sciences*, *80*, 18–32.

Spot the station: International space station. (2022). Retrieved October 12, 2022, from https://spotthestation.nasa.gov/

Steffensen, J. F. (2006). *Interpolation*. Courier Corporation.

Takahashi, K., Charles, C., Boswell, R. W., & Ando, A. (2018). Demonstrating a new technology for space debris removal using a bi-directional plasma thruster. *Scientific reports*, *8*(1), 1–10.

Trivailo, P. M., & Kojima, H. (2016). Dynamics of the net systems, capturing space debris. *Transactions of the Japan Society for Aeronautical and Space Sciences, Aerospace Technology Japan*, *14*(ists30), 57–66.

UNOOSA. (2010). Space debris mitigation guidelines of the committee on the peaceful uses of outer space. Retrieved July 22, 2022, from https://www.unoosa.org/pdf/publications/st_space_49E.pdf.

UPM. (2021). The ion beam shepherd concept. Retrieved August 20, 2021, from https://leosweep.upm.es/en/ibs/ibs-concept-applications/31-the-ion-beam-shepherd-concept

Wakker, K. F. (2015). *Fundamentals of astrodynamics*. Faculty of Aerospace Engineering Delft University of Technology.

Werner, D. (2018). ESA to study links between space debris removal and satellite servicing. Retrieved July 5, 2021, from https://www.space.com/40080-esa-space-debris-removal-satellite-servicing-study.html.

Wertz, J. R. (2009). Earth satellite parameters. *Orbit and constellation design and management: Spacecraft orbit and attitude systems* (p. 976). Springer.

Woignier, T., Duffours, L., Colombel, P., & Durin, C. (2013). Aerogels materials as space debris collectors. *Advances in Materials Science and Engineering*, *2013*, 1–6.

Wong, T. (2015). *Feasibility study of a gnss tracking application on android* (Master's thesis). Tampere University.

Wormnes, K., Le Letty, R., Summerer, L., Schonenborg, R., Dubois-Matra, O., Luraschi, E., Cropp, A., Krag, H., & Delaval, J. (2013). ESA technologies for space debris remediation. *6th European Conference on Space Debris*, *1*, 1–8.